

https://dspace.org/

Wear Reduction and Media Density Optimization for the Single Stage Pipe Densifier at Sishen Iron Ore's Beneficiation Plants

Botha, Simone

0202-02
University of the Witwatersrand, Johannesburg
https://hdl.handle.net/10539/38879
Both, Simone. (2024). Wear Reduction and Media Density Optimization for the Single Stage Pipe Densifier at Sishen Iron Ore's Beneficiation Plants. [Master's dissertation, University of the Witwatersrand, Johannesburg]. WIReDSpace. https://hdl.handle.net/10539/38879

Downloaded from a DSpace repository. https://dspace.org/



WEAR REDUCTION AND MEDIA DENSITY OPTIMIZATION FOR THE SINGLE-STAGE PIPE DENSIFIER AT SISHEN IRON ORE'S BENEFICIATION PLANTS

MSc (50/50) RESEARCH REPORT

Prepared by

Simone Botha

2413299

Submitted to

Master of Science in Engineering by advanced coursework and research: A research report submitted to the Faculty of Engineering and the Built Environment, University of the Witwatersrand, Johannesburg, in partial fulfilment of the requirements for the degree of Master of Science in Engineering.

Supervisor: Kitungwa Kabezya

August 2023

CANDIDATE'S DECLARATION

I declare that this research report is my own unaided work. It is being submitted to the degree of Master of Science to the University of Witwatersrand, Johannesburg. It has not been submitted before for any degree or examination to any other University.



……

(Signature of Candidate)

11th day of August 2023

ABSTRACT

The depleting high-grade iron ore mining supply at Sishen Mine in the Northern Cape, South Africa, has given rise to its beneficiation plants operating at higher media densities to upgrade lower-grade ore.

In this study, densification was numerically modelled using an MPPIC model and experimentally tested using a 200-mm diameter centrifugal densifier from two local suppliers – Multotec and HMA. Shear stress, wear rate, separation efficiency and media losses were measured at increasing operating densities and differing vortex finder sizes.

Optimum operating conditions were established. It was found that a feed density of 3.60 t/m^3 and a shear stress of 9.70 e^{-3} N/m^3 at the inlet using a vortex finder diameter size of 30 mm exhibited favourable performance in terms of media densification and downstream recovery.

The practical significance of this is proven in terms of wear rate and its predictability to provide a consistent overflow of below 1.20 t/m^3 media to the recovery circuit. Furthermore, information about ideal operating conditions in terms of inlet pressure and controls to identify premature failures were established.

DEDICATION

This research paper is dedicated to the fiancé and parents of the researcher who gave their utmost support and never-ending encouragement throughout this study. It is also dedicated to the employer of the researcher who has made this research possible by technical guidance, financial aid, and employment to complete this study.

ACKNOWLEDGEMENTS

The researcher would like to acknowledge and give her warmest thanks to her supervisor, Kitungwa Kabezya, who made this work possible. His guidance, correction and advice carried her though all the stages of this project.

All the glory to be given to the Lord God Almighty who gives us the strength, knowledge, and wisdom to continue and keep positive. To Him be the kingdom, the power, and the glory.

TABLE OF CONTENTS

1. INTRODUCTION 1
1.1. Background 1
1.2. Problem statement 5
1.2.1. The need for wear prediction of densification 7
1.3. Research objectives 9
2. LITERATURE REVIEW 11
2.1. The significance of the rising density principle 11
2.2. Comparison of the densification applications 12
2.3. Computational fundamentals and modelling 17
2.3.1. Multiphase flow 17
2.3.2. Coupling 19
2.3.3. Particle wear 20
2.3.4. Computational frame of reference 21
2.3.5. Motion of particles 23
2.3.6. Inter-phase forces 28
2.3.7. Kinetic theory of granular flow 29
2.3.8. Wear mechanism principle and models 33
3. METHODOLOGY 41
3.1. Phase I: experimental testing 41
3.1.1. Experimental setup 41
3.1.2. Operating flow and pressure onset conditions 43
3.1.3. Early failure detection 44
3.2. Phase II: numerical model 45
3.2.1. CFD-MPPIC integration 46
3.3. Domain setup 50
3.4. Boundary and operating conditions 52
3.4.1. Inlet boundary 52
3.4.2. Underflow and overflow boundary 52
3.4.3. Operating conditions 52
3.5. CFD-MPPIC solver 52
3.6. Solver settings 54

3.6.1. Fluid solver 54
3.6.2. Particle solver 55
3.7. Convergence criteria 57
3.8. Design of experiments 57
4. RESULTS AND DISCUSSION 58
4.1. Phase I: experimental test work 58
4.1.1. Densifier inlet wear rate 58
4.1.2. Densifier separation efficiency 59
4.1.3. Experimental summary 64
4.2. Phase II: numerical model results 66
4.2.1. Run 1: 30-mm vortex finder and 3.4 t/m^3 feed SG 66
4.2.2. Run 5: 35-mm vortex finder and 3.5 t/m^3 feed SG 68
4.2.3. Run 9: 40-mm vortex finder and 3.6 t/m^3 feed SG 70
4.2.4. Numerical model summary 72
4.3. Discussion and comparison 73
5. CONCLUSION 75
5.1. Recommendations 76
6. REFERENCES 78
APPENDIX A: DENSIFIER PUMP CURVE 84
APPENDIX B: NUMERICAL MODEL ITERATION 85
APPENDIX C: SAFETY CONSIDERATIONS 91
APPENDIX D: INDUSTRIAL CONSIDERATIONS 94
APPENDIX E: INSPECTION AND MAINTENANCE SCHEDULE 97

LIST OF FIGURES

Figure 1.1: Sishen DMS lump performance at a ROM quality of 59.43% Fe 2
Figure 1.2: Medium circuit of the Sishen drum plant 3
Figure 1.3: Typical single line densifier failures observed at the drum plant 6
Figure 2.1: Examples of pipe and cyclonic densifier arrangements (Napier-Munn, et al., 1995) 12
Figure 2.2: The effect of the spigot wear on cut density and efficiency (Bekker, 2014) 14
Figure 2.3: Medium losses associated with a densifier at a set point of 3.0 t/m^3 (Bosman, 2006) 16
Figure 2.4: Demonstration of inter-phase interactions through coupling (Crowe, 2005) 20
Figure 2.5: Force balance of a non-uniform particle interacting with a surface (Arabnejad, et al., 2015) 37
Figure 3.1: Experimental setup for the HMA and Multotec densifiers 42
Figure 3.2: Early failure detection applications (Napier-Munn, et al., 1995) 45
Figure 3.3: Provided densifier model with internal volume in blue 47
Figure 3.4: Full internal domain for computational analysis 47
Figure 3.5: Mesh cross-section 48
Figure 3.6: Mesh refinement in the overflow region 49
Figure 3.7: Boundary layer mesh near the surfaces 49
Figure 3.8: Normalized percentage mass frequency and (B) percentage size frequency 56
Figure 4.1: Velocity-wear profile of the densifier inlet 58
Figure 4.2: Multotec densifier O/F vs SG at different vortex finder diameters 61
Figure 4.3: Multotec and HMA densifier overflow density vs operating density 62
Figure 4.4: Magnetic separator feed density vs operating density 63
Figure 4.5: Percentage MagSep magnetic losses with and without control water 64
Figure 4.6: Model flow and density outputs of Run 1 in the DoE 66
Figure 4.7: Shear stress outputs of Run 1 in the DoE 67
Figure 4.8: Model flow and density outputs of Run 5 in the DoE 68
Figure 4.9: Shear stress outputs of Run 5 in the DoE 69
Figure 4.10: Model flow and density outputs of Run 9 in the DoE table 70
Figure 4.11: Shear stress on the densifier 70
Figure 4.12: Practical observations of shear stress impact and end of part life 73

LIST OF TABLES

Table 2.1: Cyclonic and tube densifier test work results (Popplewell & Burks, 1988)..... 13
Table 2.2: Summary of two-phase flow systems and their significance in industrial processes (Sommerfeld, 2017) 18
Table 2.3: Summary of different coupling levels in multiphase flows (Crowe, 2005; Sommerfeld, 2017; Elghobashi, 1994; Loth, 2000)..... 18
Table 3.1: Comparison between current and test densifiers 41
Table 3.2: Experimental DoE for the tube densifier by test work 43
Table 3.3: CFD fine mesh inputs 46
Table 3.4: Samples taken to verify the percentages of solid and magnetic material in the feed .. 56
Table 3.5: Experimental DoE for the tube densifier by modelling..... 57
Table 4.1: Experimental wear rate results of the Multotec PC200 inlet..... 59
Table 4.2: Experimental wear rate results of the HMA 200NB inlet 59
Table 4.3: Summary of the average overflow densities for the Multotec and HMA test units 60
Table 4.4: Experimental DoE for the tube densifier by test work 65
Table 4.5: Model outputs of Run 1 to Run 3 in the DoE..... 68
Table 4.6: Model outputs of Run 4 to Run 6 in the DoE table 70
Table 4.7: Model outputs of Run 7 to Run 9 in the DoE table 72
Table 4.8: DoE for the tube densifier by modelling 72

LIST OF ABBREVIATIONS

Abbreviation	Meaning in Context
CFD	Computational fluid dynamics
CFD-DEM	Computational fluid dynamics–discrete element method
CGHS	Coarse-grained hard sphere
CGPM	Coarse-grained particle method
DEM	Discrete element method
DEM	Discrete element modelling
DMS	Dense media separation
DoE	Design of experiments
Fe	Chemical symbol for iron
FeSi	Ferrosilicon
HG	High-grade
HMA	Supplier of pipe densifiers
KTGF	Kinetic theory of granular flow
LG	Low-grade
MagSep	Magnetic separator supplied by Malvern

MPPIC	Multiphase particle-in-cell
MTTF	Mean-time-to-failure
Multotec	Supplier of pipe densifiers
O/F	Densifier overflow (dilute media)
ROM	Run-of-mine
TDHS	time-driven hard sphere
tph	Tonnes per hour
U/F	Densifier underflow (concentrated media)
WEMCO	Supplier of beneficiation drums

LIST OF SYMBOLS

Abbreviation	Meaning
g	Gram
h	Hour
kPa	Kilopascal
m	Metre
N	Newton
t	Tonne (1 000 kg)
t/m^3	Tonnes per cubic metre

1. INTRODUCTION

1.1. Background

Sishen Mine's iron ore dense media separation (DMS) processing line comprises four beneficiation plants based on the size fraction of iron ore treated, namely the fine cyclone plant (–5 +3.35 mm), coarse cyclone plant (–8 +5 mm), medium drum plant (–25 +8 mm) and coarse drum plant (–90 +25 mm). WEMCO drum technology has been used since the 1950s at Sishen (Legault-Seguin, Mohns, & Rylatt, 2016). This is due to the limitation of cyclones to treat –200 + 8 mm ore (Napier-Munn T. , 2018). All four plants use a dense media to aid in the beneficiation of the run-of-mine (ROM) to meet client product specification in terms of iron ore grade and size.

These iron ore beneficiation plants were designed to treat high-grade ROM known as "A-grade" material. A-grade ROM has an iron content of approximately 60% Fe and needs to be upgraded to a high-grade (HG) premium iron ore of 64% Fe for the fine and 65% Fe for the lump product with constraints on the contaminant levels (Tom, 2015). The product iron ore quality specification is dependent on the size of the product and the market demand.

Sishen DMS plants make use of a dense media called ferrosilicon (FeSi) to upgrade the iron content of the ore. A blend of ferrosilicon and water is used to achieve a specific operating density to control the cut-point in the dense media cyclone or WEMCO drum unit and obtain the desired iron ore product quality. The relationships between cut-point density, product quality and yield for a lump sample are illustrated in Figure 1.1.

This study revealed that the beneficiation plants were operated at a medium density of 3.6 t/m^3 with an expected yield of 88.8% to meet HG product quality specification of 65.2% Fe. It is

evident from the relationships that the cut-point density is proportional to the product quality but indirectly proportional to the yield. Traditionally, operating densities of between 3.4 t/m^3 and 3.6 t/m^3 are maintained, which is highly dependent on the ROM quality to the plant (Tom, 2015).

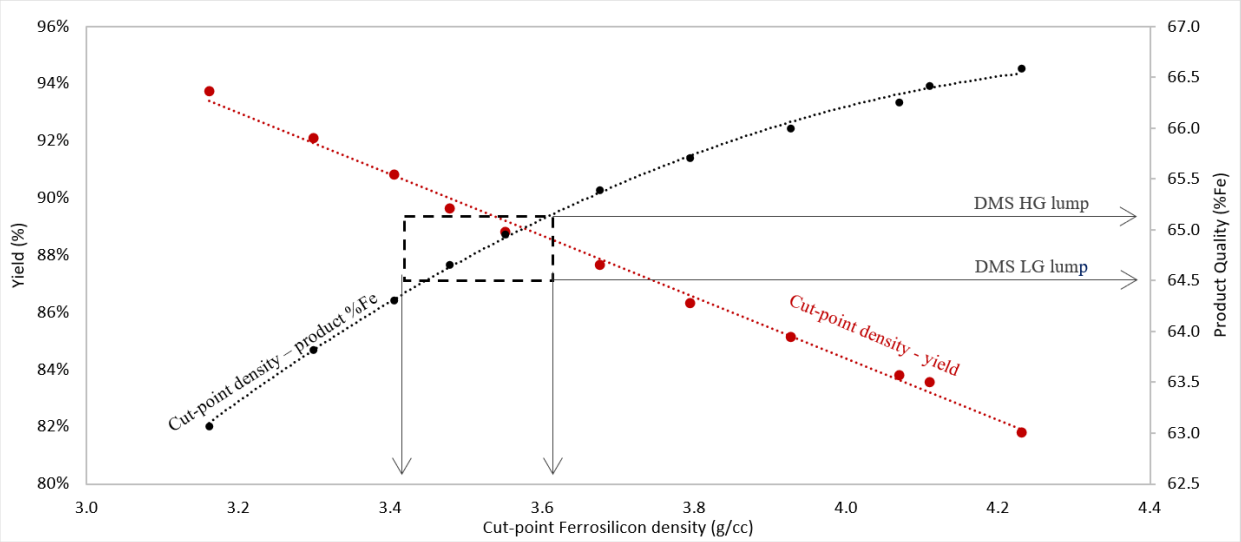


Figure 1.1: Sishen DMS lump performance at a ROM quality of 59.43% Fe

The control of the specific operating density requires the ferrosilicon carrying media to undergo a densification stage to recover media back into the circuit. The equipment responsible for densification is called a single-stage centrifugal densifier, also known as a pipe densifier, which will be the focus of this paper.

The densifier sump feeds the single-stage pipe densifier as illustrated in Figure 1.2. The aim of the pressurized densifier is to classify the media by inducing a density differential. High-density media must be separated from low-density media. High-density media, known as the underflow, reports back into the correct media sump to ensure that the operating density is maintained, while low-density media, referred to as the overflow, reports to the dilute sump. All low-density media

recovered to the dilute sump is to subject ferrosilicon recovery by primary and secondary magnetic separation.

Recently, Sishen DMS has been exposed to lower-grade material with a lowered iron feed content of between 57%– 60% Fe with higher percentage of silica in the feed. Depending on the iron-contaminant relationship, the cut-point and operating density need to increase proportionately to ensure the contaminants report to the waste and the product quality meets premium product specification.

A higher operating density leads to a higher densifier feed density since a higher density media will be drained at the waste screen. This places strain on the single-stage densifier to differentiate between a larger range of target underflow and overflow densities. The higher operating density also has an increasing effect on medium losses at the drain and rinse screens and downstream magnetic separation (Napier-Munn, et al., 1995). Therefore, it is of utmost importance that the densifier performs efficiently and maintains adequate density control.

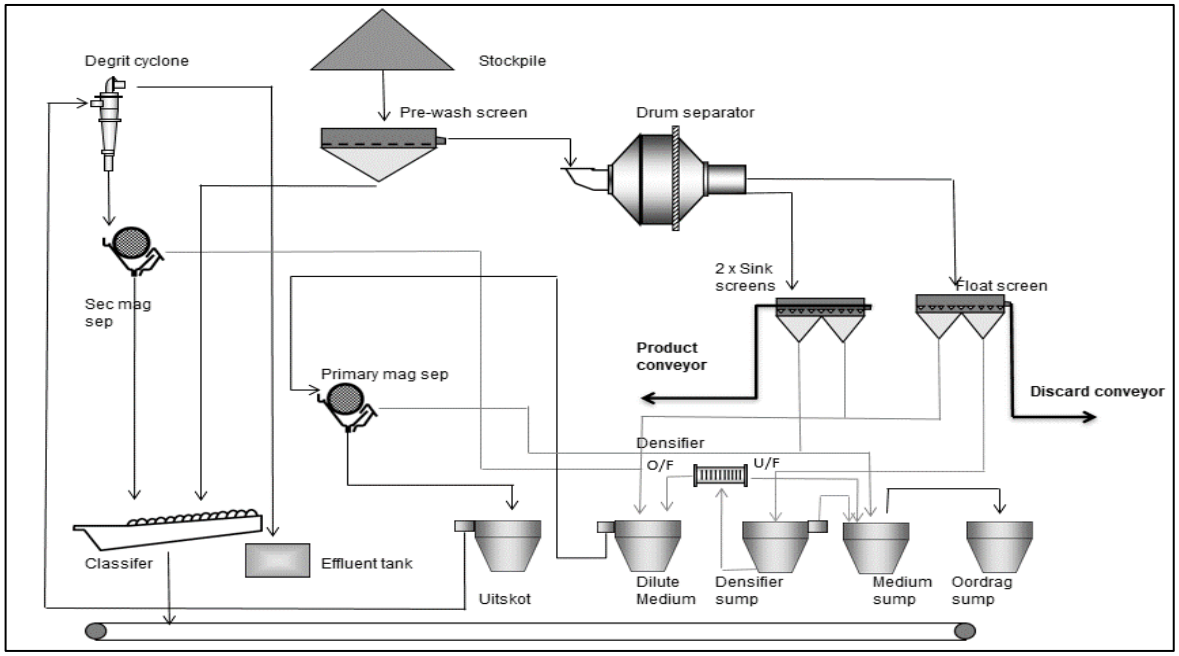


Figure 1.2: Medium circuit of the Sishen drum plant

The type of FeSi used also has an impact on the densification of the densifier unit under higher operating density conditions. Sishen uses nitrogen gas atomized Exxaro coarse silicon as medium in the drum plant since it is most suited to use for heavy medium densities above 3.6 t/m^3 (Myburgh, 2013). The advantage of gas atomization is sharper separation, which justifies its popular use for coarse iron ore beneficiation. However, it comes at a higher cost, so recovery needs to be efficient to lower its economic impact (Collins, Napier-Munn, & Sciarone, 1974). Apart from the cost implications, medium recovery circuits must be efficient to ensure that the required rheological composition is maintained in the circuit (Ferrara, Lapasin, & Bevilacqua, Modelling the rheological behaviour of dense media and design of medium circuits in dynamic DMS processes, 1992).

An inefficient pipe densifier unit causes misplacement of high-density media to the overflow and low-density media to the underflow. This negatively affects the density control of the media circuit and, in turn, causes instability in the iron ore product quality. Moreover, misplacement significantly strains the media recovery reporting to the dilute circuit (Waanders & Mans, 2003).

One of the main reasons the pipe densifiers malfunction is the excessive wear caused by the abrasive nature of the high-density ferrosilicon media. A worn densifier causes extended periods of inefficient operation (misplacement) until the unit is eventually opened and parts are replaced, or it fails by dismantling itself under high pressure. The latter situation poses an extreme safety risk for operators.

In summary, the Sishen DMS beneficiation plant needs to be geared to treat lower-grade ore by beneficiating iron ore at higher cut-points to consistently meet product specification. In effect, this requires an efficient single-stage media densification process to maintain stable density

control of the circulating media and reduce magnetic content in the dilute circuit to minimize ferrosilicon losses.

1.2. Problem statement

As the mining of high-grade iron ore gets depleted, a need arises to beneficiate the low-grade material, which in turn requires the dense media plants to operate at higher operating densities of 3.6 t/m3. Previously, at Sishen mine, the centrifugal pipe densifiers were able to densify up to 4.0 t/m3 (Voges, 1982). The efficient density control of the drum plant is important as it is responsible for producing high-grade lump iron ore.

Densifier failures due to excessive wear are one of greatest issues faced at the Sishen drum plant. The most dangerous and costly occurrence is when the inlet ring of the densifier dismantles under high pressure. This is due to excessive wear at the inlet. The release of high-pressure energy can gravely injure a person if they are in the line of fire. It also leads to unnecessary FeSi losses, with each occurrence requiring at least two to six bags of FeSi to be added to replenish the circuit media after media has been washed back into the system from the floor sump. These severe occurrences occurred eight times in 2021 and three times at drum plants until June 2022.

Other failures due to inlet or vortex finder wear are also cost-intensive as these parts need to be replaced often and lead to higher FeSi losses. This is because there is no instrumentation to monitor the feed pressure to the densifier. Sishen is highly dependent on operator intervention, and the failure is usually only identified if most of the FeSi has been misplaced and washed out at the primary magnetic separator. The reason is that misplacement at the densifier overloads the magnetic separator with magnetic material to a point where the medium is washed out and the module is no longer able to achieve the required density. This may take hours or even days

before it is picked up and will cause instability under densification of the media and, ultimately, lower product quality. Typical failures are illustrated in Figure 1.3. According to Dardis (1987), inefficient magnetic recovery can account for 18%–39% of the total operating cost of the DMS.

The current wear rate is estimated to be four weeks to eight weeks per inlet and vortex finder. Currently, no engineering controls are in place, but operators and metallurgists perform regular inspections. Replacements are done on routine maintenance and plant-wide densifier audits are done on shutdowns to mitigate the effects of failure.



Figure 1.3: Typical single line densifier failures observed at the drum plant

With the current performance of the densifiers, an optimization project has been undertaken to investigate the optimization of densifier wear and to ensure a tighter density control of the media when operating at higher operating densities of 3.4–3.6 t/m^3. The low mean-time-to-failure (MTTF) of the single-line densifiers implies unplanned and costly failures, unsafe operation and increased FeSi consumption. This is due to incorrect operating pressure, no pre-indication of densifier failure and incorrect design of densifier assembly.

In light of this problem, there is a need to improve the densifier's physical parameters and operating conditions to ensure safe, cost-efficient concentration and stable operation. This will be investigated with both computer modelling and field experimental testing.

1.2.1. The need for wear prediction of densification

Despite extensive research on DMS cyclones in the past, operational issues with both DMS cyclones and DMS densifiers persist (Scott & Napier-Munn, 1992; Wood, et al., 1989; Restarick & Krnic, 1991; Galvin & Smitham, 1994; He & Laskowski, 1994; Ferrara, et al., 2000; Magwai & Bosman, 2008). Problems like the "surging" phenomenon (Wood, Davis, & Lyman, 1989), vortex finder overloading, severe wearing of cyclone walls (Zughbi, Phil, & Hutton, 1991) and difficulties in scale-up and system instability remain prevalent.

Excessive wearing of dense media concentrators walls is a significant issue, though it is not well understood. For instance, in the case of a DMS cyclone used to collect diamond-bearing lamproite ore, the rate of vortex finder wear determines the cyclone's operation life, where a significant portion of the feed reports to the floats through the vortex finder (Zughbi, Phil, & Hutton, 1991). Wearing can alter the densifier's geometry and later affect its separation performance. This means that predicting the wear rate of densifier walls is crucial. Additionally, finding the most severely worn areas in a densifier is essential for possible targeted treatments.

The wear occurring in densifiers results from particle abrasion on solid surfaces, a common phenomenon in various industrial processes and machinery, such as sandblasting, pneumatic pipelines, helicopter propellers, and turbine blades. The extent of surface erosion caused by abrasive particle impingement depends on factors such as particle impact velocity, impact angle, properties of the particles, and target material properties (Jianren, Dadong, Keli, & Kefa, 1992)

These concepts form the basis for most wear models, including the widely used Finnie wear model (Finnie, 1960; Chen, et al., 1998; Lester, et al., 2010). Most erosion models have been developed based on the Finnie model or its modifications.

The literature on modelling wear in dense media cyclones is quite limited and none exists in the application of media densification. The closest work is by Zughbi et al. (1991) where a two-dimensional computational fluid dynamics (CFD) model was used to predict the wear rate in a DMS cyclone used in diamond mines.

Modelling wear in dense media concentrators depends on the dynamic process of particle-wall interaction, which can be obtained using the discrete element method (DEM). Discrete element modelling models the motion of particles as a discrete phase, described by Newton's laws of motion (Cundall & Strack, 1979). While DEM has been applied to predict wear in pure particle flow systems like mills (Cleary, 1998; Jayasundara, et al., 2011), its usage for particle-fluid systems (CFD-DEM) focuses on modelling the flow rather than wear prediction. However, recent developments have seen the use of CFD-DEM to study the multiphase flow in dense media concentrators (Chu, et al., 2009; Chu, et al., 2012). This work employs a CFD-DEM approach coupled with the Finnie wear model (Finnie, 1960) to predict the wear rate of cyclone walls under various conditions and to investigate the effect of a worn spigot wall.

For this study, the aim was to introduce new research using the multiphase particle-in-cell (MPPIC) method and to compare this model to experimental data to simulate the efficiency and wear on the problematic densifiers at Sishen mine.

1.3. Research objectives

The purpose of this study was to find a practical, wear improvement solution for the Sishen dense media separation (DMS) plant when operated at higher operating densities. This involved defining and optimizing performance by the following objectives:

i. To investigate the impact of operating density on densifier performance and wear by practical test work and numerical modelling. The considered operating densities were:
   - 3.4 t/m^3
   - 3.5 t/m^3
   - 3.6 t/m^3

ii. To investigate the impact of feed pressure on densifier performance and wear by changing the diameter of the vortex finder. This was done by MPPIC modelling and practical test work. The considered vortex finder diameters were:
   - 40 mm
   - 40 mm
   - 35 mm

These objectives were investigated under the following efficiency (A) and safety (B) considerations:

A. Under normal operation, the densifier overflow density must not exceed 1.7 t/m^3 and the primary magnetic separator feed density should not exceed 1.2 t/m^3 to ensure that the dilute circuit is not overloaded with magnetic material.
B. The design changes to the densification circuit need to enable operations to detect and act on premature densifier failures.

A constant in this study was that no lining wear property improvement work was done, as original type of lining material was used in the investigations for both manufacturers. The study was able to identify a set of operating parameters that would result in lower lining wear against the original design.

Furthermore, the research needed to measure the densifier MTTF. If failures can be predicted, proactive maintenance can be planned into routine maintenance schedules to further benefit the run hours of the plant and reduce the number of unexpected stops and FeSi losses below 80 g/t (Voges, 1982).

2. LITERATURE REVIEW

The subsequent section aims to provide a concise review of the most significant work done thus far on densification practices, theories and models.

2.1. The significance of the rising density principle

Dense media separation is defined by Gochin & Smith (1983) as a technique used to sort particles based on their clear specific gravity relative to the operating medium density. Simply stated, in any dense media separation process, the low-density particles will segregate to the float or overflow and the high-density particles will sink or report to the underflow (Pryor, 1965).

This principle can be applied when ore is beneficiated using an operating medium or in the case of operating medium densification. The rising density control principle is used to effectively control the operating medium at the setpoint level (Osborne, 1988). This means that the medium density in the correct medium sump must always be higher than the setpoint. To get the medium density to setpoint, dilution control water is added to the correct medium sump.

Maintaining the density setpoint is of utmost importance in achieving consistent ore product quality as it provides a consistent cut-point in the cyclone or drum beneficiation unit. Therefore, density control is a vital parameter, such as cyclone pressure and media stability, in any DMS.

There are two methods for achieving density control, namely pipe and cyclonic densification (Voges, 1982). Both of these are centrifugal methods. The employed method should have the ability to control to 0.05 t/m^3 of the setpoint to effectively comply with the rising density principle and ensure that the density in the correct medium sump is always higher than the setpoint (Osborne, 1988).

2.2. Comparison of the densification applications

The most common designs used for medium densification are pipe and cyclonic densifiers as shown in Figure 2.1. Feed is introduced tangentially into the densifier to create a centrifugal movement of the fluid. The cyclone has a cylindrical body and the spigot discharges tangentially from the cylindrical barrel. High-density material centrifuges to the inside walls of the densifier and discharges at the spigot/outlet (Osborne, 1988). The vortex finder arrangement is where the overflow or low-density medium is discharged. In a typical DMS configuration, this low-density media will report to the dilute medium sump.

In literature, test work results have been recorded on the performance of both cyclonic and tube densifiers (Popplewell & Burks, 1988). The results are shown in Table 5.1. The cyclonic densifier design is based upon a typical classification cyclone. The advantage is that it can achieve high underflow densities (> 3.5 t/m^3). However, its volumetric recovery to underflow is relatively low. Therefore, the cyclone overflow contains a large quantity of media.

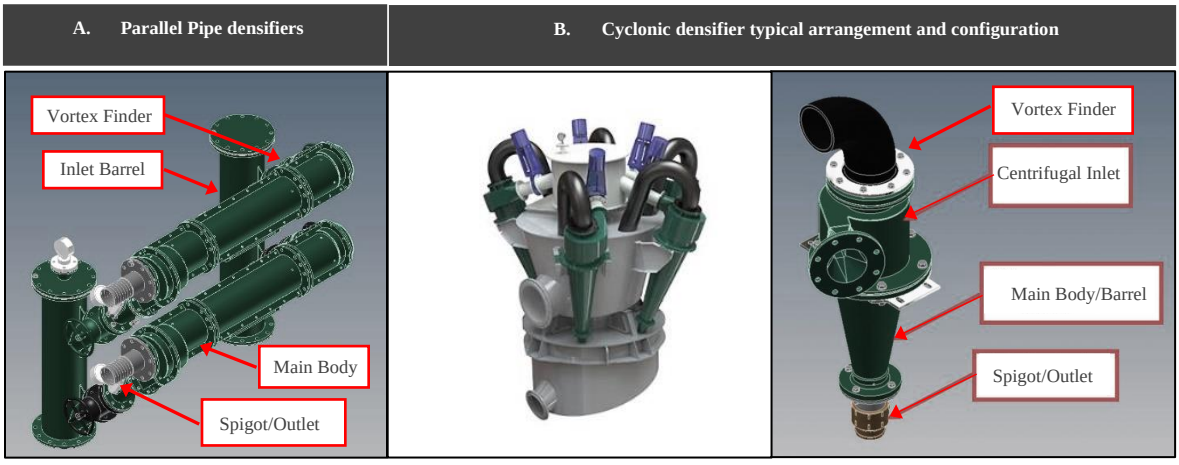


Figure 2.1: Examples of pipe and cyclonic densifier arrangements (Napier-Munn, et al., 1995)

The pipe densifier, also referred to as a tube densifier, has a tangential inlet and outlet to support the centrifugal motion of the fluid. It is equipped with a relatively small vortex finder for tighter control of the overflow density. As a result, it has a high volumetric recovery to underflow (80% to 90%) and a low-density overflow (< 1.3 t/m^3) which is beneficial for downstream medium recovery.

Table 2.1 shows the type of configurations for densifiers, of which a single-stage horizontal densifier is considered in this study. This overflow density should be below a value of 1.7 t/m^3 (Weldhagen, 2015). The configuration with the largest density differential between the underflow and overflow and highest feed density is the best performer.

It is evident from the results that the 100-mm tube densifier with a feed flow of 27.30 m^3/h and a feed density of 2.84 t/m^3 will be a suitable indication (Popplewell & Burks, 1988). To specify the recommended spigot (outlet) size for both the cyclonic and pipe densifiers, the following rule of thumb is used as a reference: Spigot (outlet) diameter ≤ 85% vortex finder diameter (Bekker, 2014).

Table 2.1: Cyclonic and tube densifier test work results (Popplewell & Burks, 1988)

Densifier Configuration	**Feed**		**Overflow**		**Underflow**	
	Flow (m^3/h)	**Density (t/m^3)**	**Flow (m^3/h)**	**Density (t/m^3)**	**Flow (m^3/h)**	**Density (t/m^3)**
Cyclone 250 mm	74.20	2.57	53.55	2.30	20.65	3.27
Cyclone 200 mm	36.20	2.87	20.41	2.22	15.79	3.71
Cyclone 200 mm	48.30	2.70	35.32	2.52	12.98	3.19
Tube 100 mm	27.30	2.84	9.03	1.08	18.27	3.71

Cyclone 100 mm	13.80	2.51	6.38	1.23	7.42	3.61
Tube 100 mm	35.00	2.70	5.48	1.03	29.52	3.01
Cyclone 200 mm	43.00	2.70	27.52	2.25	15.48	3.50

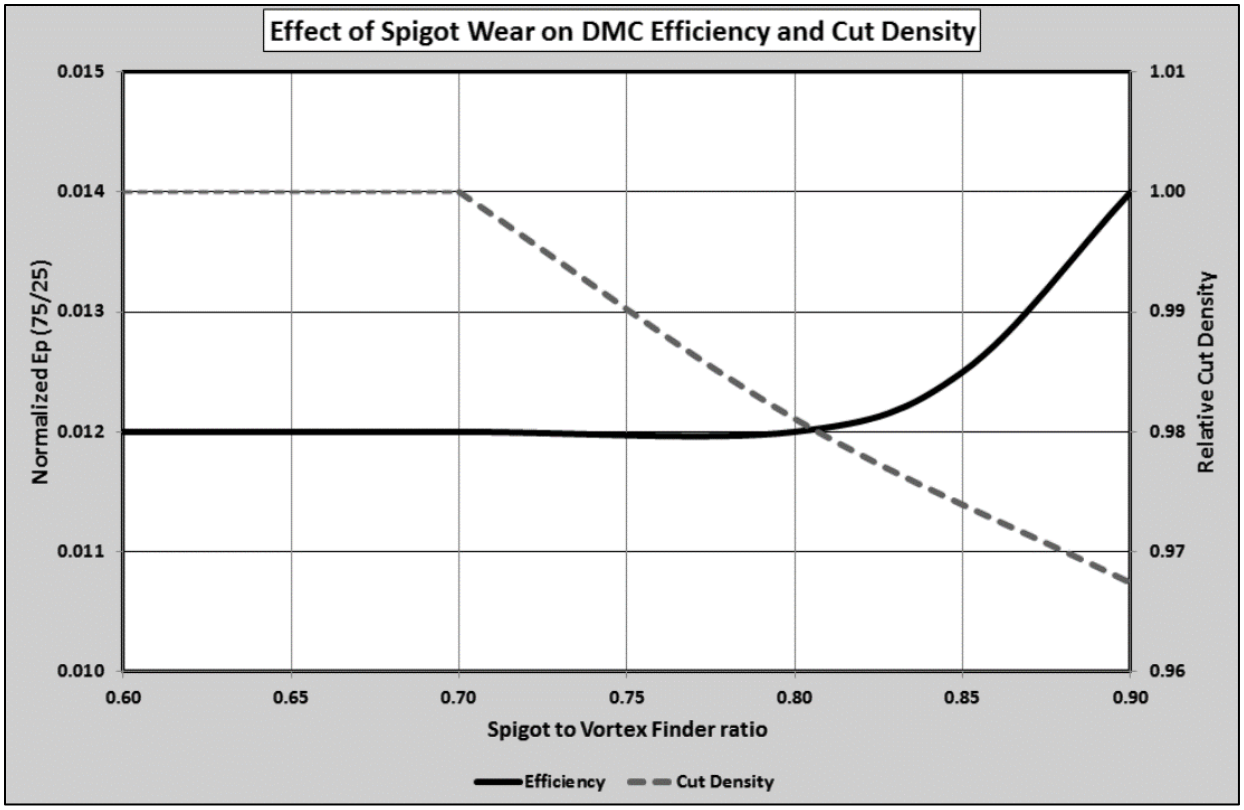


Figure 2.2: The effect of the spigot wear on cut density and efficiency (Bekker, 2014)

In Figure 2.2, the effect of a larger spigot-to-vortex finder ratio is illustrated, and it is seen that as the spigot diameter becomes larger, the efficiency starts to decline. It is also noted that cyclone cut density decreases as the cyclone spigot diameter increases (Bekker, 2014).

Jeremy Bosman (2006) compared the pipe and cyclonic densifiers in terms of their ability to ensure accurate density control and minimize medium losses. He used steady-state simulations to illustrate the performance with the addition of a correct medium bleed (Bosman, 2005). The correct medium bleed is where a fraction of the correct medium is discharged to the dilute medium sump where it combines with the dilute medium and is fed to the magnetic separators. The magnetic separator then dewaters it and the high-density concentrate is routed back to the correct medium sump. While this is not the most effective method of densification, it helps to reduce built-up grit continuously recycling in the correct medium circuit. This contamination can arise due to poor feed desliming, brittle ore or damaged panels on sieve bends and rinse and drain screens (Bosman, 2005).

The medium losses were the measured variable of the test. The manipulated variable was the deslimed feed moisture, which determined how much density control water entered the correct medium, thereby reducing the operating density. Like the study of Popplewell (1988), a basis was 100 tonnes per her (tph) deslimed feed and the magnetic separator concentrate density of 3.10 t/m^3 was used.

Only his simulated findings from the highest operating density (3.0 t/m^3) are presented in Figure 2.3 since the study will not consider low operating densities and is more interested in medium losses.

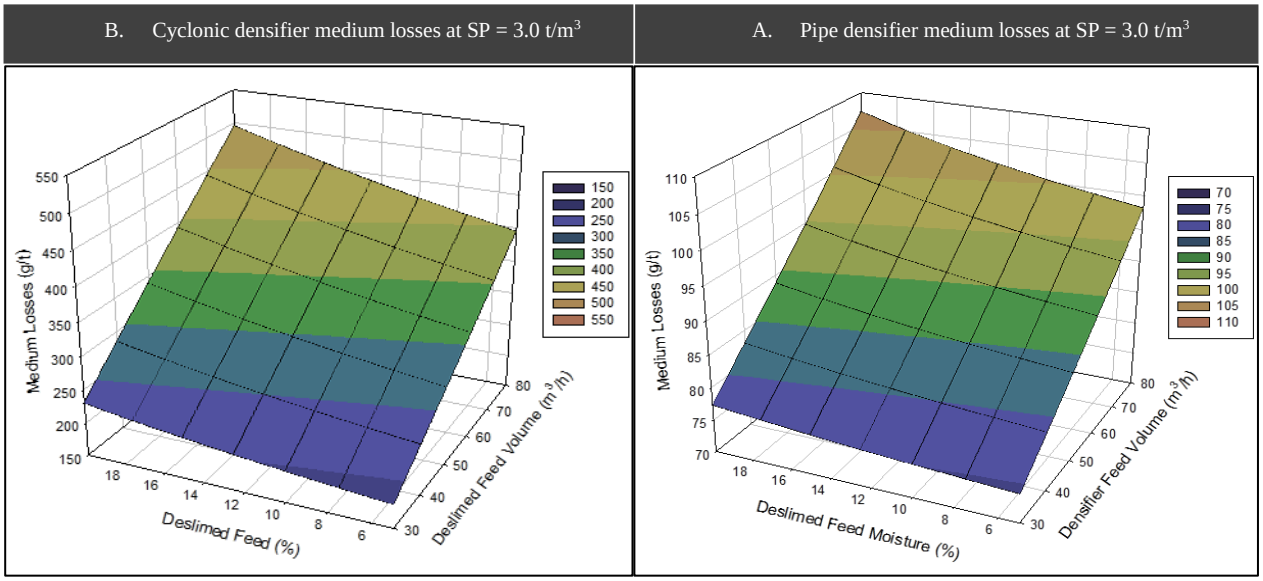


Figure 2.3: Medium losses associated with a densifier at a set point of 3.0 t/m^3 (Bosman, 2006)

From Figure 2.3 it is seen that the medium losses increase with an increase in the operating density setpoint. The medium losses in a pipe densifier are significant compared to the other methods, remaining an order of magnitude lower than those associated with the correct medium bleed and cyclonic densifier as seen in Figure 2.3. Bosman's findings highlight that the pipe densifier maintains a constant positive control water addition rate that obeys the rising density principle.

He also recommends that a DMS plant should have a correct media bleed option included in its start-up philosophy. It should be exercised only on specific occasions to bleed large volumes of water and contaminants from the correct media but should be shut off again when the operating density is near the set point (Bosman, 2006).

2.3. Computational fundamentals and modelling

2.3.1. Multiphase flow

Multiphase flow is characterized by the movement of a mixture composed of two or more distinct phases, such as gas, liquid, and solid. Each of these phases can be classified as either dispersed or continuous. In dispersed phase flows, the components exist as individual, non-connected elements with finite dimensions. They are referred to as particles. The continuous phase, on the other hand, represents a connected medium, which can either be a liquid or a gas, that carries and surrounds the dispersed phase (Crowe, 2005). Table 2.2 provides examples of different multiphase flow scenarios.

Dispersed flows can be categorized further into dense and dilute flows, each necessitating different modelling approaches to understand their behaviour. These classifications are based on the prevailing interactions within the system. In dilute flows, the motion of particles is influenced by fluid forces like drag and lift, referred to as fluid-particle interactions. In dense flows, the motion of particles is governed by collisions occurring within or between dispersed phases. These interactions are termed particle-particle interactions when they occur within the same dispersed phase and inter-particle interactions when they occur between different dispersed phases. It is acknowledged that the particle-particle and inter-particle interactions increase when the particle volume fraction exceeds 10^{-3} (Elghobashi, 1994). At this threshold, these interactions play a crucial role in shaping the behaviour of the dispersed flow.

Table 2.2: Summary of two-phase flow systems and their significance in industrial processes (Sommerfeld, 2017)

Continuous-dispersed phase	**Industrial and technical application**
Liquid-gas flows	Bubble columns, aeration of sewage water, flotation
Liquid-droplet flows	Mixing of immiscible liquids, liquid-liquid extraction
Gas-droplet flows	Spray drying, spray cooling, spray painting, spray scrubbers
Liquid-solid flows *(Considered for this study)*	Hydraulic conveying, **liquid-solid separation**, particle dispersion in stirred vessels
Gas-solid flows	Pneumatic conveying, particle separation in cyclones and filters, fluidised beds

In real-life applications, dispersed phases in multiphase flows can exhibit a wide range of physical particle properties, including various material properties and particle sizes within the continuous fluid phase. To simplify the modelling process, one might consider using an average of particle properties, such as a mean particle diameter. However, if the properties vary too extensively, modelling them as a single collection of particles can impact the dynamics and accuracy of the model. Hence, it becomes necessary to consider these particle properties and group particles into separate dispersed phases to ensure more accurate representations. Furthermore, extensions to consider three-phase flows are possible; for example, scenarios involving bubbles forming in a slurry mixture (Crowe, 2005).

This study focused on dispersed multiphase flow, wherein there is a single continuous phase of liquid and a single dispersed phase consisting of particles of the same size and material.

2.3.2. Coupling

In the context of dispersed multiphase flows, it is essential to consider both the movement of particles by the continuous fluid phase and their interactions. These inter-phase interactions can be characterized based on the concentration of particles, as this concentration influences fluid dynamic interactions, collisions, and cohesions within the carrier fluid (Sommerfeld, 2017).

Figure 2.4 demonstrates, and Table 2.3 summarizes the various types of coupling between the phases. Among them, four-way coupling is a special instance of two-way coupling. In four-way coupling, particle disturbances within the local fluid can influence other nearby particles. A classic example of this phenomenon is the drafting of a trailing particle (Crowe, 2005).

Table 2.3: Summary of different coupling levels in multiphase flows (Crowe, 2005; Sommerfeld, 2017; Elghobashi, 1994; Loth, 2000)

Coupling level	**Description**
One-way	This type of coupling involves the flow of the continuous phase affecting only the dispersed phase without any reverse effect. It is well-suited for very dilute flows, where the particles in the dispersed phase have a negligible influence on the flow in the continuous phase.
Two-way	In this scenario, there is a mutual influence between the flows in the continuous and dispersed phases. Alongside one-way coupling, the particles in the dispersed phase can affect the fluid flow, and these effects must be considered and incorporated into the model.
Four-way	This type of coupling arises when particle-particle interactions have an impact on the multiphase motion in addition to the two-way particle-fluid coupling. An illustrative example is when particle collisions influence the motion of both interacting particles.

This study employed a four-way coupling modelling approach. This approach considers interactions between particles and the fluid in both directions, modelled using drag terms to account for particle-fluid interactions. Additionally, it incorporated particle-particle interactions using solid pressure as a contributing factor.

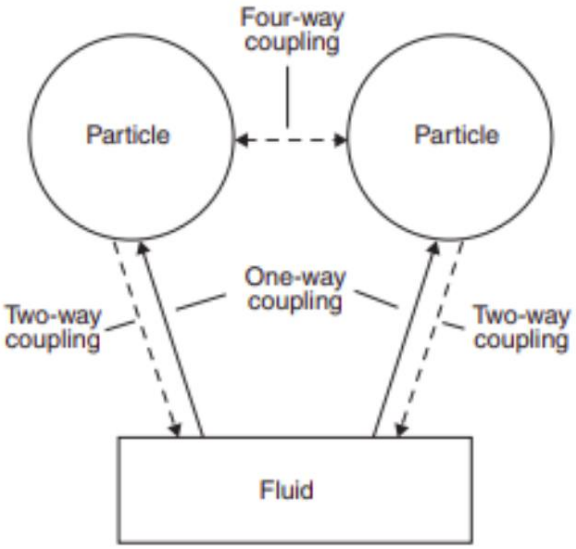


Figure 2.4: Demonstration of inter-phase interactions through coupling (Crowe, 2005)

2.3.3. Particle wear

Particles suspended in a fluid can also interact with the walls of the domain they move in, not only affecting the motion of the particles but also leading to wear and deformation of the walls. Understanding and predicting particle-laden wear in materials is a complex task that involves modelling the fluid flow, particle tracking, and employing appropriate wear prediction methods. There is no universally accepted model for predicting particle-laden wear, and most models are based on experimental data (Meng & Ludema, 1995). The prediction of wear rate depends on

several factors, including particle impact angle, impact velocity, surface material properties, and particle properties such as size, shape, and hardness (Oka & Yoshida, 2005; Oka, et al., 2005).

Meng & Ludema (1995) conducted an analysis of wear models and categorized them based on the methods of wear, which include mechanical, chemical, and thermal wear. The cutting mechanism occurs due to an oblique impact, wherein a particle strikes the surface material at shallow, grazing angles.

Deformation arises from head-on collisions of particles perpendicular to the surface of the material (Arabnejad, et al., 2015; Meng & Ludema, 1995). This study did not consider chemical and thermal wear actions. The selected mechanistic wear models focused on material loss resulting from cutting and deformation processes.

2.3.4. Computational frame of reference

There are several different computational approaches to model fluid-particle systems. These include computational fluid dynamics–discrete element method (CFD-DEM), time-driven hard sphere (TDHS), coarse-grained particle method (CGPM), coarse-grained hard sphere (CGHS), and multiphase particle-in-cell (MPPIC) (Lu, Gopalan, & Benyahia, Assessment of different discrete particle methods ability to predict gas-particle flow in a small-scale fluidized bed, 2018). It is important to understand the underlying principles, governing equations, advantages, and drawbacks of each approach.

In the literature there are mainly two types of simulations: Euler-Euler and Euler-Lagrange. Both types solve volume by using the averaged Navier-Stokes equations in a fixed frame of reference (Eulerian). The difference is that with the Euler-Euler approach, the particles are a continuum

and the volume is solved by employment of the averaged Navier-Stokes equations for both solids and liquids. The Euler-Lagrange approach tracks the motion of each particle individually (Anderson & Jackson, 1967). Hence the Euler-Euler approach holds the advantage of faster computational speed and lower cost, which was an important consideration for this study.

The first example of Euler-Lagrange simulation documented by Tsuji et al. (1993) used computation fluid dynamics coupled with the discrete element method (CFD-DEM) to model a fluidized bed. CFD-DEM allows for each individual particle's trajectory to be tracked to observe particle-particle collisions. However, due to its large computational costs, simplified models were investigated, leading to the development of the hard-sphere method.

The hard sphere method treats the particle velocity during collision based on momentum conservation. Hoomans et al. (1996) simulated the first event driven hard sphere model and Ouyang & Li (1999) investigated gas-solids flow using the TDHS approach. Even though it had an improved computational time step change, particle-particle collisions still had to be accounted for. It could be accounted for in smaller systems, but in larger dispersed systems with a higher size ratio, the efficiency was affected drastically (Andrews & O'Rourke, 1996).

The need for collating particle (parcel) behaviour in multi-dispersed systems gave rise to the MPPIC method. It avoids the search for colliding particles by using the Eulerian particle stress model to calculate particle-particle interactions. The MPPIC method is a new method that has been developed, leveraging the strengths of both Eulerian-Eulerian continuum models and Eulerian-Lagrangian discrete models. The MPPIC method efficiently transfers information between Lagrangian particles and a computational grid (Andrews & O'Rourke, 1996).

While on the grid, it readily evaluates continuum derivative terms, treating the particle phase as a fluid, and then maps these evaluations back to individual particles. As a result, the MPPIC method becomes a versatile computational tool for handling multiphase flows with varying particulate loading.

If the parcel lumping approach is coupled with DEM, it is called the coarse-grained particle method (CGPM) (Sakano, et al., 2000; Sakai & Koshizuka, 2009) and if MPPIC is coupled with TDHS it is referred to as the coarse-grained hard sphere method (CGHS) (Lu, Li, & Benyahia, 2017). The parcel-based approach significantly reduces the computation cost and need for a supercomputer. This has been used to simulate large scale processes such as solid-liquid leaching, fluidized beds and cyclones (Chu, Chen, & Yu, 2016).

In the context of Euler-Lagrange simulations, the fluid phase is represented as a continuous medium following the volume-averaged Navier-Stokes equations. On the other hand, the particles are individually tracked using the Lagrange method and they interact with the fluid phase through fixed Euler grids. The governing equations and the application of each of the five methods are detailed in the subsequent section.

2.3.5. Motion of particles

The momentum of each particle is defined by:

$$m_p \, dv_p/dt = F_{external} + F_{inter-phase} + F_{p-p} \qquad [1]$$

$$I_p \, dw_p/dt = T$$

Where

m_p is the particle mass.

I is the moment of Inertia and is calculated as $m_p d_p^2/10$.

$F_{external}$ is any external force such as gravity.

$F_{inter\text{-}phase}$ are inter-phase forces such as pressure gradient force and drag force.

$F_{p\text{-}p}$ is inter-particle contact forces.

The difference in the five methods is the calculation of the particle-particle forces. For the discrete element method (DEM), the forces between particles are computed by modelling their collisions as linear spring-mass viscously damped systems in both the normal and tangential directions. These equations are defined as follows (Lu, Gopalan, & Benyahia, 2018):

$$F_{pp} = \sum_{j=1, j\neq i}^{N} F_{ij}^{n} + F_{ij}^{t} \quad [2]$$

$$T = \sum_{j=1, j\neq i}^{N} Ln \times F_{ij}^{t} \quad [3]$$

Where

F_n is the collision force in the normal direction.

F_t is the collision force in the tangential direction.

L is the distance from particle centre to particle contact point.

For CGPM, the contact force between particles is determined using a similar approach to DEM. It assumes that all the actual particles within a computation parcel can be combined and approximated as a larger sphere with a diameter of $d_p W^{1/3}$, where W represents the number of real particles in that parcel (Garg, Galvin, Li, & Pannala, 2012).

The calculated force from this approximation is divided by W to obtain the force acting on an individual real particle within the parcel. This method allows for a coarse-grained representation of the interactions between particles, providing computational efficiency while still capturing essential aspects of the system's behaviour. The equation for the latter is transformed as follows (Lu, Gopalan, & Benyahia, 2018):

$$F_{pp} = \sum_{j=1, j\neq i}^{N} (F_{ij}^{n} + F_{ij}^{t})/W \quad [4]$$

$$T = \sum_{j=1, j\neq i}^{N} (Ln \times F_{ij}^{t})/W^{5/3} \quad [5]$$

In the context of the MPPIC method, the motion of the solid phase is represented using discrete computational parcels. The interactions and contact forces between particles in the solid phase are modelled based on the gradient of the pressure within the solid phase.

Essentially, the pressure within the solid phase is used to compute the forces between neighbouring particles. The gradient of this pressure field provides information regarding the variation and distribution of pressure, which is then used to determine the contact forces between the particles in the simulation.

By employing this approach, the MPPIC method efficiently handles the dynamics of the solid phase, enabling realistic and accurate simulations of solid-fluid interactions and complex particle behaviours. These equations are defined as follows (Lu, Gopalan, & Benyahia, 2018):

$$F_{pp} = -(\pi d_p^3/6\varepsilon_s)\nabla\tau \quad [6]$$

$$\tau = P_S\varepsilon_S^{\mathrm{x}}/\max[\varepsilon_{s,cp} - \varepsilon_s, \varepsilon(1-\varepsilon_s)] \quad [7]$$

Where

Ps is pressure [1 Pa – 100Pa]

εs, cp is the close packing limit.

ξ is also arbitrarily [2 to 5]

ε is the singularity of the close packing limit [10^{-7}]

In the current MPPIC method, the particle-particle force is directly applied at the centre of the particles, which means particle rotation is not explicitly considered in the simulation. This simplification permits more simplified calculations, but it does not account for rotational effects that might occur.

The specific values of the parameters used in the MPPIC method might be challenging to interpret physically. Instead, these parameters are employed as guidelines to determine the new velocity of a computational parcel when it approaches, exits, or becomes embedded in a close pack of other particles.

The TDHS approach breaks down the movement of particles in gas-solids flows into two distinct processes: the suspension process and the collision process. In the suspension process, external forces such as gravity and inter-phase forces influence the motion of the particles. The collision process deals with instantaneous binary collisions between particles. When updating particle

velocities during the suspension process, Newton's law of motion is employed as the governing principle:

$$m_p(dv_p/dt) = F_{external} + F_{inter-phase} \quad [8]$$

In the collision process, the velocities of particles are immediately updated through instantaneous binary collisions. When particles *i* and *j* come into contact during the collision, the change in momentum during the impact can be expressed as follows:

$$\Delta P = -m_e(1 + e_n)v_n + J_t \quad [9]$$

$$J_t = -\max\left(2/7\, m_e(1 + e_t)|v_t|, \mu m_e(1 + e_n)|v_n|\right) \times (v_t/|v_t|)$$

Where

m_e is the effective collision mass.

e_n is the normal restitution coefficients.

e_t is the tangential restitution coefficients.

J_t is the variation of momentum as result of impact in tangential direction.

μ is sliding friction coefficient.

Then, the velocity of particle *i* and *j* can be calculated as:

$$v_i = v_i - \Delta P/m_i \quad [10]$$

$$v_j = v_j + \Delta P/m_j$$

And the particle rotation of particle *i* and *j* can be calculated as:

$$w_i = w_i - (r_i n \times J_t)/I_i \quad [11]$$

$$w_j = w_j - (r_j n \times J_t)/I_j$$

Where

I is the moment of inertia calculated by $m_p d_p^2/10$.

Further details on the principles of TDHS can be found in work done by Ouyang & Li (1999) and Helland et al. (2002). More details on CGHS can be found in work done by Lu, et al. (2017), though this method is not directly referred to in this research due to the considered particle size.

2.3.6. Inter-phase forces

The inter-phase forces can be calculated as (Lu, Gopalan, & Benyahia, 2018):

$$F_{inter-phase} = \pi d_p^3/6\,(-\nabla P_f(x^i) + \beta_i/(1-\varepsilon_f) \times (v_f(x^i) - v_p^i)) \quad [12]$$

Where

$P_f(x^i)$ is the fluid pressure interpolated by the particle *i*.

$v_f(x^i)$ is the velocity interpolated by the particle *i*.

β_i is drag coefficient of particle *i*.

The Beetstra, van der Hoef, Kuipers (BVK) drag model is derived from direct numerical simulation results. The calculation of the BVK drag model is as follows (Beetstra, van der Hoef, & Kuipers, 2007):

$$\beta = 18F\mu\varepsilon_f(1-\varepsilon_f)/d_p^2 \quad [13]$$

$$F = 10(1-\varepsilon_f)/\varepsilon_f^2(1 + 1.5(1-\varepsilon_f)^{0.5} +$$

$$0.413Re_p/24\varepsilon_f^2[(\varepsilon^{-1}+3\varepsilon_f(1-\varepsilon_f)+8.4Re_p^{-0.343})/\left(1+10^{3(1-\varepsilon_f)}Re_p^{-0.5-2(1-\varepsilon_f)}\right)]$$

Where

$$Re_p = \varepsilon_f \rho_f |v_f - v_p| d_p/\mu_f \quad [14]$$

In this study, the inter-phase forces are determined by the diameter of real particles if all the real particles within a computational parcel experience the same inter-phase forces. This assumption holds well when the parcel size is small since the particles are closely spaced.

However, when the parcel size becomes significantly larger, there may be a notable discrepancy between the particles located at the centre of the parcel and those situated at its outer layer. This issue has been acknowledged and discussed by Radl & Sundaresan (2014) and Ozel et al. (2016).

Nevertheless, as this research employs a small parcel size and is focused on different solid phase models, the same drag model without further corrections is adopted to simplify the analysis and simulations.

2.3.7. Kinetic theory of granular flow

To account for particle-particle interactions experienced in the four-way coupling of this model, this thesis adopts the concept of the kinetic theory approach of granular flow. This approach is inspired by the kinetic theory of dense gases defined by Chapman (2014). It involves modelling densely packed macroscopic particles as microscopic molecules exhibiting constant random motion. By using this concept, the thermal temperature is replaced with a granular flow temperature, where the temperature term represents the energy associated with the random motion of the particles (Cloete, Johansen, & Amini, 2012). The theory posits that particles at a

high-volume fraction will exert a solid pressure, which prevents them from becoming excessively densely packed together (Gidaspow, 1994).

The Eulerian-Lagrangian model incorporates the concept of kinetic theory of granular flow (KTGF) to represent particles as averaged quantities, serving as an intermediate approach between the two-fluid Eulerian-Eulerian model and the DEM. In this model, the fluid dynamics are solved on a fixed Eulerian grid, while representative particles are tracked using the Lagrangian framework. These representative particles maintain discrete particle information while also being represented on the Eulerian grid as averaged quantities.

The mapping of representative particles onto the Eulerian grid groups them, treating them as point particles traveling through the domain. However, unlike in DEM simulations, they cannot directly interact. Instead, their interactions are accounted for indirectly through their effects on the fluid phase.

The volume fraction of the particle phase is represented by interpolating the volume fraction that the particles would occupy within each cell. This information is then mapped onto the Eulerian grid, while particle-particle interactions are modelled using the KTGF concept. This approach maintains discrete particle information, but in an averaged form, and it incorporates particle-particle interactions through solid pressure parameterizations.

Furthermore, this method reduces computational costs compared to using the DEM to achieve the same objective (Chen & Wang, A comparison of two-fluid model, dense discrete particle model andcfd-dem method for modeling impinging gas–solidflows, 2014). The sub-grid scale

fluctuation of particle velocities around the mean particle velocity is based on Maxwell's velocity distribution function (Jenkins, 1992; Ding & Gidaspow, 1990).

$$f(c-u_p) \propto (1/2\pi\Theta)^{\frac{3}{2}} \exp\left(-((c-u_p)\cdot(c-u_p))/2\Theta\right) \quad [15]$$

$$\Theta = \langle \left\| c-u_p \right\|^2 \rangle /3$$

Where

c is the mean particle velocity within the Eulerian reference.

Θ is the granular temperature to the kinetic theory of gasses.

The solid stress tensor $\overline{\overline{\tau_p}}$ is derived from Lun et al. (1984) and given as:

$$\overline{\overline{\tau_p}} = -p_p \mathrm{I} + \propto_{\mathrm{P}} \mu_P \nabla^2 U_P + \alpha_P(\lambda_{\mathrm{P}} - 2/3 \times \mu_P)\nabla \cdot u_P \mathrm{I} \quad [16]$$

Where

μ_p is the shear viscosity.

λ_p is the bulk viscosity.

u_p the average viscosity of the vector.

The solid pressure, shear, and bulk viscosity, which together constitute the solid stress tensor, are all determined using the KTGF approach. These quantities depend on the conservation of kinetic energy within the particles, known as the granular temperature.

The granular temperature represents the individual particle velocity, which is not averaged as it is in Eulerian-Eulerian simulations, where particles are not treated as a continuous medium. The mean particle velocity *c* is calculated as the average velocity.

Both the shear and bulk viscosity arise from the momentum exchange resulting from the translation and collision between particles. The shear viscosity consists of both the kinetic and collisional components of particle-particle momentum exchange, while the bulk viscosity represents the resistance of particles to compression and expansion.

The shear viscosity, denoted as μ_p is formed by modelling the collisional and kinetic parts using expressions from Gidaspow (1994):

$$\mu_p = \mu_{col} + \mu_{kin} \quad [17]$$

$$\mu_{col} = 4/5 \times \alpha_p d g_0 (1 + e)(\Theta/\pi)^{0.5}$$

$$\mu_{kin} = (10\rho_p d\sqrt{\Theta\pi}/96\alpha_p(1+e)g_0) \times \left(1 + 4/5 \times g_o \mu_p (1+e)\right)^2$$

Where

μ_{col} is the collisional part of the shear viscosity.

μ_{kin} is the kinetic part of the shear viscosity.

The bulk viscosity, which quantifies the resistance of particles to compression and expansion, is expressed as shown below based on Lun et al. (1984):

$$\lambda_p = 4/3 \times \alpha_p^2 \rho_p d g_0 (1+e)(\Theta/\pi)^{0.5} \quad [18]$$

Where

d is the particle diameter.

e is the restitution coefficient for particle collision.

The solid pressure, denoted as p_p, is determined using expressions from Lun, et al. (1984) and Ding and Gidaspow (1990), and it is given by:

$$p_p = \alpha_p \rho_p \Theta + 2\rho_p(1 + e)\alpha_p^2 g_0 \Theta \quad [19]$$

Where

g_0 is the is the radial distribution given by:

$$g_0 = \left(1 - \left(\alpha_p / \alpha_{max}\right)^{1/3}\right)^{-1} \quad [20]$$

The radial distribution function describes the likelihood of particle collisions at a specific packing ratio and serves as a mechanism to prevent particles from becoming excessively densely packed. It is influenced by a maximum packing fraction denoted as α_{max} and is designed to increase significantly as the solid volume fraction approaches this maximum value. For this study, the value of αmax is set to 0.6 based on research conducted by Ding and Gidaspow (1990).

While particle-particle shear stress becomes more significant at high particle volume fractions near the walls, the crucial aspect of particle-particle behaviour in this thesis lies in its ability to describe the deceleration of particles as they approach the wall. This deceleration is attributed to the solid pressure, which emulates the effects of particle-particle collisions near the wall, ultimately reducing the influence of particle-wall collisions.

2.3.8. Wear mechanism principle and models

The wear of materials due to solid particle impingement poses significant risks to the integrity of industrial processes involving the transport of slurries in pipes or complex geometries like DMS cyclones and densifiers. While the use of solid transport as slurry mixtures proves efficient and cost-effective for short to medium distances, the abrasive nature of slurries leads to substantial

wear. Considering the nature of wear in densifiers, uneven wear distribution across the inlet and vortex finder are identified, with some areas experiencing significantly more wear than others.

Wear occurs when particles collide with a surface, resulting in the formation of scars. The shape and size of these scars, caused by individual impacts, depend on various parameters, such as surface material properties, particle size, velocity, and impact angle. Wear mechanisms are categorized based on the ductility of the surface material, distinguishing between ductile and brittle behaviour. Finnie's model proposed in 1960 explains erosion in ductile materials, suggesting that it results from micro-cutting caused when a particle impacts the surface at a low angle, creating a crater. In contrast, erosion in brittle materials arises from crack formation when a particle strikes the brittle surface, leading to lateral and radial cracks. Subsequent impacts cause these cracks to grow, eventually dividing the surface into smaller pieces that are removed by subsequent particle impacts (Parsi, 2015).

Wear models for erosion have been extensively studied in pipes and elbows. However, despite these studies, no single predictive equation applicable to a wide range of scenarios has been found. These models can generally be categorized as empirical, mechanistic, or CFD/MPPIC-based. Empirical models are straightforward to implement but have limited applicability beyond the specific conditions they were derived from. Mechanistic models, based on the physics of erosion, have been developed for single-phase and multiphase flows. However, some of these models have limitations, such as neglecting turbulence effects (Ip, 2021).

The third type of wear model is computational-based (CFD/MPPIC) erosion modelling, which allows the study of erosion effects under different parameters and complex geometries.

Computational-based erosion modelling involves flow modelling, particle tracking, and application of particle trajectory information to the erosion equation (Ip, 2021).

For this thesis, a semi-mechanistic wear model was chosen, focusing on cutting and deformation contributions, and integrated into the CFD/MPPIC-based wear modelling framework. Existing wear equations in the literature are diverse, with empirical models relying on experimental data and mechanistic models based on the underlying physics and wear mechanisms.

Several other CFD-based wear prediction models have been proposed by researchers such as Chen et al. (2004), Zhang et al. (2007), and Agrawal et al. (2019). Chen, et al. (2004) employed a one-way coupled approach with a fixed computation mesh, defining the erosion ratio as the mass loss of the material divided by the mass of particles impacting the wall and is given by:

$$ER = AF_s V^n f(\theta) \quad [21]$$

Where

A is the empirical constant for specific materials.

V is the particle impact velocity.

F_s is the particle sharpness factor.

n is the empirical coefficient.

$f(\theta)$ is the impact angle function as derived from the eroded material type.

The particle rebound model is employed to describe particle-wall collisions. It incorporates an impact-angle-dependent coefficient of restitution, which is derived from empirical data. Notably, Grant and Tabakof (1975) and Forder et al. (1997) are examples of studies utilizing such models.

Zhang, et al. (2007), compared various CFD-based wear models against experimental data, with the model used being one-way coupled and lacking particle-particle interactions. The results revealed that the erosion model of Oka and Yoshida (2005) demonstrated the best correlation with the experimental data. Interestingly, Zhang et al. (2007) observed that however the coefficient of restitution is defined had minimal to no impact on particle trajectory and wear, thereby contrasting the findings of Chen et al. (2004).

Additionally, Agrawal et al. (2019) developed a one-way coupled wear model capable of mesh deformation based on the calculated erosion rate for each node. Like Zhang et al. (2007), they utilized the E/CRC erosion model for their simulations given by:

$$\mathrm{ER} = \mathrm{C}(\mathrm{BH})^{-0.59}\mathrm{F}_s\mathrm{V}_\mathrm{p}^{\mathrm{n}}\,\mathrm{F}(\alpha) \qquad [22]$$

$$\mathrm{F}(\alpha) = 5.4\alpha - 10.11\alpha^2 + 10.93\alpha^3 - 6.33\alpha^4 + 1.42\alpha^5$$

Where

C is the empirical constant.

BH is the Brinell Hardness of the material.

α is the particle impact angle.

One limitation of the previously discussed CFD-based wear models lies in the reliance on empirically derived wear equations. Although these equations are user-friendly, there are uncertainties associated with extrapolating these correlations to different material properties, potentially leading to inaccuracies.

In contrast, a more suitable alternative for the wear modelling framework is the semi-mechanistic impingement wear model proposed by Arabnejad et al. (2015). This model combines both

mechanistic and empirical approaches and specifically accounts for mechanical wear in ductile materials arising from cutting and deformation mechanisms. To ensure relevance to the oil and gas industries, target materials were carefully selected based on their distribution density, hardness, and prevalence in these sectors. By employing this semi-mechanistic model, a more comprehensive and accurate representation of wear behaviour can be achieved, addressing some of the limitations of purely empirical approaches.

Arabnejad et al. (2015) demonstrated that the ratio of contact increased significantly, from 0.4 for sand particles to 1 for rounded glass beads. Consequently, this alteration in contact ratio influenced the angle dependency, resulting in higher impact angles that led to increased wear. Moreover, the particle sharpness factor was found to play a crucial role in determining the overall wear effectiveness. Research by Bahadur and Badruddin (1990) and Liebhard and Levy (1991) revealed that angular particles can induce wear up to an order of magnitude greater than that caused by spherical particles.

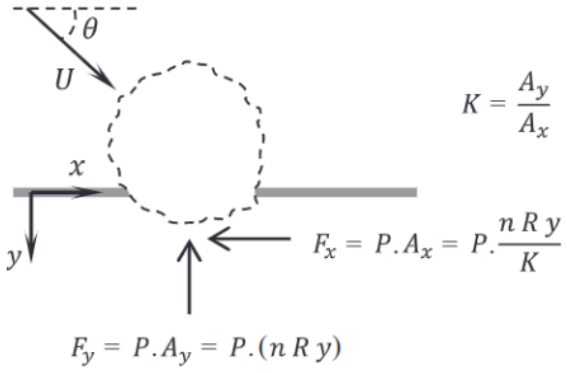


Figure 2.5: Force balance of a non-uniform particle interacting with a surface (Arabnejad, et al., 2015).

Furthermore, this model introduces a new approach in which the particle's shape influences the ratio of contact parameter used to determine the critical impact angle. Figure 2.5 depicts the forces that oppose the particle as it cuts into the surface, where K represents the empirically defined ratio of vertical to horizontal contact area between the particle and the surface, given by A_y and A_x, respectively (K is experimentally obtained for each specific material). This differs from the mechanistic model of Finnie and McFadden (1978), where the ratio of contact is assigned as a constant. The forces resisting the motion of the particle in the vertical and horizontal directions are denoted by F_y and F_x, respectively, and their equations of motion (Finnie & McFadden, 1978) are defined as:

$$m(d^2y/dt^2) = PnRy = 0 \quad [23]$$

$$m(d^2x/dt^2) = PnRy/K = 0$$

$$P = \sqrt{Hv}$$

Where

m is the particle mass.

P is the pressure of the material flow.

Hv is the Vickers hardness of the material.

N is the is the ratio of the contact and removed area.

R is the particle size.

According to Andrews (1930) contact stress is given as:

$$A_y = 2\pi Ry \quad [24]$$

The integral of the above-mentioned derived equations using the particle position and inbound velocity gives:

$$y = Usin(\theta)/\beta \sin(\beta t) \quad [25]$$

$$x = tUcos(\theta) - Usin(\theta)[t\beta - \sin(\beta t)]/K\beta$$

$$\beta = \sqrt{PnR/m}$$

Where

θ is the impact angle.

U is the inbound velocity.

Therefore, the volumetric wear loss is defined as follows:

$$Vol_C = \int A_x dx = mF_s C U^{2.41} f(\theta)/2\sqrt{Hv} \quad [26]$$

$$f(\theta) = \begin{cases} 1/2K^2(Ksin(2\theta) - \sin^2(\theta)), & \theta < \tan^{-1} K \\ \cos^2(\theta), & \theta \geq \tan^{-1} K \end{cases}$$

Where

C is the cutting coefficient.

Fs is the particle sharpness factor.

Experimental studies have determined that $Vol_C \propto U^{2.41}$. The volumetric loss because of deformation is given as (Bitter, 1963):

$$Vol_D = 0.5 \times mF_s g(\theta)/\epsilon \quad [27]$$

$$g(\theta) = \max(0, (Usin(\theta) - U_{tsh})^2)$$

Where

ϵ is the deformation coefficient.

$g(\theta)$ is angle function for deformation of erosion.

U_{tsh} is the threshold velocity (considered to be negligible from experimentation).

The total volume loss term resulting from an impact event, considering both cutting and deformation mechanisms for erosion, is a combination of the relevant expressions above. This equation can be represented as:

$$W_i = mF_s/2\left[U^{2.41} f(\theta)/\sqrt{Hv} + g(\theta)/\epsilon\right] \quad [28]$$

In this model, the value of K is experimentally determined to be 0.4 for materials eroded with sand. The sharpness of the particle plays a crucial role in causing volume loss during collisions with the wall, and thus, the sharpness factor F_s varies from 0.25 for rounded particles to 1 for fully sharp particles (Bitter, 1963).

Mass transport due to wear was not considered in this study. This decision was motivated by the significant increase in computational cost and complexity that would have arisen from including the material lost through wear. Moreover, the wear introduced by the flow is greater than the wear from the scoured surface. Additionally, relying on empirical data in the model equations might have introduced uncertainties when extrapolating the model to materials with different properties. Although the wear equation used is based on a semi-mechanistic model, there is still a reliance on empirical data for certain material properties.

3. METHODOLOGY

The experimental approach is subdivided into two phases, namely, Phase I: Experimental Testing and Phase II: Numerical Model.

3.1. Phase I: experimental testing

The practical test work was conducted at the Sishen mine medium drum plant, module 741. This module has a duty (F741G7210) and a standby (F741G7220) densifier feed pump. The duty and standby lines are fitted respectively with F741G5810 and F741G5820 pipe densifiers.

3.1.1. Experimental setup

Experimental testing entailed changing physical components of the test densifier, F741G5820, to meet the required set objectives. Table 3.1 explains the changes that were made for the test.

Table 3.1: Comparison between current and test densifiers

Category	Current densifier setup	Test work densifier
Functional equipment	F741G5810 densifier	F741G5820 densifier
Supplier	HMA (Red)	Multotec (Green)
Model	200NB	PC200
Unit design	Single modelled unit: polyurethane	Stainless steel casing with weep holes with a replaceable polyurethane liner
Pulley arrangement	355-mm motor pulley by 500-mm pump pulley	355 mm motor pulley by 500 mm pump pulley
Vortex finder size	32 mm	30 mm, 40 mm and 45 mm

The experimental setup is shown in Figure 3.1. The inlet was sampled from the drain valve of the densifier pump F741G7210 for the HMA unit and at pump F741G7220 for the Multotec unit. The underflow was sampled at the underflow pipes of each of the units and the overflow was sampled at the overflow launder. Only one densifier was in production for the respective tests.



Figure 3.1: Experimental setup for the HMA and Multotec densifiers

The outcomes are defined in a matrix in line with the suggested experimental method used by Bosman in his study in 2011. The design of experiments (DoE) for the physical experiments is shown in Table 3.2.

Run 1 to Run 9 were performed on the Multotec PC200 pipe densifier with varying vortex finder diameters and feed densities. Run 10 to Run 12 were performed on the HMA 200NB pipe densifier with similar volumetric capacity at varying feed densities to compare the current practice to the test work.

Table 3.2: Experimental DoE for the tube densifier by test work

Operating flow rate 50 m³/h		**Wear and efficiency outputs**								
		$SG_{O/F}$	$SG_{U/F} - SG_{O/F}$	Wear rate (mm/day)	$SG_{O/F}$	$SG_{U/F} - SG_{O/F}$	Wear rate (mm/day)	$SG_{O/F}$	$SG_{U/F} - SG_{O/F}$	Wear rate (mm/day)
		Feed density = 3.4 t/m³			**Feed density = 3.5 t/m³**			**Feed density = 3.6 t/m³**		
Multotec vortex diameter (mm)	30	Run_1	Run_1	Run_1	Run_4	Run_4	Run_4	Run_7	Run_7	Run_7
	35	Run_2	Run_2	Run_2	Run_5	Run_5	Run_5	Run_8	Run_8	Run_8
	40	Run_3	Run_3	Run_3	Run_6	Run_6	Run_6	Run_9	Run_9	Run_9
HMA vortex diameter (mm)	32	Run_{10}	Run_{10}	Run_{10}	Run_{11}	Run_{11}	Run_{11}	Run_{12}	Run_{12}	Run_{12}

3.1.2. Operating flow and pressure onset conditions

At Sishen there were no permanent flow meters installed before the densifier units. However, a temporary SAFSONIC Doppler flow meter was used to get an estimation flow around the experimental module F741G5810. The inlet flow rate recorded ranged from 43–74 m^3/h on the densifier inlet. A nominal flow rate of 50 m^3/h was used as the inlet flow rate to the numerical model by considering the pump curve along with the experimentally determined mode. The

flows on the underflow used as inputs ranged from 171–193 m^3/h. A nominal flow rate of 180 m^3/h was recorded as the underflow flow rate.

The theoretical pump curve seen in Appendix A was used to establish an estimate inlet pressure to the densifier unit. The calculations to determine the upper and lower pressure boundaries are as follows:

$$P_{LoLo} = \rho g h = 3300 \frac{kg}{m^3} \times 9.81 \frac{m}{s^2} \times 14m = 453\ kPa \quad [29]$$

$$P_{HiHi} = \rho g h = 3600 \frac{kg}{m^3} \times 9.81 \frac{m}{s^2} \times 14m = 494\ kPa \quad [30]$$

The inlet pressure was verified by a pressure gauge installed on the inlet of the densifier to be ranging between 430–500 kPa on the unit. The average pressure of 460 kPa was used as in input constant for Phrase II.

3.1.3. Early failure detection

The casing design of the densifier should incorporate weep holes to detect early failures (Chiu, 2012). The pressure and densifier pump current can also be monitored to detect early failures. Weep holes installed on the Multotec PC200 densifier provide a systematic release of pressure. Fluid leaking from the weep holes indicates densifier parts failure (Baboo, 2006), as shown in Figure 3.2 (B). If a deviation is noted, then an investigation of the densifier parts should be triggered.

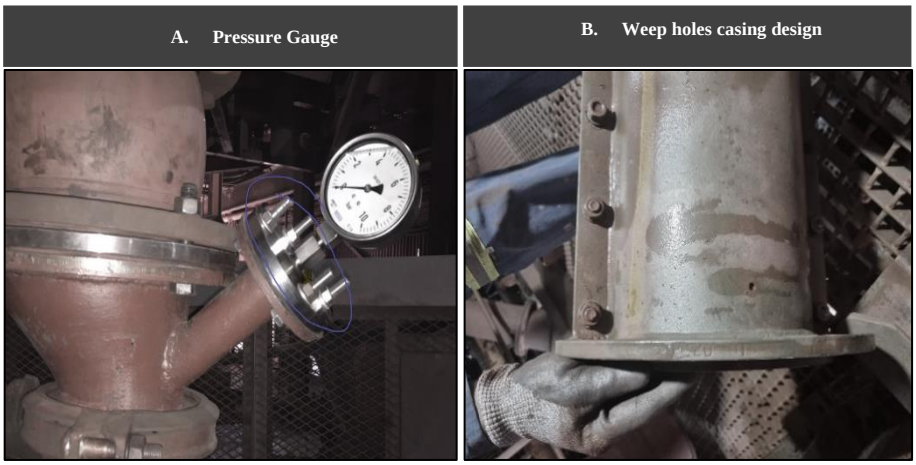


Figure 3.2: Early failure detection applications (Napier-Munn, et al., 1995)

3.2. Phase II: numerical model

Design by MPPIC modelling entails defining the medium fluid dynamics inside a densifier to determine the behaviour of the high-density medium under different scenarios.

MPPIC was selected because of the following advantages in comparison with the other four methods:

1. It works well for dense particle flow (low loss of fidelity) considering a high-density feed is used of 3.10 t/m^3 and higher.
2. Statistical weighing makes it simple to employ DEM fundamental principles.
3. It enables repeat runs to be done due to its fast computational speed.

Limitations that needed to be considered included that MPPIC requires insight to properly select empirical parameters for the solid stress model and the setup of the model requires forethought to preserve mass.

3.2.1. CFD-MPPIC integration

CFD provides specific insights to identifying high wear zones based on the fluid dynamic principles. It uses numerical algorithms adhering to the Navier-Stokes laws to compute fluid behaviour consequent to internal states such as velocity, density, pressure, and shear stress. It also provides a three-dimensional insight of the design making it convenient to comprehend the mathematics applied. The extended fine mesh domain was configured according to Table 3.3.

Table 3.3: CFD fine mesh inputs

Parameter	Measurement
Liquid volume flow rate at inlet	50 m^3/h
Grid cell count	305 000
Particle injection rate	100 000 particles/second
Vortex diameter	30, 35, 40 mm
Feed density at inlet	3.4, 3.5, 3.6 t/m^3
Particle density	6.95 t/m^3

The Solid Works STEP file for the 200-mm densifier was provided by HMA (the supplier of the pipe densifiers) and its internal volume was used. The apparatus setup from the STEP file is shown in Figure 3.3 with internal volume in blue.

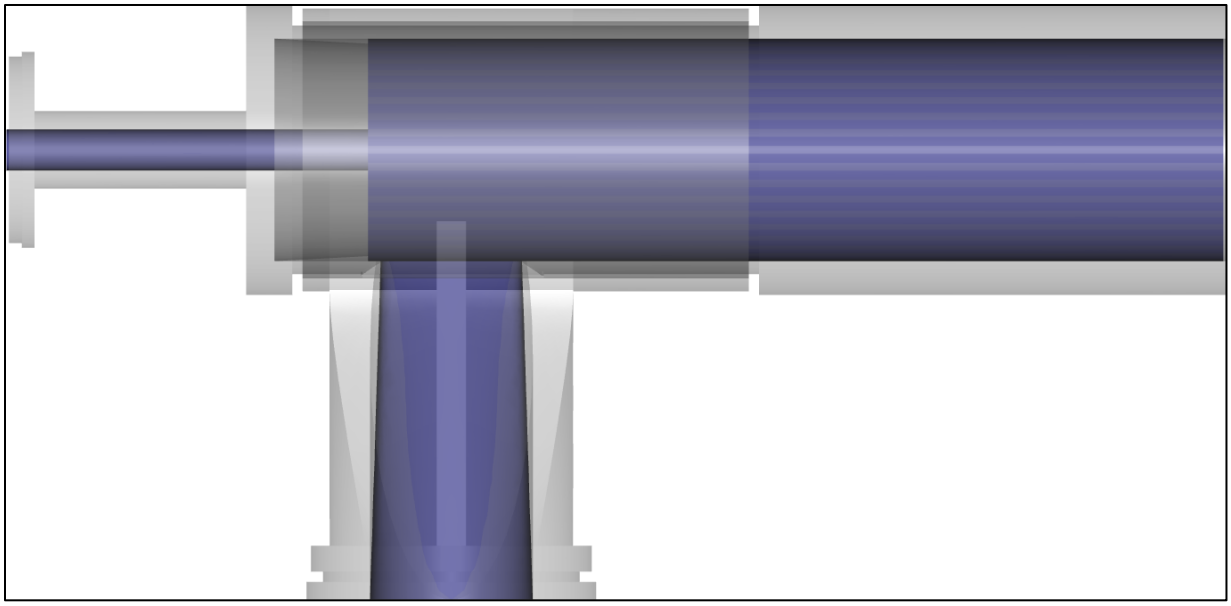


Figure 3.3: Provided densifier model with internal volume in blue

The apparatus was only half the size of the actual densifier for the computational analysis. To conduct CFD analysis of the flow through the full domain, the internal volume was extended such that the inlet and the underflow were identical. Figure 3.4 illustrates the full domain along with the flow boundaries.

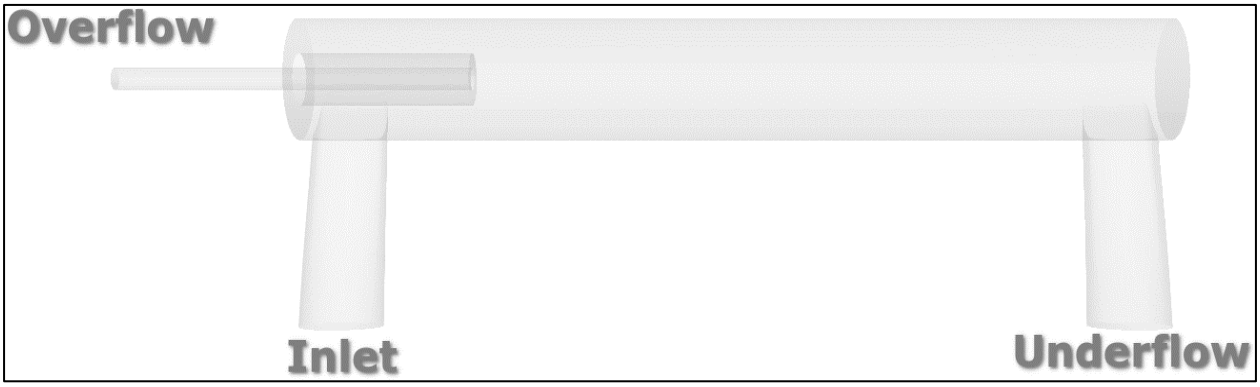


Figure 3.4: Full internal domain for computational analysis

The CFD software used for the analysis was OpenFOAM v2012. OpenFOAM is an open-source CFD framework that is highly extensible and includes several physics-based models. To simulate the flow of the feed, a multiphase solver was required to model both the fluid and the particle transport within the feed. Therefore, the MPPICFoam solver within the OpenFOAM framework was selected to perform the simulation. MPPICFoam is a transient solver for the coupled transport of a single kinematic particle cloud including the effect of the volume fraction of particles on the continuous phase. MPPIC modelling is used to represent collisions without resolving particle-particle interactions. Since the solver models the particle-particle interaction on a bulk basis, it is ideally suited for feed flow where the particle count is substantially high.

A hybrid between structured and unstructured tetrahedral mesh was used in the CFD analysis. This was to balance the computational efficiency but to still have geometric flexibility for the irregular design of the densifier. The mesh was refined in the overflow pipe region. To capture the viscous effects accurately near the walls, boundary layer mesh was generated throughout the internal surfaces of the densifier. The mesh details are shown in Figures 3.5 and 3.6. The mesh comprises of 0.313 million cells.

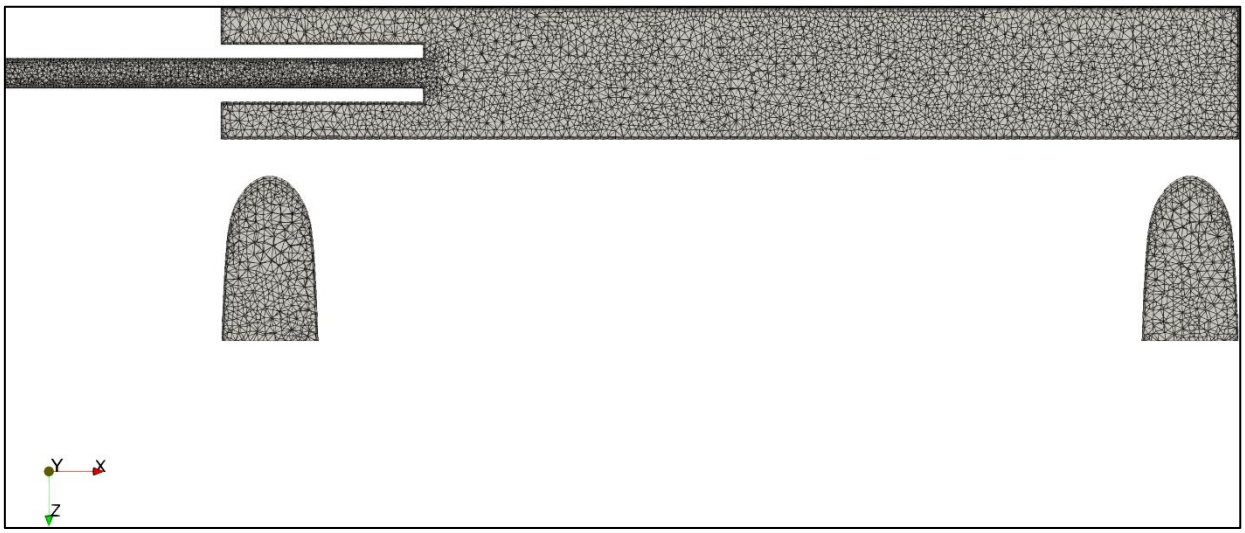


Figure 3.5: Mesh cross-section

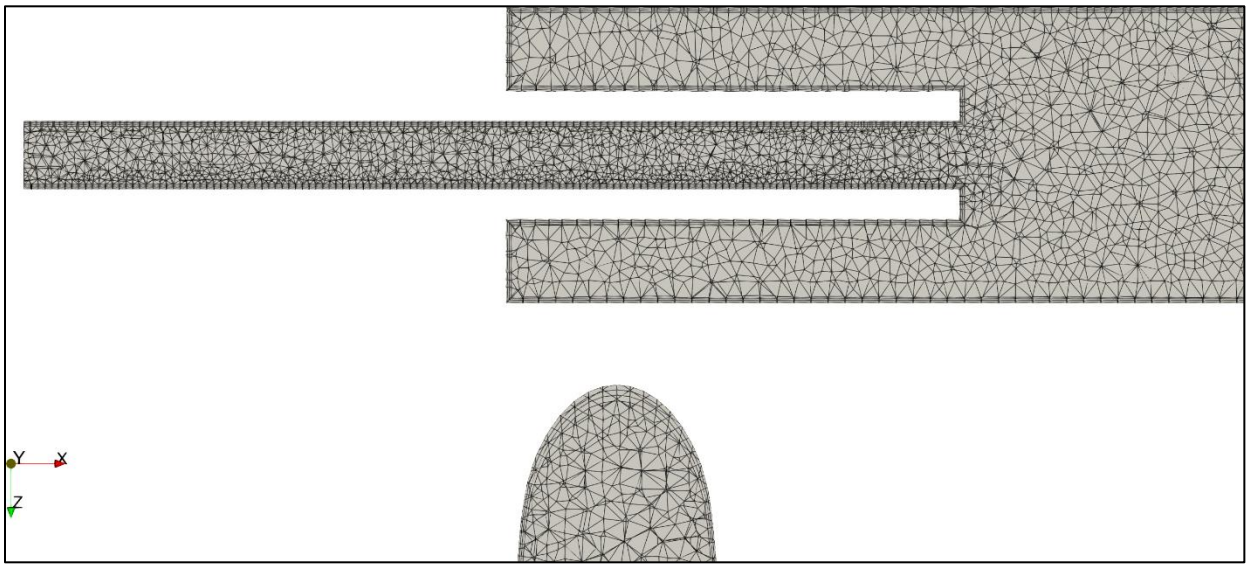


Figure 3.6: Mesh refinement in the overflow region

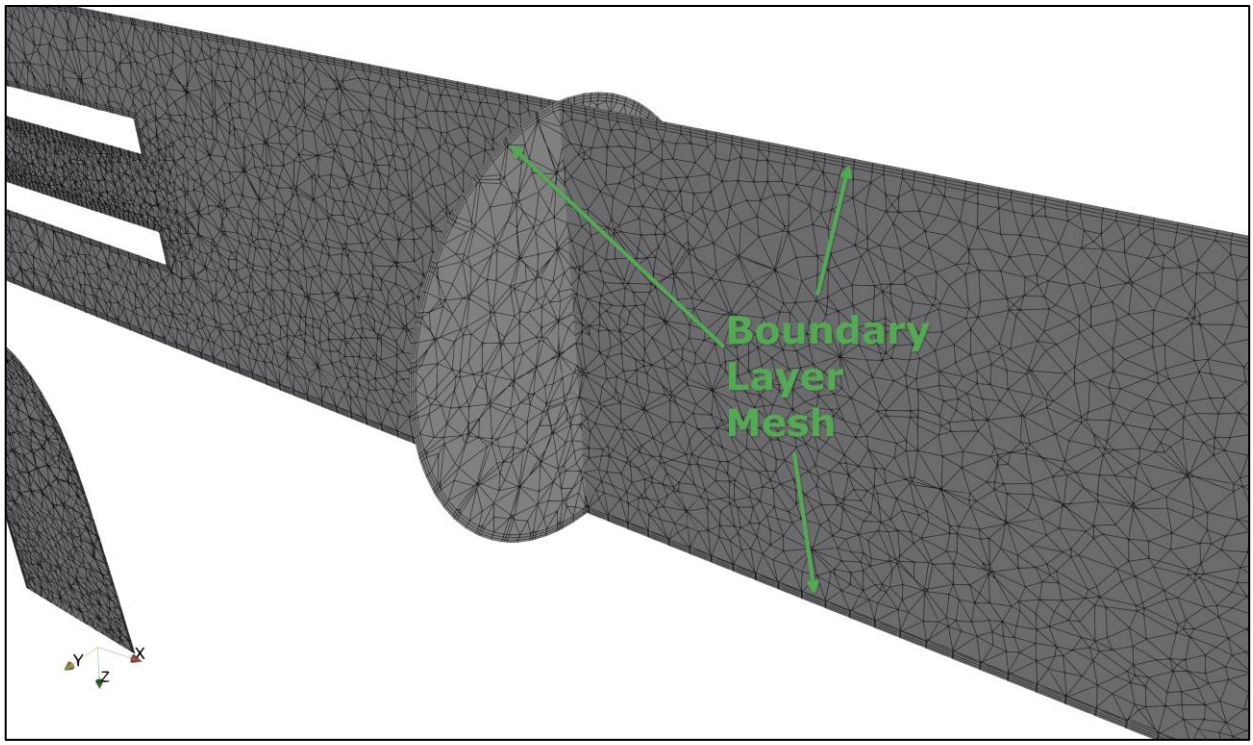


Figure 3.7: Boundary layer mesh near the surfaces

3.3. Domain setup

In the MPPICFoam approach, the liquid and solid phases are tracked in the Eulerian and Lagrangian frameworks, respectively. The number of solid particles contained in the feed can be estimated from the feed density, liquid density, particle mass and particle size distribution.

Given that the liquid is water with a density of 1.00 t/m^3 and the feed has the density of 6.95 t/m^3, the number of particles flowing with the feed per second can be estimated. Since the particle size is of the order of microns, there are billions of particles flowing with the feed per second. It is computationally not feasible to model the flow with full particle count.

Since the particles exhibit bulk behaviour, particles can be grouped into clouds, also known as parcels or numerical particles. Each parcel commonly consists of several real particles, reducing the computational costs remarkably. For the simulations in this project, 100 000 numerical particles per second were injected into the liquid at the inlet.

This particle count is sufficient to capture the bulk behaviour of the particles in the flow as well as to model drag forces exhibited on the internal densifier surface. The particle drag model is based on the Gidaspow drag model, which in turn is a combination of the Wen-Yu and Ergun drag models (Schiller & Naumann, 1935).

The combination of the Wen-Yu and Ergun drag models is given as follows:

$$F_{D,Wen-Yu} = \frac{3}{4}\frac{(1-\propto_c)\mu_c \propto_c Re_p}{d_p^2} C_D \propto_c^{-2.65} \quad [31]$$

$$F_{D,Ergun} = (150\frac{1-\alpha_c}{\alpha_c} + 1.75Re_p)\frac{(1-\alpha_c)\mu_c}{d_p^2} \quad [32]$$

$$F_D = F_{D,Wen-Yu} \text{ if } \alpha_c \geq 0.8$$

$$F_D = F_{D,Wen-Yu} \text{ if } \alpha_c < 0.8$$

With

$$Re_p = \frac{\rho_c |u_{rel}| d_p}{\mu_c} \quad [33]$$

Where

F_D = Drag force per carrier-fluid velocity [kg/s].

C_D = Particle drag coefficient.

Re_p = Particle Reynolds number.

μ_c = Dynamic viscosity of carrier at the cell occupying particle.

d_p = Particle diameter.

ρ_c = Density of carrier at the cell occupying particle.

u_{rel} = Relative velocity between particle and carrier.

α_c = Volume fraction of carrier fluid.

The flow within the densifier was quite dense due to the presence of particles and the overall volume flow rate was moderate.

3.4. Boundary and operating conditions

3.4.1. Inlet boundary

For velocity boundary conditions, *flowRateInletVelocity* was used. This boundary condition enforces a constant volumetric flow rate for the fluid. The *zeroGradient* boundary condition was used for pressure. This meant that the pressure was free to adjust at the inlet as the velocity boundary condition was enforced.

3.4.2. Underflow and overflow boundary

The *inletOutlet* boundary condition was used for velocity. It is a generic outflow boundary condition that allows the specification of inflow in case of return flow. Fixed pressure was applied at both boundaries. Since pressure is relative, the kinematic pressure of zero was applied at both boundaries. This was done to drive additional fluid through the overflow and to improve densifier separation efficiency.

3.4.3. Operating conditions

The fluid was introduced at the inlet with the volumetric flow rate of 50 m^3/h. Particle flow of 100 000 particles per second were also injected at the inlet. The fluid and the particles were allowed to escape from the underflow and overflow boundaries based on the progression of simulation. The entire domain was decomposed among 28 processors using scotch partitioning for enabling MPI parallelized simulation. All the walls are modelled as no-slip isothermal surfaces.

3.5. CFD-MPPIC solver

To simulate the flow of the feed, a multiphase solver was needed to model the fluid and the particle transport within the feed. The fluid phase was solved as a laminar flow in the current solver. The flow within the densifier is dense due to the presence of particles and the overall

volume flow rate is moderate. For such flows, a laminar model was used with good accuracy. The motion of the fluid phase in the presence of discrete phase (solid particles) is governed by Navier-Stokes Equations.

For the particle phase, one approach is to use the discrete element method (DEM). In the DEM frame, all the particles in the computational domain are tracked in the Lagrangian manner, and each particle's trajectory is explicitly solved based on momentum conservation of translational and angular accelerations (Li, Peng, Zhu, Zou, & Yin, 2017). All the forces acting on each particle are solved as separate equations. These forces include collision forces, frictional forces, fluidic forces and other body forces such as gravity, electrostatic and magnetic forces.

The DEM approach is highly accurate since it resolves the domain at the particle scale and thus can capture phenomena like particle clustering, percolation, and wave propagation within particles. The major disadvantage of this approach is that it is computationally intensive, and the time step must be extremely small to calculate the force interaction at particle level accurately. As the particle size decreases, the time-step also needs to be reduced proportionately to resolve particle-particle interaction. The DEM approach is better suited for cases where the particle size is of the order of millimetres and the number of particles is in the range of a few million (for instance modelling grain transport in a medium-sized silo). For these reasons, DEM was deemed unsuitable for the study, and we chose to go with MPPIC.

Like DEM, MPPIC is based on translational force balance formulated for individual particles. In the case of MPPIC, each particle represents a parcel of particles. MPPIC parcels are also subjected to forces such as gravity, drag force, pressure force, and Saffman force. The main difference is that in MPPIC, inter-particle collisions are modelled as empirical mean models

instead of as explicit particle-particle interactions. This significantly improves the computational efficiency and time-step size requirements without substantial loss of accuracy.

Since the solver models the particle-particle interaction on a bulk basis, it is ideally suited for feed flow where the particle count is substantially high. The coupling between the CFD and MPPIC solver is based on the momentum exchange term between the fluid phase and the particle phase. Typically, the most important contribution to fluid-particle momentum exchange comes from the drag force, which depends on the particle volume fraction.

3.6. Solver settings

3.6.1. Fluid solver

The *pimpleFoam* solver was employed for the simulation. This is a transient solver for incompressible, turbulent flow of Newtonian fluids. It uses PIMPLE iterative solver, which is a combination of PISO and SIMPLE algorithm. The *GAMG* solver was used for pressure with a Gauss-Seidel smoother. The *smoothSolver* was used for velocity with *symGaussSeidel* smoother.

Two pressure-corrector loops were used within each PIMPLE iteration, meaning that the algorithm solved the pressure equation twice while correcting the momentum in each loop. For incompressible flows, the advised value is usually 2 or 3 for the number of corrector loops. A momentum predictor was also enabled so that the velocity field was approximated from the solution of the momentum equation assembled from the previous time-step pressure field. It was enabled to achieve faster convergence.

3.6.2. Particle solver

Given that the liquid is water with density 1.00 t/m^3 and the feed has the density 6.95 t/m^3, the number of particles flowing with the feed per second can be estimated. Since the particle size is of the order of microns, there are billions of particles flowing with the feed per second. The particles exhibit a bulk behaviour and are grouped into a cloud which are often called parcels or numerical particles.

Each parcel consists of several real particles reducing the computational costs remarkably. The properties of the parcels are determined based on feed density and bulk behaviour. This parcel count is sufficient to capture the bulk behaviour of the particles in the flow as well as to model drag forces exhibited on the internal densifier surface. The particle size distribution in the simulations is specified as the probability density function equivalent to the size distribution of the Exxaro coarse particles. The probability density function of size and mass is shown in Figure 3.8 respectively. For each individual parcel, the forces induced by drag, pressure gradient, gravity, and collisions (bulk) are modelled in the simulations.

The elasticity coefficient of 1 is used for parcel-wall interaction. The Ergun-Wen-Yu drag model is used to compute interphase momentum transfer terms and to account for the drag forces and the buoyancy forces (Ergun, 1952). The implicit packing model is used to determine the particle-particle interaction. It utilizes Harris and Crigton's model for computation of inter-particle stresses (Harris & Crighton, 1994). The stochastic collisional isotropy model is used to compute isotropic velocity distribution at the particle scale (O'Rourke & Snider, 2012).

The particle size distribution in the simulations is specified as the probability density function equivalent to the size distribution of the Exxaro coarse particles (Halvorsen, Plessis, & Woudberg, 2006). These inputs were verified by sampling are given in Table 3.4.

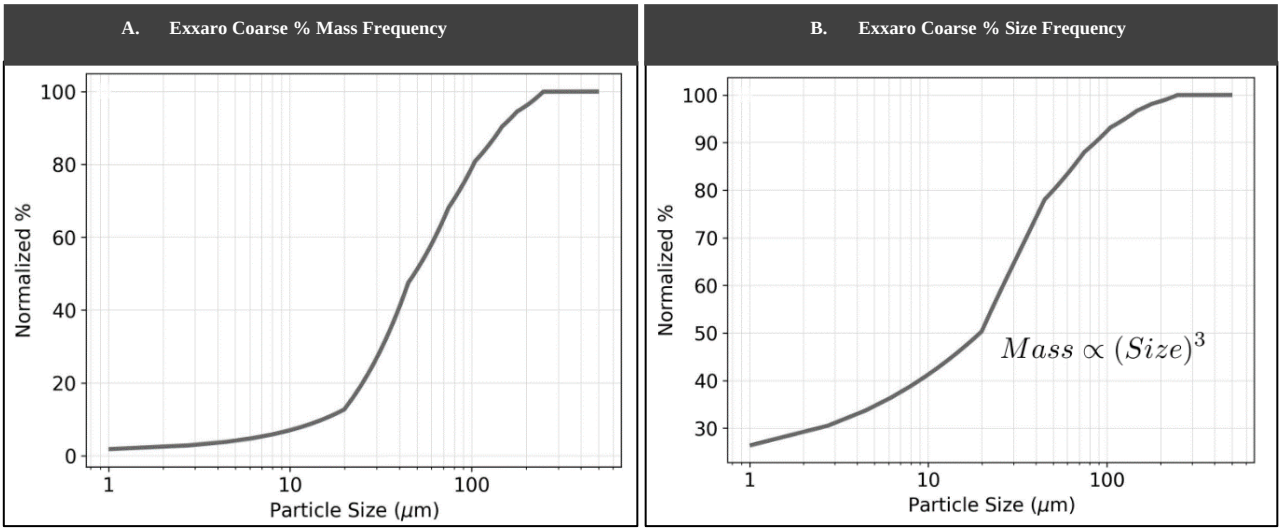


Figure 3.8: Normalized percentage mass frequency and (B) percentage size frequency

The other required input for the MPPIC was the percentage solids of the ferrosilicon mixture at differing inlet densities.

Table 3.4: Samples taken to verify the percentages of solid and magnetic material in the feed

Measured inlet density t/m^3	% Solids	% Magnetic material
3.404	41.74%	74.28%
3.504	43.48%	82.73%
3.598	45.22%	92.28%

3.7. Convergence criteria

In the particle-fluid coupled simulations, statistical convergence was observed as there was continuous interaction between the particle and fluid phases. Each simulation was run for 10 seconds of real-world time. Adaptive time-stepping based on a maximum Courant number of 2 was used. This resulted in time-stepping size of the order of 2×10^{-4} s.

The particle transport Courant number was also restricted to 1 ensure to volume-fraction convergence. In the duration of 10 seconds, multiple cycles of repeating flow characteristics were obtained, indicating statistical convergence. The L2 norm of velocity magnitude converged to 5×10^{-4} and the particle volume-fraction converged to 5×10^{-4}.

3.8. Design of experiments

Both CFD and MPPIC inputs were integrated to provide the desired outcome. The DoE is used to guide and compare the results to the practical experiments. The experimental setup in terms of the DoE for the linear modelling is tabulated in Table 3.5 (Bosman, 2011).

Table 3.5: Experimental DoE for the tube densifier by modelling

Operating flow rate 50 m³/h		**Shear stress and efficiency outputs**								
		$SG_{U/F}$	$SG_{U/F} - SG_{O/F}$	Shear Stress (Inlet)	$SG_{U/F}$	$SG_{U/F} - SG_{O/F}$	Shear stress (inlet)	$SG_{U/F}$	$SG_{U/F} - SG_{O/F}$	Shear stress (inlet)
		Feed density = 3.4 t/m³			**Feed density = 3.5 t/m³**			**Feed density = 3.6 t/m³**		
Vortex Diameter (mm)	30	Run_1	Run_1	Run_1	Run_4	Run_4	Run_4	Run_7	Run_7	Run_7
	35	Run_2	Run_2	Run_2	Run_5	Run_5	Run_5	Run_8	Run_8	Run_8
	40	Run_3	Run_3	Run_3	Run_6	Run_6	Run_6	Run_9	Run_9	Run_9

4. RESULTS AND DISCUSSION

The results of the experimental findings and numerical outputs will be discussed separately, followed by a combined discussion to compare and relate the findings at the end of the chapter in Section 4.3.

4.1. Phase I: experimental test work

4.1.1. Densifier inlet wear rate

The highest fluid velocity was observed at the inlet. This is also where the highest shear stress was measured according to the numerical model. Hence, for the practical results, the inlet was measured from ear to ear in its cross section, as illustrated in Figure 4.1 (B). The cross-section was measured and used to calculate the wear rate of the test units.

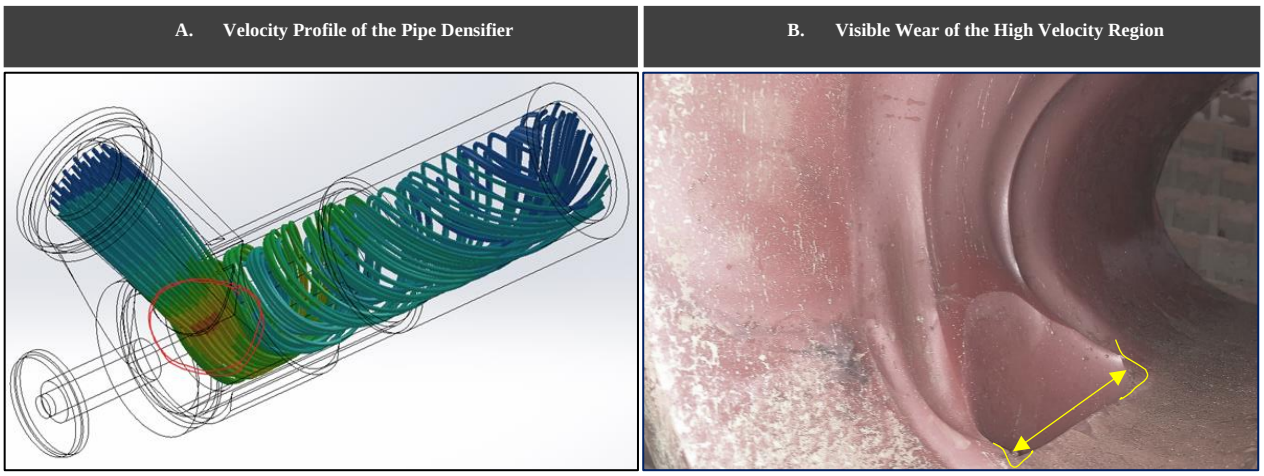


Figure 4.1: Velocity-wear profile of the densifier inlet

The inlets, outlets, and main bodies of each test unit were new at the start of the test. The test densifiers were opened on four occasions to inspect the wear rate of the typical high-wear areas at the inlet. These observations from the Multotec PC200 are tabulated below in Table 4.1.

In total, from ear to ear, the Multotec PC200 test unit wore 4.84 mm over a period of 121 days from new to failure, giving an average wear rate of 0.04 mm/day.

Table 4.1: Experimental wear rate results of the Multotec PC200 inlet

Inspection day	Inlet measurement (ear-to-ear)	Wear rate
Day 1 (Start)	56.00 mm	New
Day 48	56.15 mm	0.03 mm/day
Day 56	56.70 mm	0.04 mm/day
Day 63	57.00 mm	0.05 mm/day
Day 121 (End)	60.84 mm	0.04 mm/day

The HMA test unit wore at an average rate of 0.31 mm/day. That is approximately 15 mm over a period of seven weeks from new to failure. Therefore, the Multotec test densifier outlasted the HMA test densifier 2.5 times in terms of mean-time-to-failure (MTTF).

Table 4.2: Experimental wear rate results of the HMA 200NB inlet

Inspection day	Inlet measurement (ear-to-ear)	Wear rate
Day 1 (Start)	105.00 mm	New
Day 48 (End)	119.85 mm	0.31 mm/day

4.1.2. Densifier separation efficiency

The amount of solid material removed is a function of the inlet fluid velocity and the ratio of spigot-to-vortex open area (Bekker, 2014). Only the latter was varied for the purpose of these

tests and recorded in Table 4.3. The fluid velocity remained constant as the densifier feed pump pulley sizes and inlet open area remained constant.

Table 4.3: Summary of the average overflow densities for the Multotec and HMA test units

Vortex diameter	**Overflow density at a feed density of 3.4 t/m^3**	**Overflow density at a feed density of 3.5 t/m^3**	**Overflow density at a feed density of 3.6 t/m^3**
50 mm (Multotec)	2.20 t/m^3	2.51 t/m^3	2.72 t/m^{3*}
40 mm (Multotec)	1.76 t/m^3	2.05 t/m^3	2.25 t/m^3
35 mm (Multotec)	1.54 t/m^3	1.80 t/m^3	2.01 t/m^3
30 mm (Multotec)	1.33 t/m^3	1.58 t/m^3	1.75 t/m^3
32 mm (HMA)	1.10 t/m^3	1.35 t/m^3	1.51 t/m^3

**Densification instability and misplacement*

The results indicate that the HMA test densifier has a lower overflow density at a vortex finder diameter of 32 mm than the Multotec at a 30-mm vortex finder diameter. This indicates that the HMA 200NB densifier performs better in terms of dewatering.

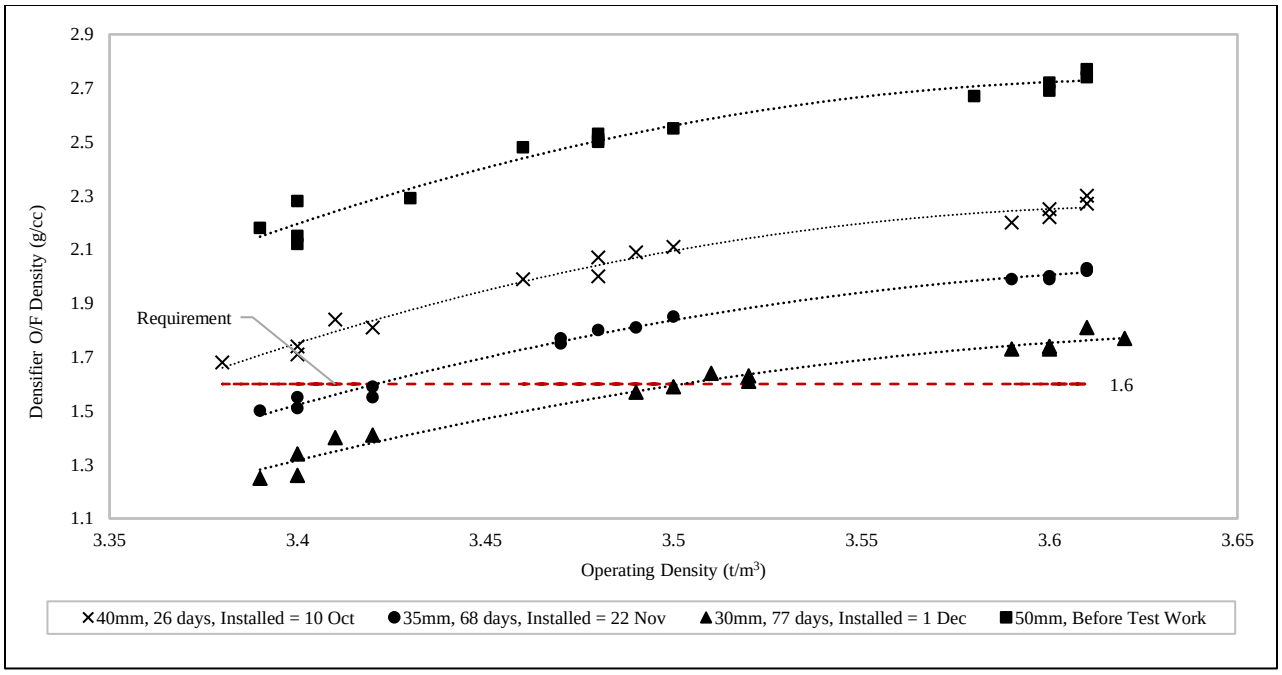


Figure 4.2: Multotec densifier O/F vs SG at different vortex finder diameters

Figure 4.2 illustrates the results of the densifier overflow density compared to the feed density of each experiment. The maximum allowable density is indicated by the requirement line. Any overflow density above this line, would make the test impractical as it is prone to overloading the downstream magnetic separation with a high concentration of magnetic material, which will lead to poor performance and FeSi loses.

The detailed experimental findings with the green and yellow operating ranges for the HMA 32-mm vortex finder and the best performing Multotec experiment (with a 30-mm vortex finder) are compared in Figure 4.3.

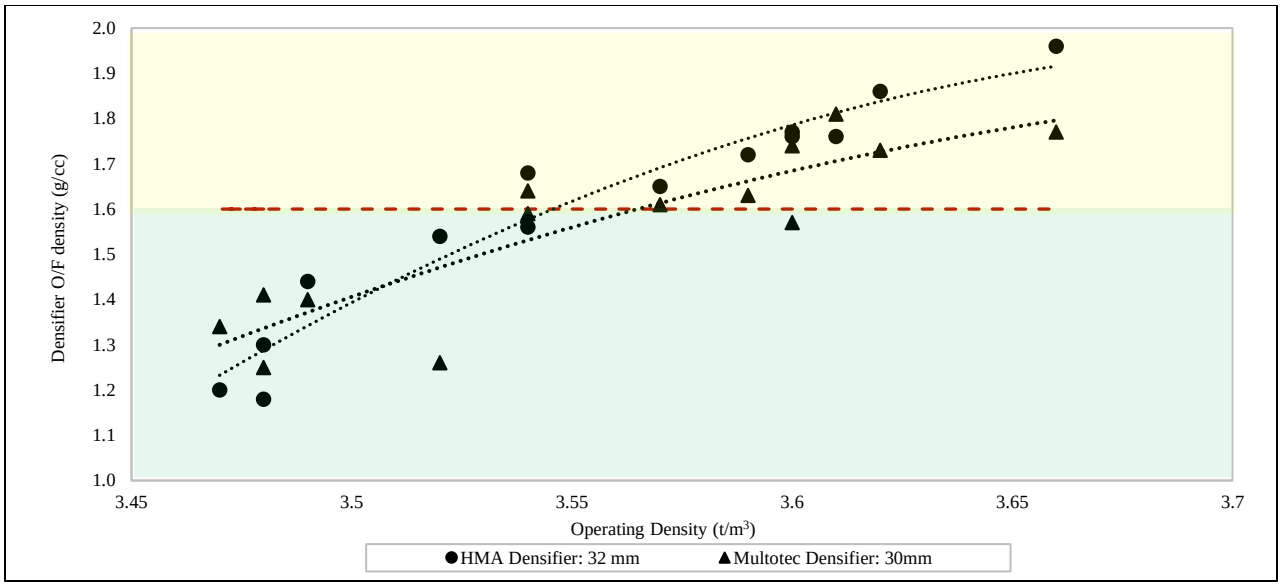


Figure 4.3: Multotec and HMA densifier overflow density vs operating density

Efficient dewatering is important since it impacts the downstream process of magnetic separation. The purpose of the magnetic separator is to recover 99.8% of the ferrosilicon medium back into the process (Weldhagen, 2015).

The densifier overflow with the addition of control water is fed to the magnetic separator. A further study was then performed to quantify the impact of the magnetic separator feed densities on its allowable feed density. The detailed experimental findings with the green and yellow operating ranges for the densifier overflow densities are highlighted in Figure 4.4.

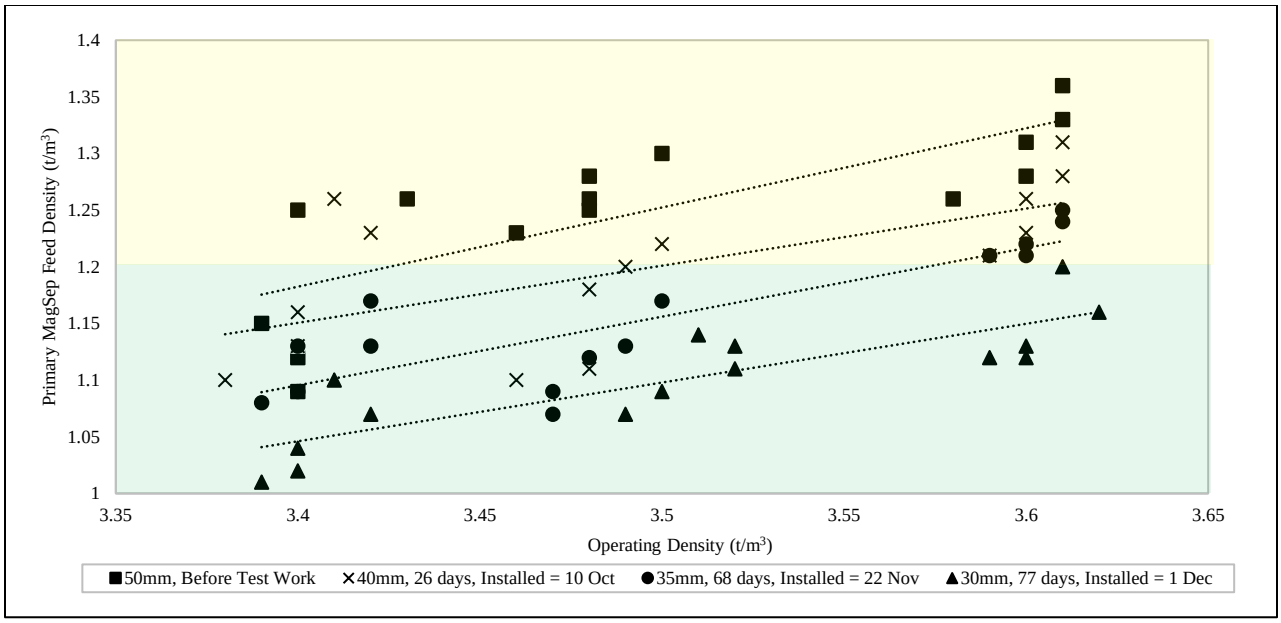


Figure 4.4: Magnetic separator feed density vs operating density

It is important to note that the Malvin magnetic separator is designed for a feed density below 1.20 t/m^3 (Weldhagen, 2015). The results in Figure 4.4 show that the Multotec PC200 densifier with vortex finder diameters of 30 mm and 35 mm fall within the acceptable ranges for magnetic separation. This is with the condition that the control water to the dilute sump stays open and supplies a constant flow of water.

The risk of not having the control water open was further investigated. The purpose was to quantify the impact of the control water on the magnetic separator effluent losses under differing densifier overflow densities.

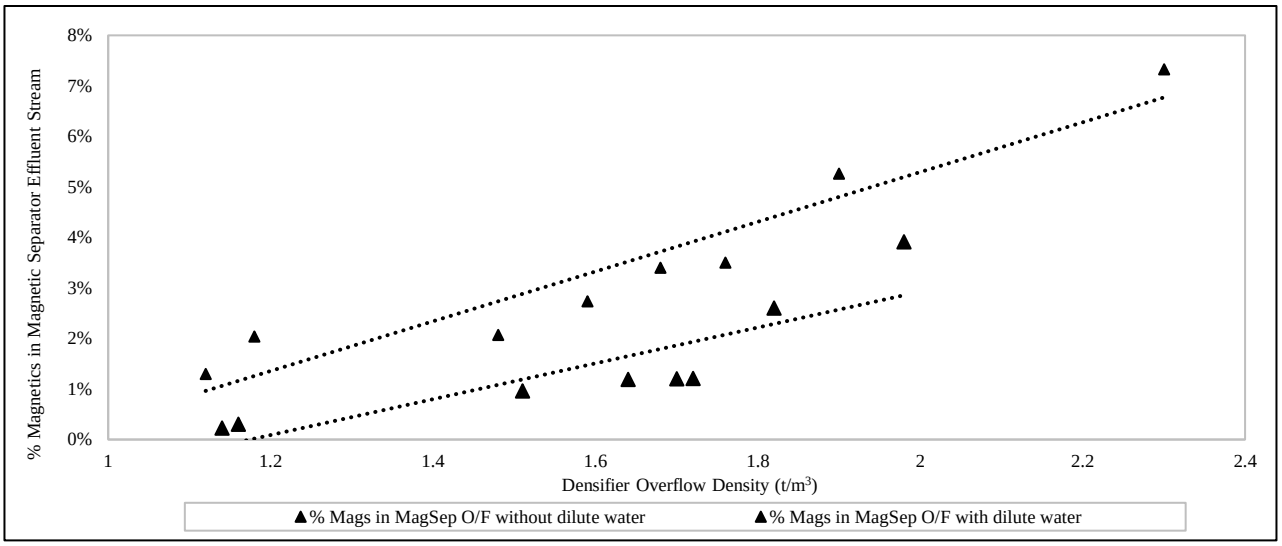


Figure 4.5: Percentage MagSep magnetic losses with and without control water

Under normal operating conditions, not adding control water leads to an approximate 1% increase in magnetic losses in the effluent stream. Higher operating densities cause higher densifier overflow densities, with larger magnetic losses. This is because the effective open or contact area of media to the magnetic separator drum decreases as the media thickens. Hence, dilution control water has a larger impact on the magnetic separator performance at higher densifier overflow densities.

4.1.3. Experimental summary

The DoE outcomes for the experimental testing are summarized in Table 4.4 in terms of densifier overflow density, density differentials and wear rate on the inlet.

Table 4.4: Experimental DoE for the tube densifier by test work

Operating flow rate 50 m³/h		**Shear Stress and efficiency outputs**								
		$SG_{O/F}$	$SG_{U/F} - SG_{O/F}$	Wear rate (mm/day)	$SG_{O/F}$	$SG_{U/F} - SG_{O/F}$	Wear rate (mm/day)	$SG_{O/F}$	$SG_{U/F} - SG_{O/F}$	Wear rate (mm/day)
		Feed density = 3.4 t/m³			**Feed density = 3.5 t/m³**			**Feed density = 3.6 t/m³**		
Multotec vortex diameter (mm)	30	1.33	2.17	0.05	1.58	2.02	0.05	1.75	1.95	0.06
	35	1.54	1.96	0.04	1.80	1.80	0.04	2.01	1.69	0.05
	40	1.76	1.74	0.02	2.05	1.55	0.04	2.25	1.45	0.04
HMA vortex diameter (mm)	32	1.10	2.40	0.28	1.35	2.25	0.31	1.51	2.19	0.34

In terms of wear rate and MTTF, the Multotec PC200 densifier is superior as it outlasts the HMA densifier by a factor of 2.5.

In terms of dewatering and separation efficiency, the HMA 200NB is superior as shown by its increased density differentials. The HMA densifier with a 32-mm diameter vortex finder provides a lower densifier overflow density of an average 0.23 t/m^3 lower than the Multotec PC200 best-performing 30-mm vortex finder.

The results indicate that a 30-mm vortex finder for the Multotec PC200 and a 32-mm vortex finder for the HMA 200 NB both satisfy the outcome of the test. This further study on the downstream magnetic separation process proved that the effect of higher overflow densities is countered by the addition of control water, making both options satisfactory for operation.

4.2. Phase II: numerical model results

The extended fine mesh domain configuration yielded the results to be discussed below. Only the three selected runs of the DoE will be discussed. The remaining runs can be found in Appendix

4.2.1. Run 1: 30-mm vortex finder and 3.4 t/m^3 feed SG

The volume flow rate of the water, cumulative particle flow, particle flow rate and effective density from the first run are presented in Figure 4.6.

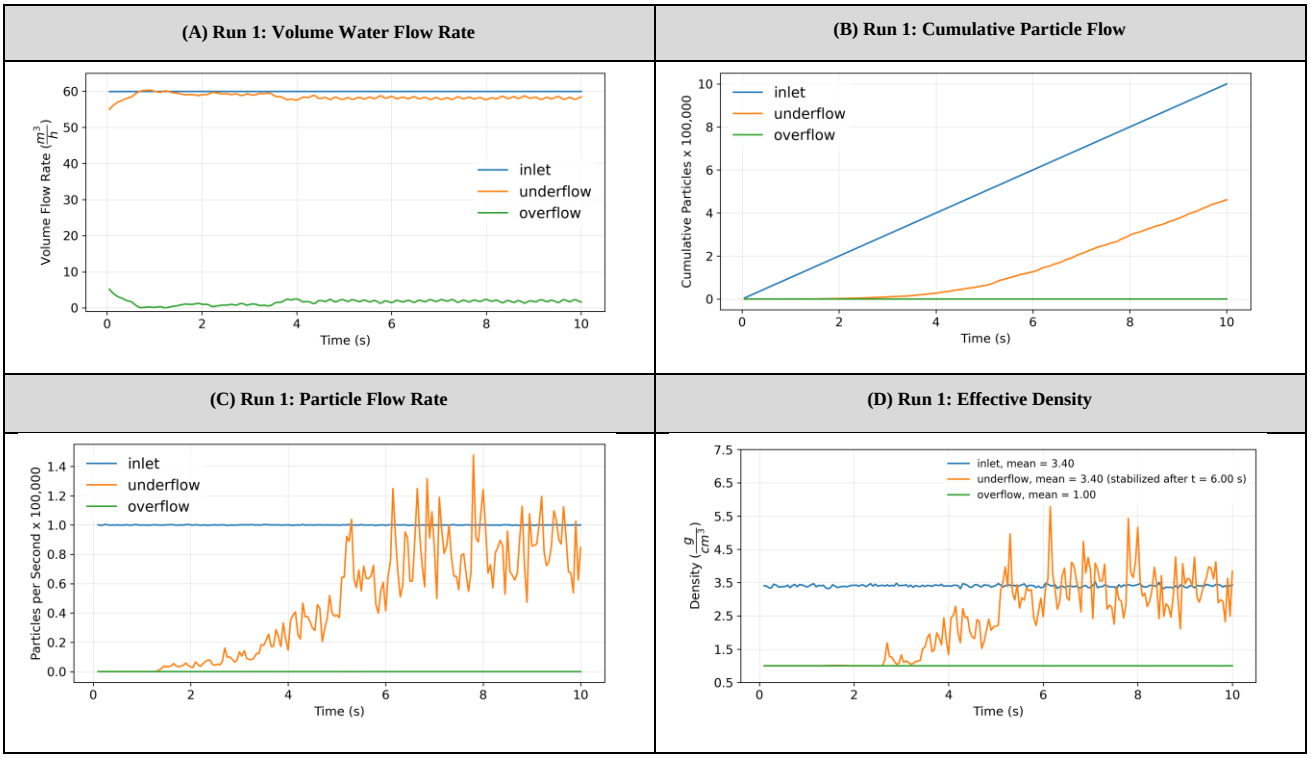


Figure 4.6: Model flow and density outputs of Run 1 in the DoE

The results in Figure 4.6 indicate no significant densification of the medium using a 30-mm vortex finder at a feed density of 3.4 t/m^3. The densifier exhibits minimum particle flow rate and water flow rate through the overflow. The shear stress on the densifier is shown in Figure 4.7.

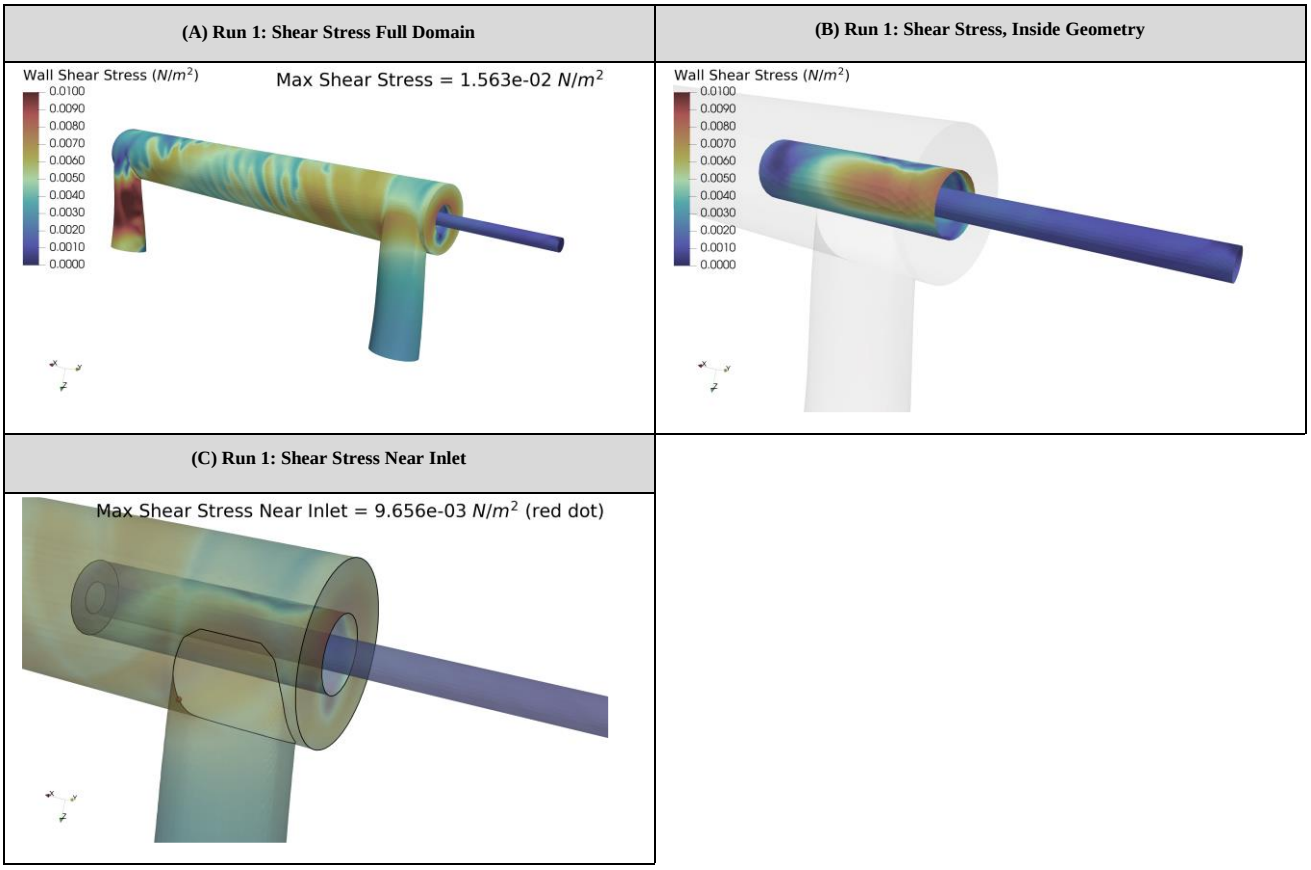


Figure 4.7: Shear stress outputs of Run 1 in the DoE

From the results it is evident that due to most particles exiting the outlet at a feed density of 3.4 t/m^3 and a vortex finder diameter of 30 mm, the wall stress at the outlet is the highest at a value of 1.563e^{-2} N/m^2. The maximum shear stress at the inlet is lower at 9.656e^{-3} N/m^2. Therefore, when running under these conditions, the outlet is expected to wear first.

A summary of Run 1 to Run 3 is given in Table 4.5 below which entails all the runs completed at a 3.4 t/m^3 feed density with vortex finder diameters of 30 mm, 35 mm and 40 mm.

Table 4.5: Model outputs of Run 1 to Run 3 in the DoE

Operating flow rate 50 m^3/h		Density$_{U/F}$	Cum. particles $_{O/F}$	Cum. particles $_{U/F}$	Max shear stress $_{Inlet}$
Vortex diameter (mm)	30	3.40	5	462030	9.656e-03
	35	3.74	257	469561	9.706e-03
	40	3.89	420	491121	9.770e-03

It is evident that opening the vortex finder diameter improves densification on the unit at a feed density of 3.4 t/m^3; however, it does increase the shear stress on the inlet.

4.2.2. Run 5: 35-mm vortex finder and 3.5 t/m^3 feed SG

The volume flow rate of the water, cumulative particle flow, particle flow rate and effective density from the fifth run are presented in Figure 4.8.

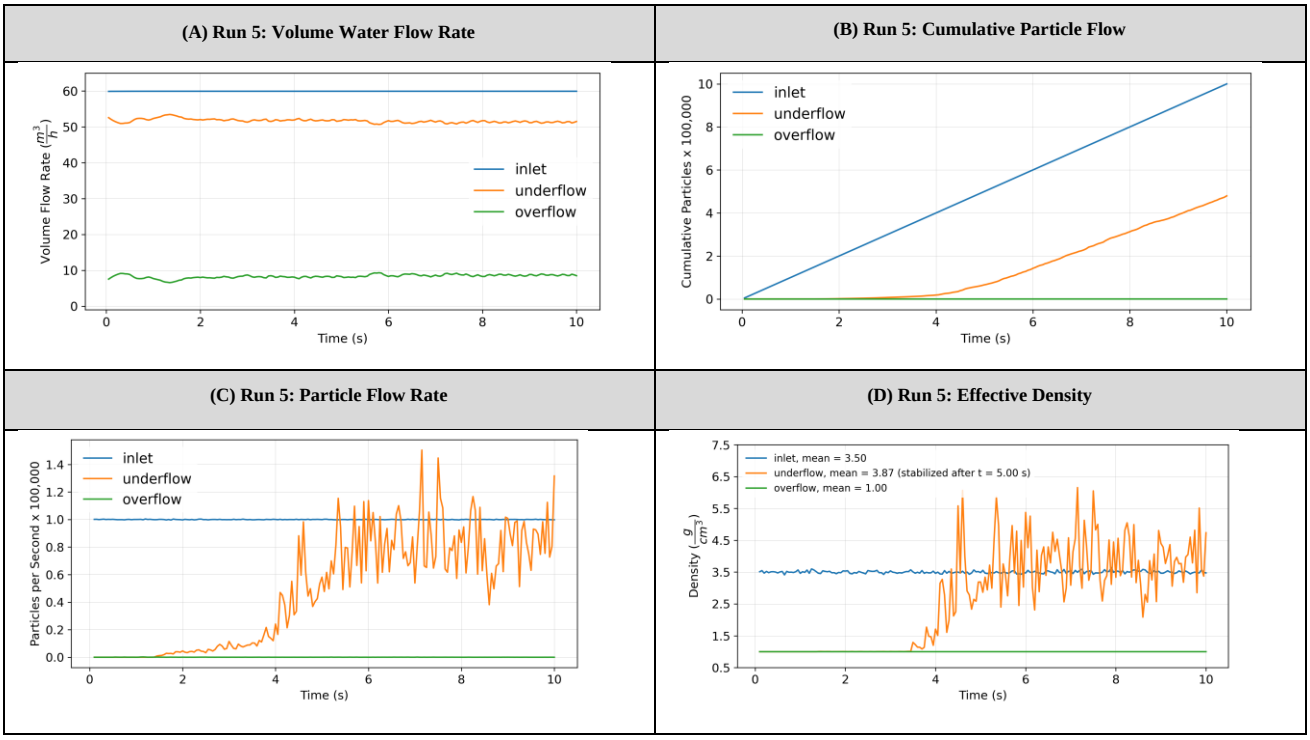


Figure 4.8: Model flow and density outputs of Run 5 in the DoE

The results in Figure 4.8 indicate that there is significant densification of the medium to 3.87 t/m^3 at the underflow using a 35-mm vortex finder at a feed density of 3.5 t/m^3. The densifier also exhibits a minimum particle flow rate through the overflow, which means it is successfully dewatering the medium. The shear stress on the densifier is illustrated in Figure 4.9.

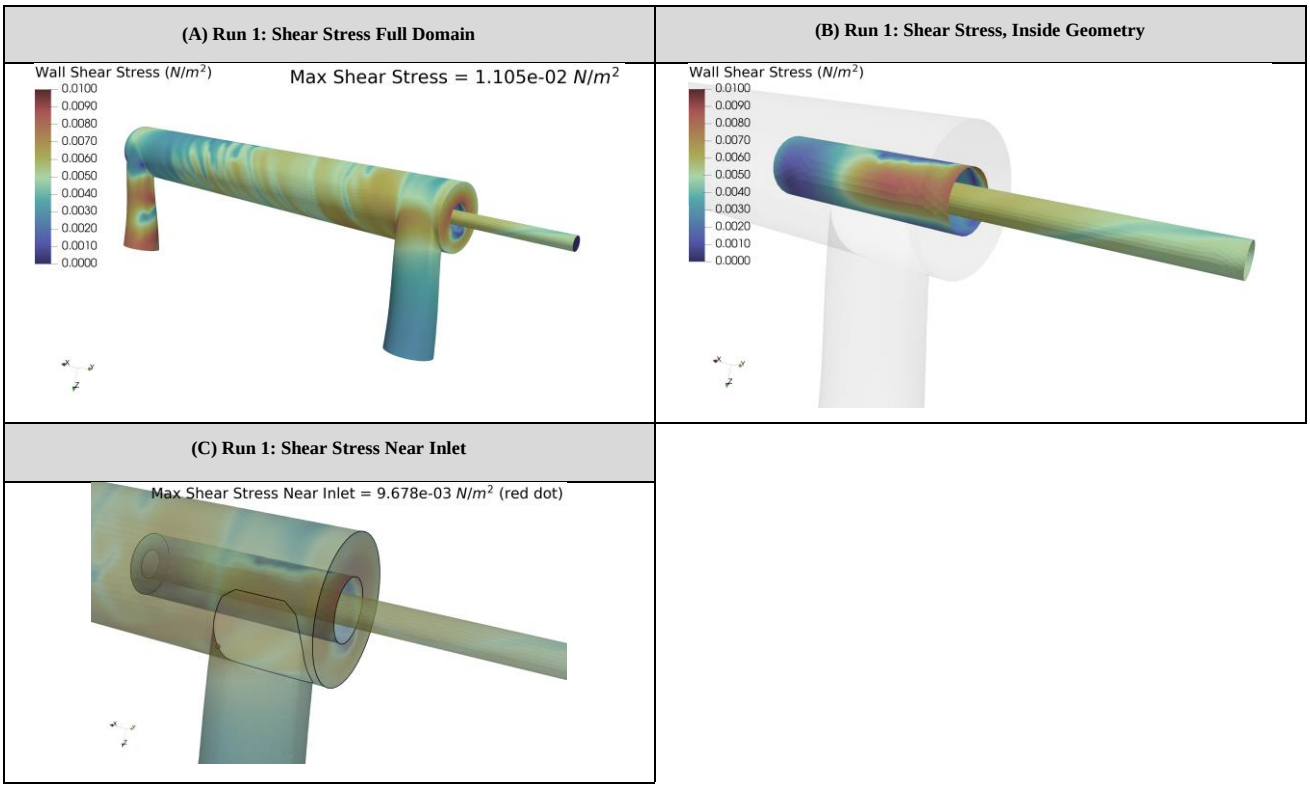


Figure 4.9: Shear stress outputs of Run 5 in the DoE

From the results it is observed that with increased density, more particles will escape to both the outlets, hence the high shear stress is experienced at the overflow. However, the maximum shear stress at the inlet is lower at 9.678e^{-3} N/m^2 as the vortex finder is opened. Therefore, when running under these conditions, the outlet is expected to wear first, but wear on the inlet and vortex finder base is also observed. This is due to somewhat higher wear at the inlet compared to the first run.

A summary of Run 4 to Run 6 is shown in Table 4.6 which entails all the runs completed at a 3.5 t/m^3 feed density with vortex finder diameters of 30 mm, 35 mm and 40 mm.

Table 4.6: Model outputs of Run 4 to Run 6 in the DoE table

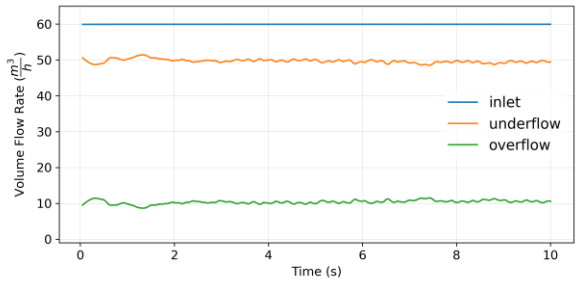
Operating flow rate 50 m^3/h		Density$_{U/F}$	Cum. particles $_{O/F}$	Cum. particles $_{U/F}$	Max shear stress $_{Inlet}$
Vortex diameter (mm)	30	3.70	173	446619	9.719e-03
	35	3.87	238	467742	9.678e-03
	40	4.03	374	479727	9.671e-03

It is evident that opening the vortex finder diameter improves densification on the unit at a feed density of 3.5 t/m^3; however, it does slightly lower the shear stress on the inlet.

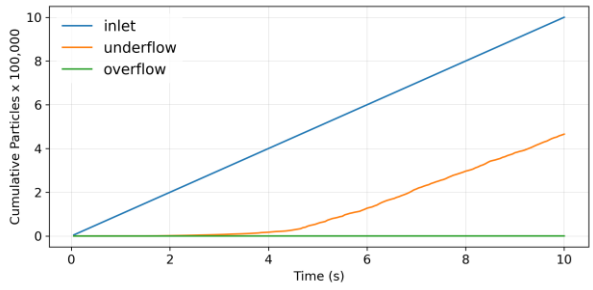
4.2.3. Run 9: 40-mm vortex finder and 3.6 t/m^3 feed SG

The volume flow rate of the water, cumulative particle flow, particle flow rate and effective density from the ninth run are presented in Figure 4.10.

(A) Run 9: Volume Water Flow Rate



(B) Run 9: Cumulative Particle Flow



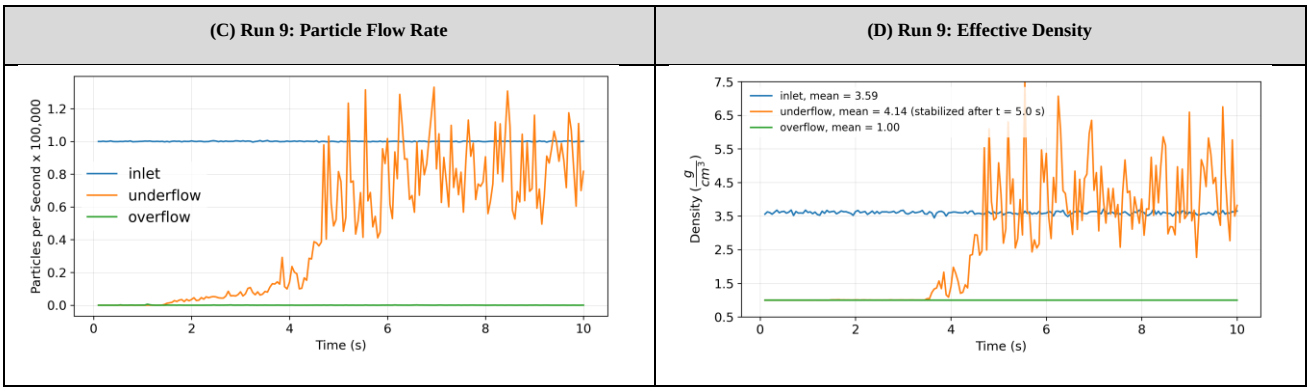


Figure 4.10: Model flow and density outputs of Run 9 in the DoE table

Figure 4.10 shows that there is significant densification of the medium to 4.14 t/m^3 at the underflow using a 40-mm vortex finder at a feed density of 3.6 t/m^3. The densifier also exhibits minimum particle flow rate through the overflow, which means it is successfully dewatering the medium. The shear stress on the densifier is illustrated in Figure 4.11.

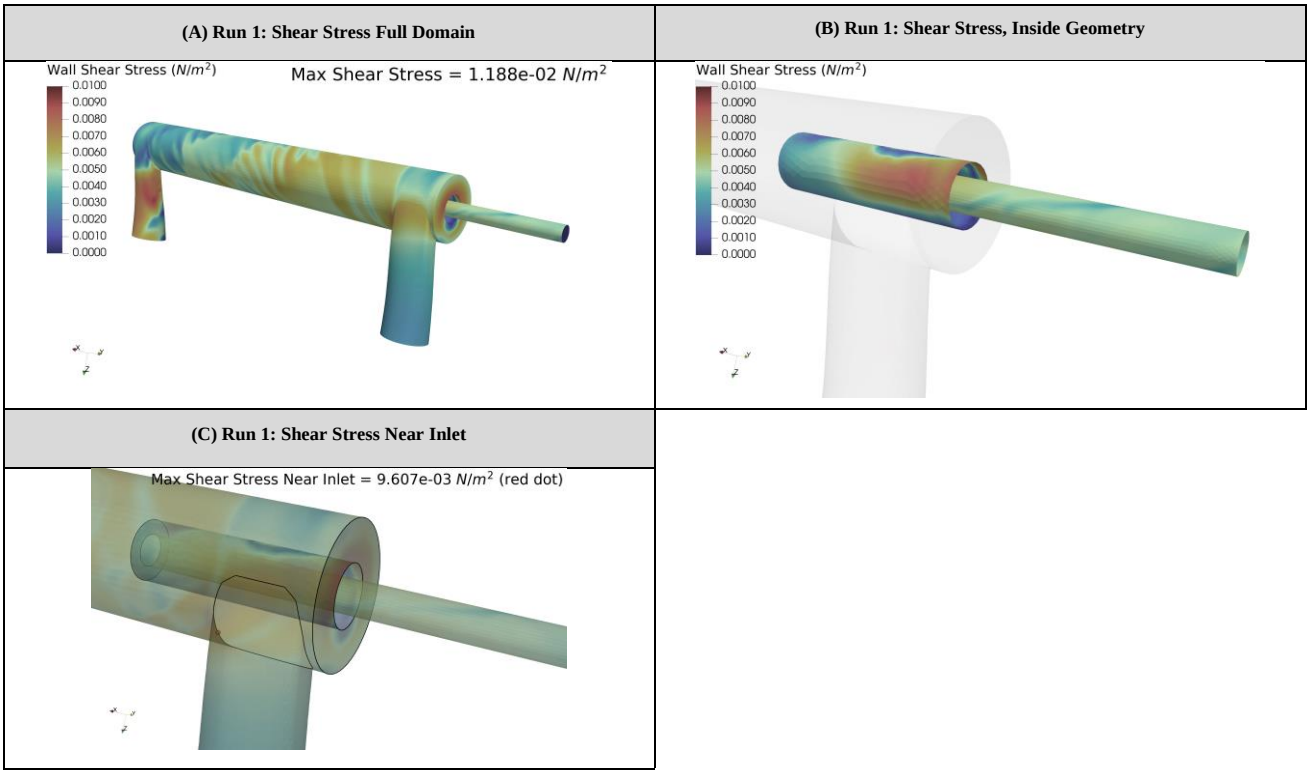


Figure 4.11: Shear stress on the densifier

A summary of Run 7 to Run 9 is given below in Table 4.7.

Table 4.7: Model outputs of Run 7 to Run 9 in the DoE table

Operating flow rate 50 m³/h		Density $_{U/F}$	Cum. particles $_{O/F}$	Cum. particles $_{U/F}$	Max shear stress $_{Inlet}$
Vortex diameter (mm)	30	3.64	7	464336	9.700e-03
	35	4.00	245	465785	9.662e-03
	40	4.14	386	482923	9.607e-03

It is evident that opening the vortex finder diameter improves densification on the unit at a feed density of 3.6 t/m^3; however, it does slightly lower the shear stress on the inlet.

4.2.4. Numerical model summary

The DoE outcomes for the modelling are summarized in Table 4.8 in terms of densifier underflow density, density differentials and shear stress at the inlet.

Table 4.8: DoE for the tube densifier by modelling

Operating flow rate 50 m³/h		**Wear and efficiency outputs**								
		$SG_{U/F}$	$SG_{U/F} - SG_{O/F}$	Shear Stress (N/m^2)	$SG_{U/F}$	$SG_{U/F} - SG_{O/F}$	Shear Stress (N/m^2)	$SG_{U/F}$	$SG_{U/F} - SG_{O/F}$	Shear Stress (N/m^2)
		Feed density = 3.4 t/m³			**Feed density = 3.5 t/m³**			**Feed density = 3.6 t/m³**		
Vortex diameter (mm)	30	3.40	2.40	9.656e-03	3.70	2.70	9.719e-03	3.64	2.64	9.700e-03
	35	3.74	2.74	9.706e-03	3.87	2.87	9.678e-03	4.00	3.00	9.662e-03
	40	3.89	2.89	9.770e-03	4.03	3.03	9.671e-03	4.14	3.14	9.607e-03

The modelling output shows that as the density and vortex finder diameter increase, the shear stress on the inlet is relieved. Also, from the results it is anticipated that a larger vortex finder diameter will increase the density differential, having a positive impact on the performance of the densifier. All overflow densities were measured at 1.00 t/m^3 which models the ideal behaviour of the densifier.

The shear stresses predicted in the numerical modelling are confirmed by wear patterns found in actual densifiers. Photographs of some failures at the inlet and vortex finders of the HMA and Multotec densifiers are presented in Figure 4.12, validating the observations of the modelling results.

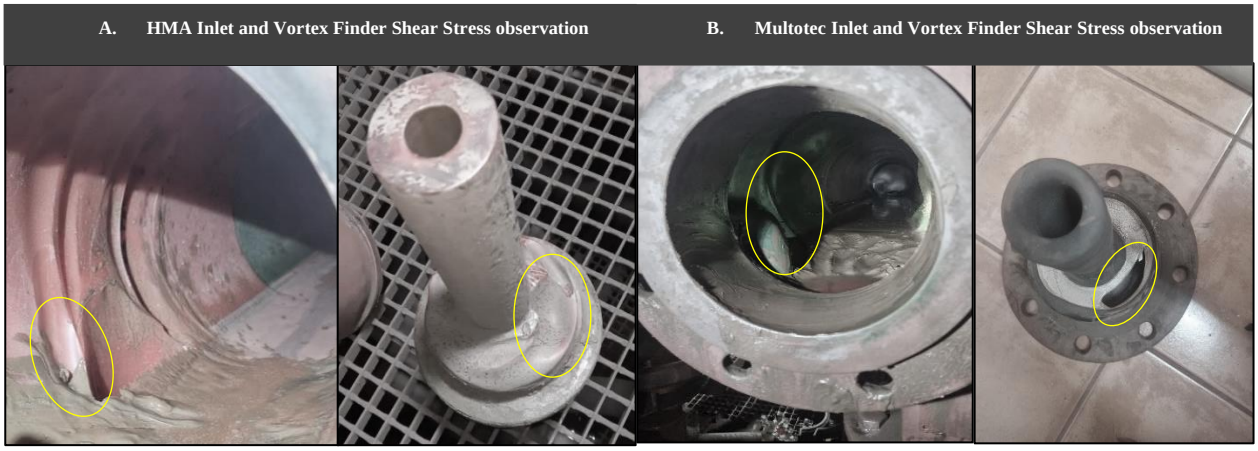


Figure 4.12: Practical observations of shear stress impact and end of part life

4.3. Discussion and comparison

From the numerical model (MPPIC integration) it can be concluded that high shear stresses are experienced at the inlet of the densifier, and this is confirmed by the practical findings of wear patterns on the worn parts. The shear stress is relieved by increasing the diameter of the vortex finder, allowing greater outflow at the overflow of the densifier.

The practical test work results proved that the only acceptable dewatering occurs at a smaller vortex finder for the current HMA 200NB unit with a vortex finder diameter of 32 mm and the Multotec PC200 densifier with a 30 mm vortex finder diameter. This is not in line with the results of the modelling as for all modelled scenarios the overflow density was recorded at 1.00 t/m^3, which was considered ideal behaviour. In practice, higher overflow densities were observed due to inefficiencies, which increased as the operating densities increased.

Both practical test work and modelled differential results exhibited better dewatering or separation efficiency with an increase in feed density.

5. CONCLUSION

The depletion of high-grade iron ore supply at Sishen Mine in the Northern Cape, South Africa, has required the beneficiation plants to operate at increased media densities to process the lower-grade ore. This research aimed to address a specific aspect of the problem, namely the optimisation of the densification process. It involved practical test work on two different designs of centrifugal densifiers, complemented by numerical modelling that integrated multiphase particle-in-cell (MPPIC) and computational fluid dynamics (CFD).

While the integration of MPPIC and CFD proved valuable, MPPIC came with limitations, particularly in terms of accurately representing lower-density feed. Nonetheless, the research methodology encompassed a thorough combination of computational modelling techniques and hands-on experimentation. These simulations and practical tests delved into the behaviour of the densification process under varying densities and vortex finder diameters, influencing flow control. Vortex finder diameters of 30 mm, 35 mm, and 40 mm were examined, alongside operational densities of 3.4 t/m^3, 3.5 t/m^3, and 3.6 t/m^3.

From the numerical modelling, optimal operational parameters were identified. Maintaining a feed density of 3.60 t/m^3 and a shear stress of 9.70 e-3 N/m^3 at the inlet – augmented by a 30-mm vortex finder diameter – yielded remarkable enhancements in media densification and downstream recovery. These enhancements carry substantial practical importance, evidenced by heightened predictability in wear rates and the consistent maintenance of media overflow below 1.20 t/m^3 to the recovery circuit. Additionally, insights were gained on establishing optimal operating conditions and control measures for the early detection of potential failures.

Subsequent real-world testing on the two densifiers – an existing unit manufactured by HMA and a test unit manufactured by Multotec – validated this finding. It also demonstrated the superior performance of the Multotec densifier configuration, particularly at higher densities and inlet pressures ranging between 430 kPa and 500 kPa.

The study's primary focus of enhancing wear resistance in the dense media separation plant operating at higher densities was realized and significant advances were achieved. Notable amongst these was the extension of the mean time to failure from three weeks to three months. This advancement improved maintenance strategies, as proactive planning now involves timely and safer interventions. As a result, the frequency of operational interruptions has been substantially reduced, culminating in a marked decrease in unplanned downtimes and consequential losses of FeSi. This culmination contributes to the broader discourse on efficient low-grade iron ore processing and demonstrates the significance of tailored equipment optimization in mining operations.

5.1. Recommendations

This report proposes the implementation of the Multotec PC200 densifier at the Sishen Mine drum plant, contingent upon the addition of control water into downstream recovery processes. Additionally, it suggests that HMA consider changing from a clamped design to a bolted design to enhance the densifier's safety factor. Moreover, the utilization of a more wear-resistant material is recommended for the high-wear regions on the inlet and the vortex finder base of the HMA unit.

The numerical modelling highlighted a need for further research using the CFD-DEM approach. This methodology holds the potential for capturing granular interactions very effectively,

offering a more comprehensive understanding of the densification process. Endeavours should be directed towards devising techniques that alleviate the computational demands, making it feasible without the exclusive reliance on high-performance supercomputers. This step would contribute to the democratization of numerical analysis in this domain and enable broader exploration and innovation.

6. REFERENCES

Gao, X., Li, T., Sarkar, A., Lu, L., & Rogers, W. (2018). Development and validation of an enhanced filtered drag model for simulating gas-solid fluidization of Geldart A particles in all flow regimes. *Chemical Engineering Science*, 184, 33-51.

Agrawal, M., Khanna, S., Kopliku, A., & Lockett, T. (2019). Prediction of sand erosion in CFD with dynamically deforming pipe geometry and implementing proper treatment of turbulence dispersion in particle tracking . In *Wear* (pp. 596–604).

Anderson, T. B., & Jackson, R. (1967). Fluid Mechanical Description of Fluidized Beds: Equations of Motion. In *Ind. Eng. Chem. Fundamentasl* (pp. 527-539).

Andrews, J. P. (1930). Theory of collision of spheres of soft metals. *The London, Edinburgh, and Dublin Philosophical Magazine and Journal of Science*, 593–610.

Andrews, M. J., & O'Rourke, P. J. (1996). The multiphase particle-in-cell (MP-PIC) method for dense particulate flows. *Int. J. Multiphase Flow* , 379-402.

Arabnejad, H., Mansouri, S., Shirazi, A., & McLaury, B. S. (2015). Development of mechanistic erosion equation for solid particles. In *Wear* (pp. 1044–1050).

Baboo, P. (2006). *The Analysis & Prevention of Safety Hazards in NFL Complex.* India: National Fertilizers ltd.

Bahadur, S., & Badruddin, R. (1990). Erodent particle characterization and the effect of particle size and shape on erosion. In *Wear* (pp. 189–208).

Beetstra, R., van der Hoef, M. A., & Kuipers, J. A. (2007). Drag force of intermediate Reynolds number flow past mono- and bidisperse arrays of spheres. *AIChE Journal* , 489-501.

Bekker, E. (2014). DMC Basics – A Holistic View, . *11th DMS Powders Conference.* Mount Grace.

Bitter, G. A. (1963). A study of erosion phenomena part i. In *Wear* (pp. 5–21).

Bosman, J. (2005). Densification in Dense Media Circuits. *9th Technical Dense Medium Symposium.* University of Pretoria: Department of Material Science.

Bosman, J. (2006). The selection and application of densifiers in dense medium circuits. University of Pretoria: Department of Material Science.

Bosman, J. (2011). Deciphering the densifier. University of Pretoria: Department of Material Science.

Chapman, S. (2014). The mathematical theory of non-uniform gases : an account of the model andcfd-dem method for modeling impinging gas–solidflows. *Powder Technology,* 94–102.

Chen, D., Sarumi, M., & Al-Hassani, S. (1998). Computational mean particle erosion model. In *Wear* (pp. 64-73).

Chen, X., & Wang, J. (2014). A comparison of two-fluid model, dense discrete particle model andcfd-dem method for modeling impinging gas–solidflows. *Powder Technology,*, 94–102.

Chen, X., McLaury, S., & Shirazi, S. A. (2004). Application and experimental validation of a computational fluid dynamics (CFD)-based erosion prediction model in elbows and plugged tees. *Computers and Fluids*, 1251–1272.

Chiu, A. C. (2012). *The Evolution of the Weep-Hole.* Columbia University.

Chu, K. W., Wang, B., Yu, A. B., & Vince, A. (2012). Particle scale modelling of the multiphase flow in a dense medium cyclone: Effect of vortex finder outlet pressure. *Minerals Engineering*, 46 - 58.

Chu, K. W., Wang, B., Yu, A. B., Vince, A., Barnett, G. D., & Barnett, P. J. (2009). CFD–DEM study of the effect of particle density distribution on the multiphase flow and performance of dense medium cyclone. *Minerals Engineering*, 893 - 909.

Chu, K., Chen, J., & Yu, A. (2016). Applicability of a coarse-grained CFD–DEM model on dense medium cyclone. *Mineral Engineering*, 43-54.

Chu, K., Wang, B., Yu, A., & Vince, A. (2012). Computational study of the multiphase flow in a dense medium cyclone: Effect of particle density. *Chemical Engineering Science*, 123–139.

Chu, K., Wang, B., Yu, A., Vince, A., Barnett, G., & Barnett, P. (2009). CFD–DEM study of the effect of particle density distribution on the multiphase flow and performance of dense medium cyclone. In *Minerals Engineering* (pp. 893-909).

Cleary, P. (1998). Predicting charge motion, power draw, segregation and wear in ball mills using discrete element methods. In *Minerals Engineering* (pp. 1061-1080).

Cloete, S., Johansen, T., & Amini, S. (2012). Performance evaluation of a complete lagrangian KTGF approach for dilute granular flow modelling. *Powder Technology*, 43–52.

Collins, B., Napier-Munn, T. J., & Sciarone, M. (1974). The production,properties and selection of ferrosilicon powders for heavy-medium separation. *Journal of the Southern African Institute of Mining and Metallurgy*, ferrosilicon powders for heavy-medium.

Crowe, C. T. (2005). *Multiphase Flow Handbook: Mechanical and Aerospace Engineering Series.* CRC Press.

Cundall, P. A., & Strack, O. (1979). A Discrete Numerical Mode For Granular Assemblies. In *Geotechnique* (pp. 47-65).

Daris, K. A. (1987). The Design and Operation of Heavy Medium Recovery Circuits for Improved Medium Recovery. *Coal Preparation*, 119 - 157.

Ding, J., & Gidaspow, D. (1990). A bubbling fluidization model using kinetic theory of granular flow. *AIChE Journal*, 523–538.

Elghobashi, S. (1994). Predicting particle-laden turbulent flows. *Applied Scientific Research*, 309–329.

Ergun, S. (1952). Fluid flow through packed columns. In *Chem. Eng.Prog.* (pp. 89 - 94).

Ferrara, G., Bevilacqua, P., de Lorenzi, L., & Zanin, M. (2000). The influence of particle shape on the dynamic dense medium separation of plastics. *International Journal of Mineral Processing*, 225-235.

Ferrara, G., Lapasin, R., & Bevilacqua, P. (1992). Modelling the rheological behaviour of dense media and design of medium circuits in dynamic DMS processes. In *Minerals Engineering* (pp. 1123-1134). Elsevier.

Finnie, I. (1960). Erosion of surfaces by solid particles. In *Wear* (pp. 87–103).

Finnie, I., & McFadden, D. H. (1978). On the velocity dependence of the erosion of ductile metals by solid particles at low angles of incidence. In *Wear* (pp. 181–190).

Flanagan, M. (2000). Simplified Dilute Medium Circuit and Improved Medium Recovery With the Permax Separator. *Seventh Samancor Dense on Dense Medium Separation.* Zimbali.

Forder, A., Thew, M., & Harrison, D. (1997). A numerical investigation of solid particle erosion experienced within oilfield control valves. In *Wear* (pp. 184–193).

Galvin, K., & Smitham, J. B. (1994). Use of X-rays to determine the distribution of particles in an operating cyclone. In *Minerals Engineering* (pp. 1269-1280).

Garg, R., Galvin, J., Li, T., & Pannala, S. (2012). Open-source MFIX-DEM software for gas–solids flows: Part I—Verification studies. *Powder Technologies*, 122-137, 138-150.

Gidaspow, D. (1994). Multiphase flow and fluidization: continuum and kinetic theory descriptions. *Academic press*.
Gidaspow, D. (1994). *Multiphase flow and fluidization: continuum and kinetic theory descriptions.* Boston: Academic Press.
Gochin, R. J., & Smith, M. R. (1983). Dense Medium Separation. Part 1: An introduction to thetheory and practice . *Mining Magazine*, 453-460.
Grant, G., & Tabakof, W. (1975). Erosion prediction in turbomachinery resulting from environmental solid particles. *Journal of Aircraft*, 471–547.
Guenther, C., & Syamlal, M. (2001). The effect of numerical diffusion on simulation of isolated bubbles in a gas–solid fluidized bed. *Powder Technology*, 116, 142-154.
H, C. V. (1975). The use of heavy-medium separationin the processing of iron ores. *Journal of the Southern African Institute of Mining and Metallurgy*, 303 - 306.
Halvorsen, B. M., Plessis, J. P., & Woudberg, S. (2006). *The performance of drag models on flow behaviour in the CFD simulation of a fluidized bed.* University of Stellenbosch, South Africa.
Harris, S. E., & Crighton, D. G. (1994). Solitons, solitary waves, and voidage disturbances in gas-fluidized beds. *Journal of Fluid Mechanics* , 243 - 276.
He, Y. B., & Laskowski, J. (1994). Effect of dense medium properties on the separation performance of a dense medium cyclone. In *Minerals Engineering* (pp. 209-221).
Helland, E., Occelli, R., & Tadrist, L. (2002). Computational study of fluctuating motions and cluster structures in gas–particle flows. *International Journal of Multiphase Flow*, 199-223.
Hoomans, B. P., Kuipers, J. A., Briels, W. J., & van Swaaij, W. P. (1996). Discrete particle simulation of bubble and slug formation in a two-dimensional gas-fluidised bed: A hard-sphere approach. *Chemical Engineering Science*, 51, 99-118.
Jayasundara, C., Yang, R., Yu, A., & Curry, D. (2011). Prediction of the disc wear in a model IsaMill and its effect on the flow of grinding media. In *Minerals Engineering* (pp. 1586-1594).
Jenkins, J. T. (1992). Boundary Conditions for Rapid Granular Flow: Flat, Frictional Walls. *Journal of Applied Mechanics*, 120.
Jianren, F., Dadong, Z., Keli, Z., & Kefa, C. (1992). Numerical and Experimental Study of Finned Tube Erosion Protection Methods. In *Wear* (pp. 1-19).
Kennedy, D., & Norman, C. (2005). What don't we know? *Science*, 75-75.
Legault-Seguin, E., Mohns, C., & Rylatt, M. (2016). *Dense Medium Separation - An effective and robust Preconcentration Technology.* Lakefield: SGS Canada Inc.
Lester, D., Graham, L., & Wu, J. (2010). High precision suspension erosion modeling. In *Wear* (pp. 449-457).
Li, F., Song, F. F., Benyahia, S., Wang, W., & Li, J. H. (2012). MP-PIC simulation of CFB riser with EMMS based drag model. *Chemical Engineering Science*, 104-113.
Li, T., Peng, Y., Zhu, Z., Zou, S., & Yin, Z. (2017). Discrete Element Method Simulations of the Inter-Particle Contact Parameters for the Mono-Sized Iron Ore Particles. *Minerals*, 520.
Liebhard , M., & Levy, A. (1991). The effect of erodent particle characteristics on the erosion of metals. In *Wear* (pp. 381–390).
Loth, E. (2000). Numerical approaches for motion of dispersed particles, droplets and bubbles. *Progress in Energy and Combustion Science*, 161–223.

Lu, L., Gopalan, G., & Benyahia, S. (2018). *Assessment of different discrete particle methods ability to predict gas-particle flow in a small-scale fluidized bed.* West Virginia: West Virginia University Research Corporation, .

Lu, L., Konan, A., & Benyahia, S. (n.d.). Influence of grid resolution, parcel size and drag models on bubbling fluidized bed simulation. *Chemical Engineering Journal*.

Lu, L., Li, T., & Benyahia, S. (2017). An efficient and reliable predictive method for fluidized bed simulation. *AIChE Journal (2nd review)*.

Lu, L., Xu, J., Ge, W., Yue, Y., Liu, X., & Li, J. (2014). EMMS-based discrete particle method (EMMS–DPM) for simulation of gas–solid flows. *Chemical Engineering Science*, 67-87.

Lu, L., Yoo, K., & Benyahia, S. (2016). Coarse-Grained-Particle Method for Simulation of Liquid–Solids Reacting Flows. *nd. Eng. Chem. Res.* , 10477-10491.

Lun, C. K., Savage, S. B., Jeffrey, D. J., & Chepurniy, N. (1984). Kinetic theories for granular flow: inelastic particle in couette flow and slightly inelastic particle in a general flow field. *Journal of Fluid Mechanics*, 223–256.

Magwai, M. K., & Bosman, J. (2008). The effect of cyclone geometry and operating conditions on spigot capacity of dense medium cyclones. *International Journal of Mineral Processing*, 94 - 103.

Magwai, M., & Bosman, J. (2008). The effect of cyclone geometry and operating conditions on spigot capacity of dense medium cyclones. *International Journal of Mineral Processing*, 94-103.

Medina, H. J., Beechook, A., Saul, J., Porter, S., Aleksandrova, S., & Benjamin, S. (2016). *Open source Computational Fluid Dynamics using OpenFOAM.* Coventry, England: Coventry University.

Meng, H. C., & Ludema, K. C. (1995). Wear models and predictive equations: their form and content. In *Wear* (pp. 443–457).

Mukherjee, A. K., Sripriya, R., Rao, P. V., & Das, P. (2003). Effect of increase in feed inlet pressure on feed rate of dense media cyclone. *International Journal of Mineral Processing: Volume 69*, 259-274.

Mulder, M. S. (1985). Practical methods developed by Iscor to curtail ferrosilicon losses, with special reference to the methods applied at the Sishen Iron–Ore Mine. *2nd Samancor Symposium on DMS.* Perth.

Myburgh, H. A. (2013). Influence of quality of ferrosilicon on rheology of dense medium and ability to reach higher densities. *Mineral Processing and Extractive Metallurgy*, 39 - 43.

Napier-Munn, T. (2018). The dense medium cyclone – past, present and future. In *Minerals Engineering* (pp. 107-113). Elsevier.

Napier-Munn, T. J., Kojovic, T., Scott, I. A., Masinja, J. H., Shi, F., & Banguley, P. J. (1995). Some causes of medium loss in dense medium plants. In *Minerals Engineering* (pp. 659 - 678). Elsevier. Retrieved from Multotec: https://www.multotec.com/en/cyclones

O'Rourke, P. J., & Snider, D. M. (2012). "Inclusion of collisional return-to-isotropy in the MP-PIC method. *Chemical engineering science*, 39 - 54.

Oka, Y. I., & Yoshida, T. (2005). Practical estimation of erosion damage caused by solid particle impact: Part 2: Mechanical properties of materials directly associated with erosion damage. In *Wear* (pp. 102–109).

Oka, Y. I., Okamura, K., & Yoshida, T. (2005). Practical estimation of erosion damage caused by solid particle impact: Part 1: Effects of impact parameters on a predictive equation. In *Wear* (pp. 95–101).

Osborne, D. G. (1988). Coal Preparation Technology Volume 1. Graham & Trotman Ltd.
Ouyang, J., & Li, J. (1999). Particle-motion-resolved discrete model for simulating gas-solid fluidization. *Chemical Engineering Science*, 2077–2083.
Ozel, A., Kolehmainen, J., Radl, S., & Sundaresan, S. (2016). Fluid and particle coarsening of drag force for discrete-parcel approach. *Chemical Engineering Science*, 258-267.
Parsi, M. (2015). *Sand Particle Erosion in Vertical Slug/churn flow*. Tulsa: PhD thesis, University of Tulsa.
Popplewell, G. M., & Burks, F. B. (1988). A Review of Dense Medium Plant Design in the Diamond Mining Industry. *Samancor Symposium on Dense Medium Separation.* Vereeniging.
Pryor, E. J. (1965). Chapter 12: Dense Media Separation. In *Minerals Processing* (p. 264). Elsevier Publishing Company Limited.
Radl, S., & Sundaresan, S. (2014). , A drag model for filtered Euler–Lagrange simulations of clustered gas particle suspensions. *Chemical Engineering Science*, 416-425.
Rajendran, S., Banerjee, P. K., Baijal, A., Dutta, A., Rao, M., & Chatterjee, S. (2007). Dense-Medium Cyclone: Plant Experience with High Near-Gravity Material Indian Coals. In *Coal Preparation* (pp. 78-106).
Rayner, J. G. (2002). A mathematical model of recovery of dense medium magnetics in the wet drum magnetic separator. *International Jurnal of Minerals Processing*, 57 – 173.
Restarick, C. J., & Krnic, Z. (1991). The effect of underflow/overflow ratio on dense medium cyclone operation. In *Minerals Engineering* (pp. 263-270).
Russell-Rhinehart, R. (2016). *Nonlinear Regression Modeling for Engineering Applications: Modeling, Model Validation and Enabling Design of Experiments.* ASME Press.
Sakai, M., & Koshizuka, S. (2009). Large-scale discrete element modeling in pneumatic conveying. *Chemical Engineering Science*, 533-539.
Sakano, M., Yaso, T., & Nakanishi, H. (2000). Numerical Simulation of Two-dimensional Fluidized Bed Using Discrete Element Method with Imaginary Sphere Model. *Japanese Journal of Multiphase Flow*, 66-73.
Schiller, L., & Naumann, A. (1935). Drag-coefficient model. In *Über die grundlegenden Berechnungen bei der Schwerkraftaufbereitung* (pp. 318 – 325). Z. Ver. Dtsch. Ing.
Scott, I. A., & Napier-Munn, T. (1992). Dense-medium cyclone model based on the pivot phenomenon. In *Section C: Min. Proc. Extr. Metall.* (p. 101). Trans. Inst. Min. Metall. .
Sharma, A. (2022). *Introduction to Computational Fluid Dynamics: Development, Application and Analysis.* Bangladesh: ANE Books Pvr. Ltd.
Sommerfeld, M. (2017). Numerical Methods for Dispersed Multiphase Flows. Cham: Springer International Publishing.
Song, C., B, P., Jiang, M., Wang, B., Xu, D., & Chen, Y. (2016). Numerical analysis of forces exerted on particles in cyclone separators. In *Powder Technology* (pp. 437 - 448). Elsevier.
Tom, P. (2015). *Optimization of Dense Medium Cyclone Plant for the Beneficiation of Low Grade Iron Ore with Associated High Proportion of Near-Density Material at Sishen Iron Ore Mine*. Johannesburg, South Africa: e Faculty of Engineering and the Built Environment, University of the Witwatersrand.
Tsuji, Y., Kawaguchi, T., & Tanaka, T. (1993). Discrete particle simulation of two-dimensional fluidized bed. *Powder Technolology*, 77, 79-87.

Tu, J., Yeoh, G. H., & Liu, C. (2018). *Computational Fluid Dynamics: A Practical Approach.* Oxford: Elsevier.

Voges, H. C. (1982). Heavy-medium and gravity separation at Iscor's tin-ore and iron-ore mines. *Journal of the Southern African Institute of Mining and Metallurgy*, 186 - 192.

Waanders, F. B., & A, M. (2003). Characterisation of Ferrosilicon Dense Medium Separation Material. *Hyperfine Interactions*, 325 – 329.

Weldhagen, T. (2015). *Magnetic Separator Efficiency SOP*. Germiston, Soth Africa: Malvern Engineering.

Wood, C., Davis, J., & Lyman, G. (1989). Towards a Medium Behaviour Based Performance Model for Coal-Washing Dense Medium Cyclones. In *Coal Preparation* (pp. 183-197).

Zhang, Y., Reuterfors, E. P., McLaury, B. S., Shirazi, S. A., & Rybicki, E. F. (2007). Comparison of computed and measured particle velocities and erosion in water and air flows. In *Wear* (pp. 330–338).

Zhou, L., Zhang, L., Bai, L., Shi, W., Li, W., Wang, C., & Agarwal, R. (2017). *Experimental study and transient CFD/DEM simulation in a fluidized bed based on different drag models.* RSC advances.

Zughbi, H., Phil, W. J., & Hutton, W. (1991). Numerical and experimental investigations of wear in heavy medium cyclones. In *Minerals Engineering* (pp. 245-262).

APPENDIX A: DENSIFIER PUMP CURVE

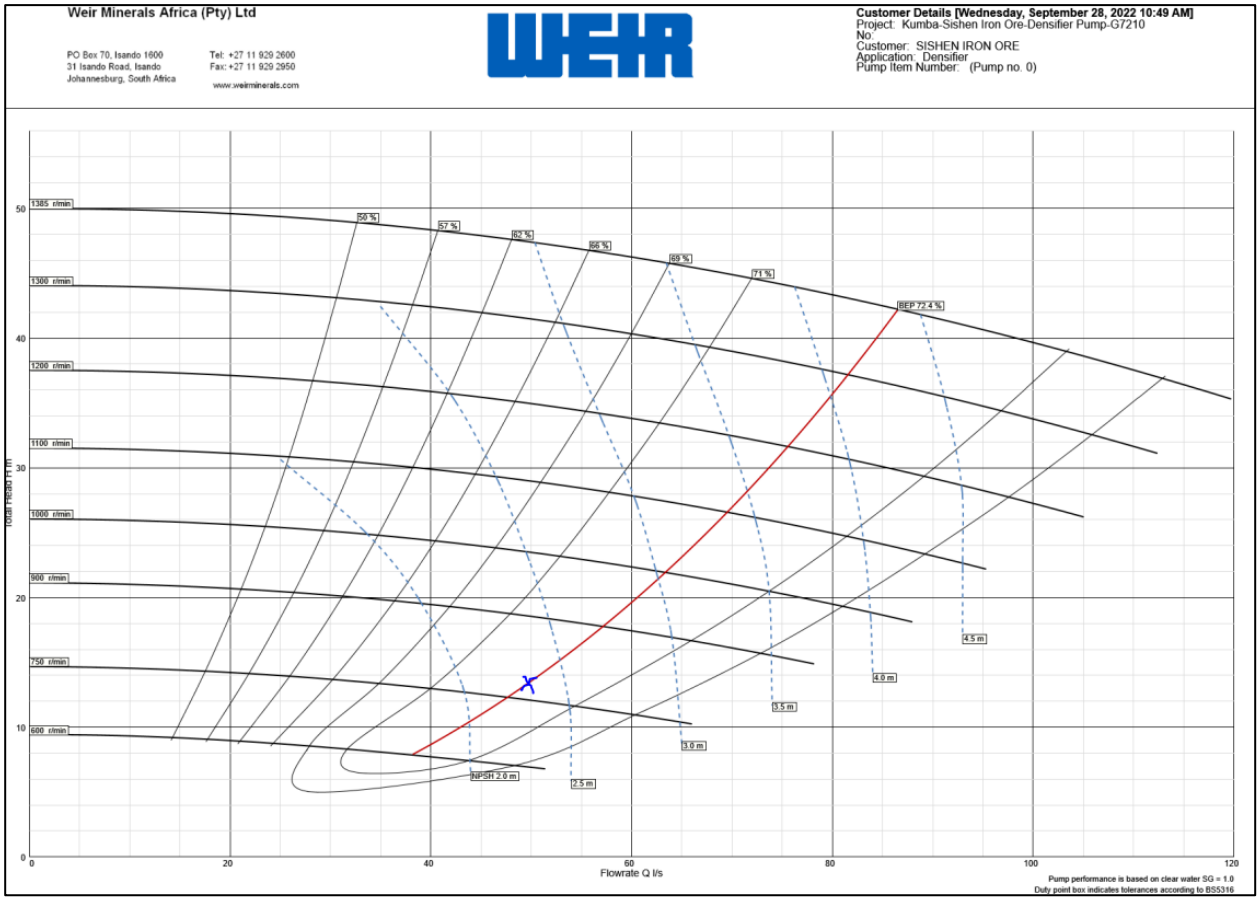


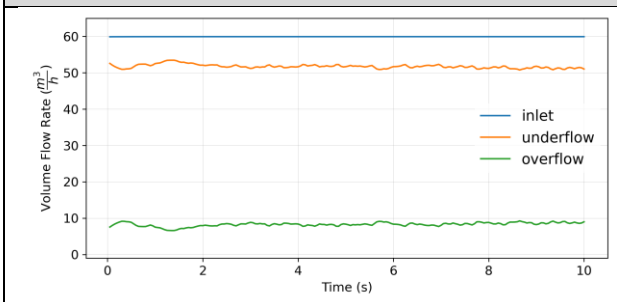
Figure A1: Tromp curve for the densifier feed pumps

Figure A1 illustrated the densifier pump curve demonstrating the in blue the expected flow of 50 l/s to the inlet of the densifier. This correlates with the pressure to the unit ranging between 430 kPa – 500kPa.

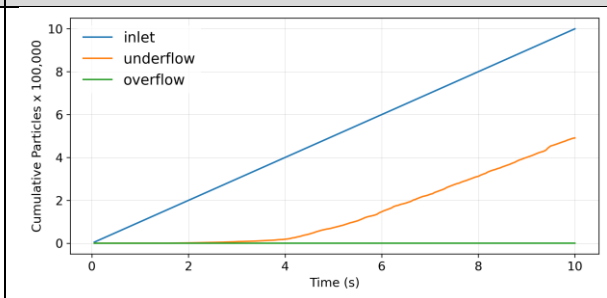
APPENDIX B: NUMERICAL MODEL ITERATION

Run 2: vortex finder diameter of 35 mm and feed Sg of 3.4 t/m3

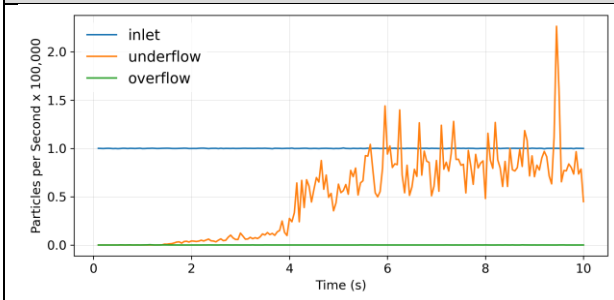
(A) Run 2: Volume Water Flow Rate



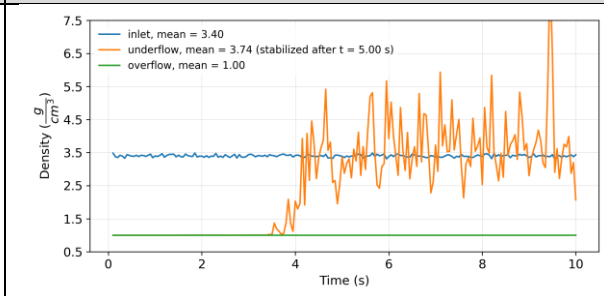
(B) Run 2: Cumulative Particle Flow



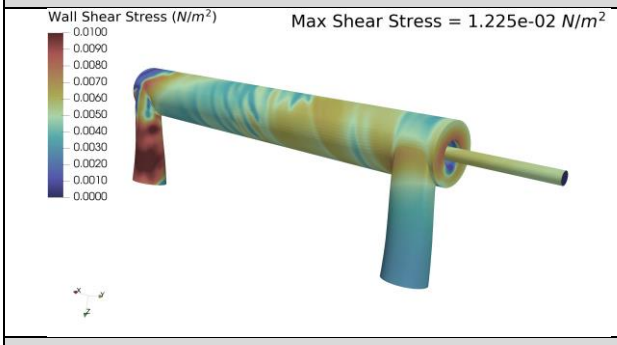
(C) Run 2: Particle Flow Rate



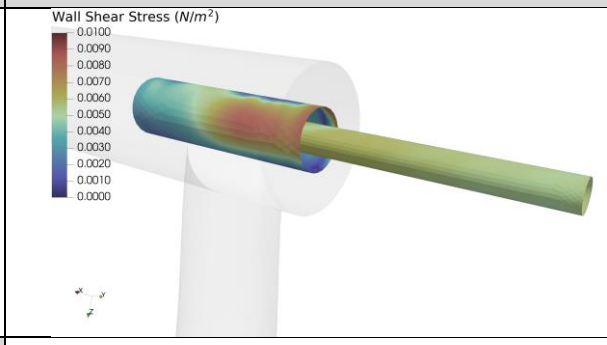
(D) Run 2: Effective Density



(E) Run 2: Shear Stress Full Domain



(F) Run 2: Shear Stress, Inside Geometry



(G) Run 2: Shear Stress Near Inlet

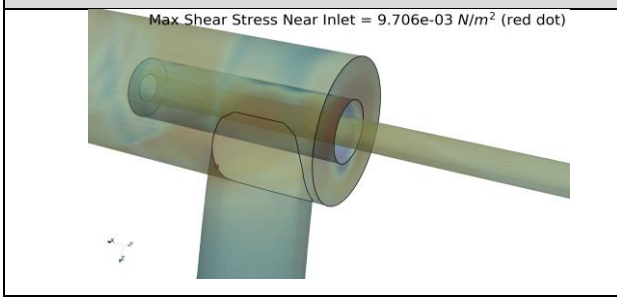
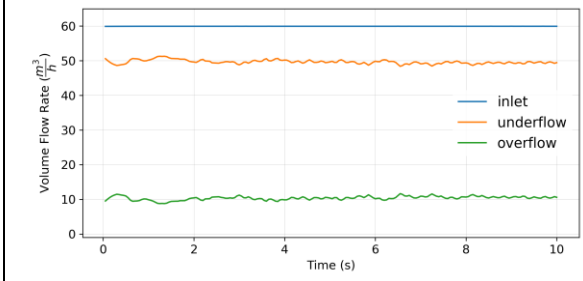


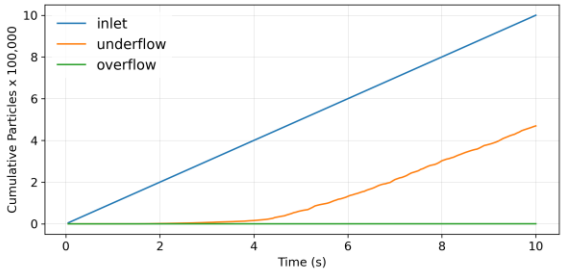
Figure B1: Volumetric flow, density and shear stress outputs of Run 2 in the DoE

Run 3: vortex finder diameter of 40 mm and feed SG of 3.4 t/m³

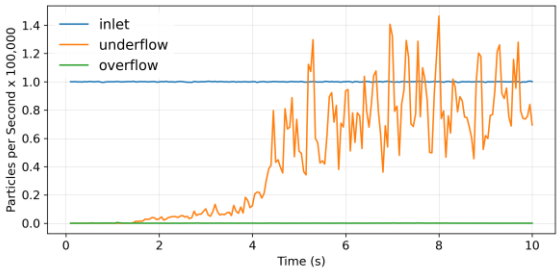
(A) Run 3: Volume Water Flow Rate



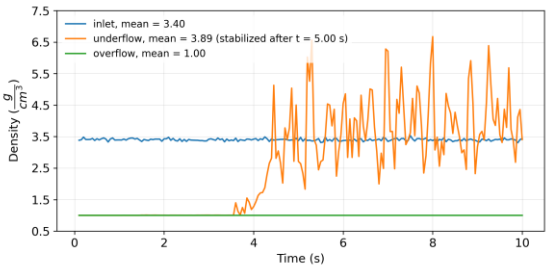
(B) Run 3: Cumulative Particle Flow



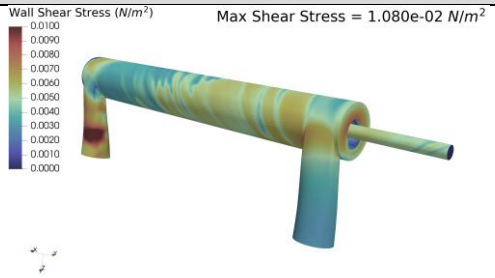
(C) Run 3: Particle Flow Rate



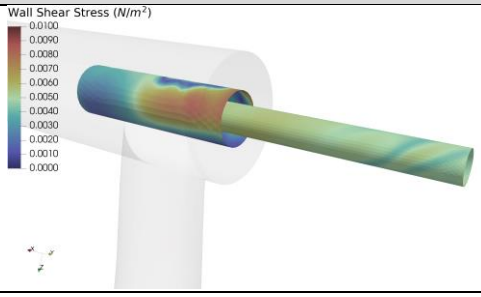
(D) Run 3: Effective Density



(E) Run 3: Shear Stress Full Domain



(F) Run 3: Shear Stress, Inside Geometry



(G) Run 3: Shear Stress Near Inlet

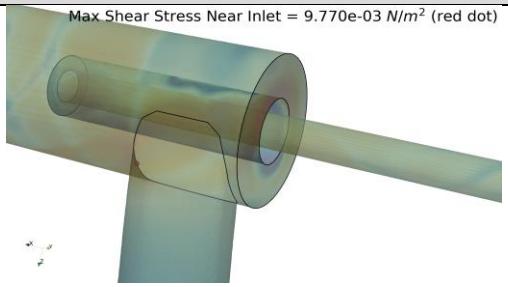
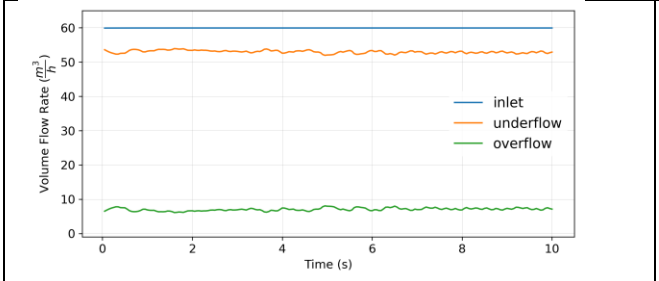


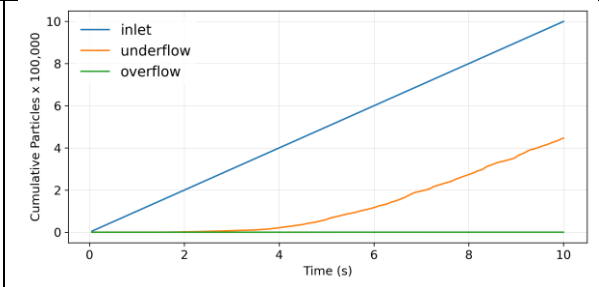
Figure B2: Volumetric flow, density and shear stress outputs of Run 3 in the DoE

Run 4: vortex finder diameter of 30 mm and feed SG of 3.5 t/m³

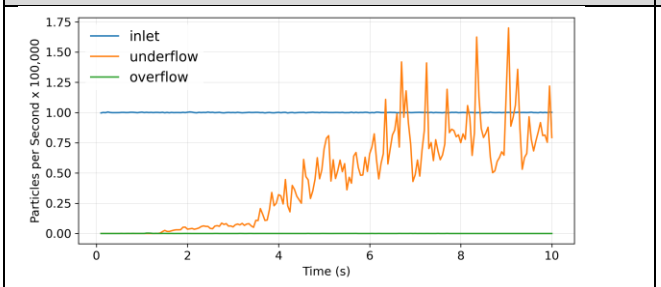
(A) Run 4: Volume Water Flow Rate



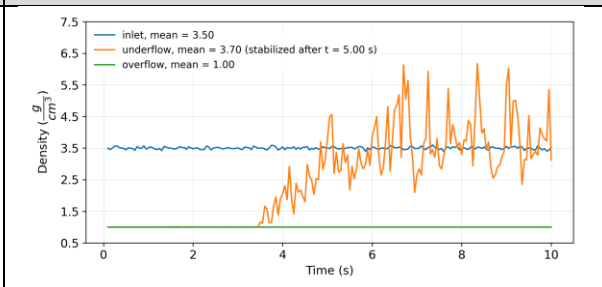
(B) Run 4: Cumulative Particle Flow



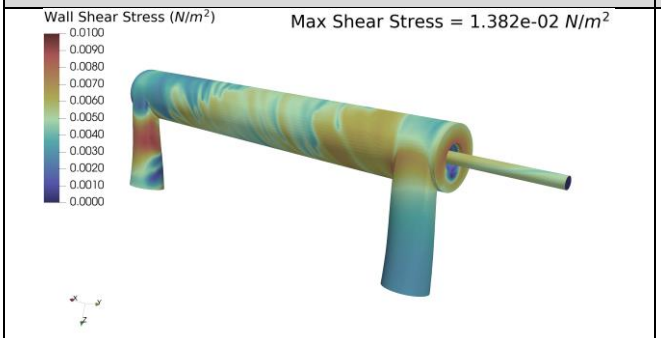
(C) Run 4: Particle Flow Rate



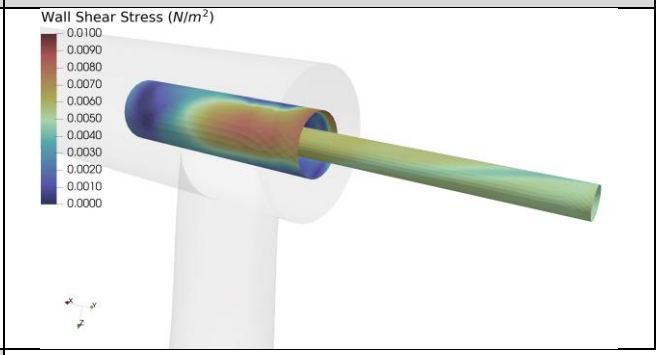
(D) Run 4: Effective Density



(E) Run 4: Shear Stress Full Domain



(F) Run 4: Shear Stress, Inside Geometry



(G) Run 4: Shear Stress Near Inlet

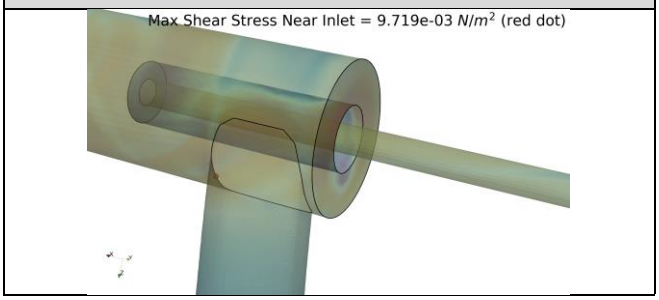
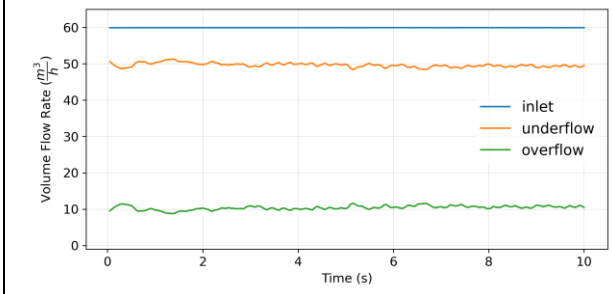


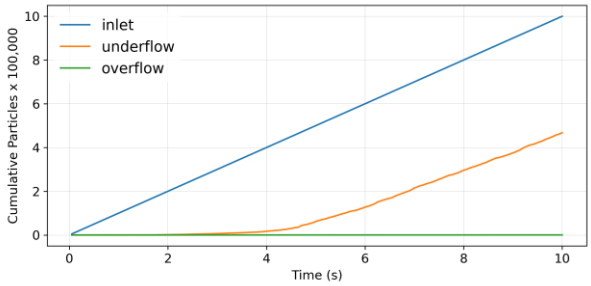
Figure B3: Volumetric flow, density and shear stress outputs of Run 4 in the DoE

Run 6: vortex finder diameter of 40 mm and feed SG of 3.5 t/m³

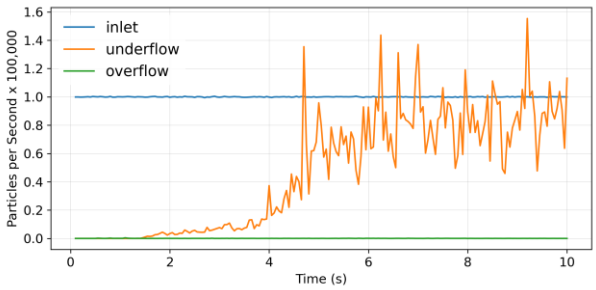
(A) Run 6: Volume Water Flow Rate



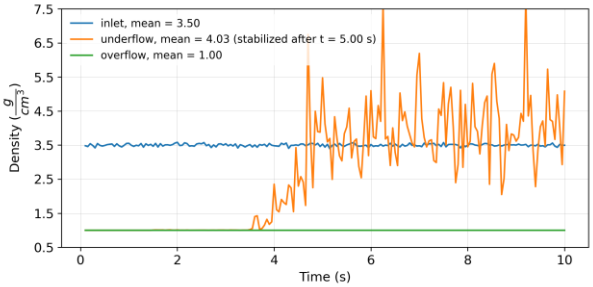
(B) Run 6: Cumulative Particle Flow



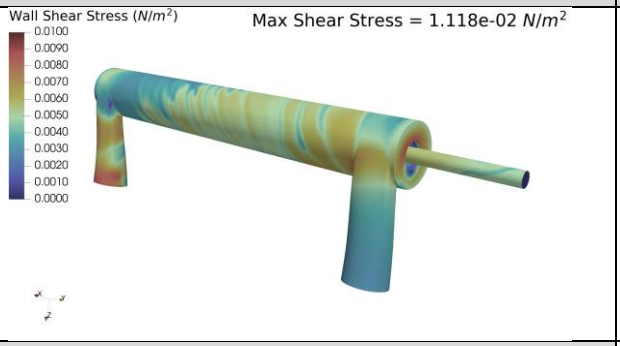
(C) Run 6: Particle Flow Rate



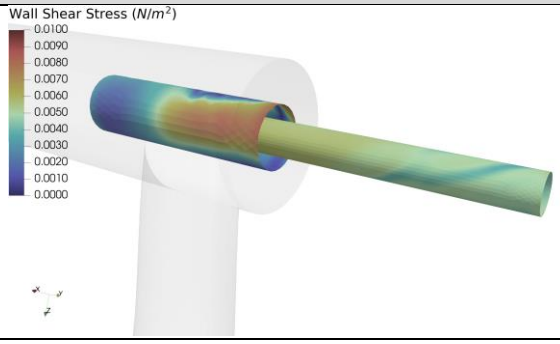
(D) Run 6: Effective Density



(E) Run 6: Shear Stress Full Domain



(F) Run 6: Shear Stress, Inside Geometry



(G) Run 6: Shear Stress Near Inlet

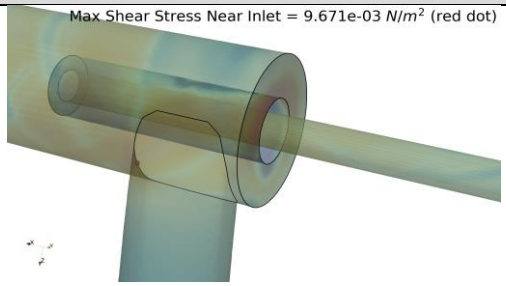
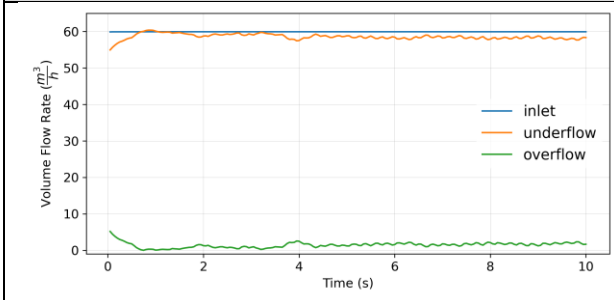


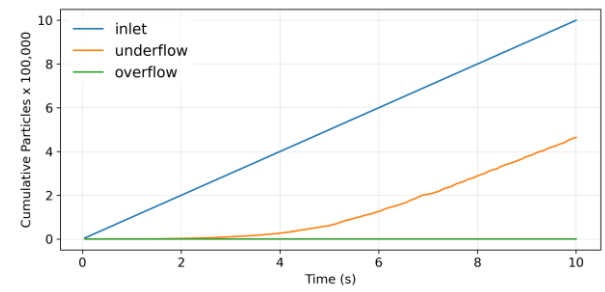
Figure B4: Volumetric flow, density and shear stress outputs of Run 6 in the DoE

Run 7: vortex finder diameter of 30 mm and feed SG of 3.6 t/m³

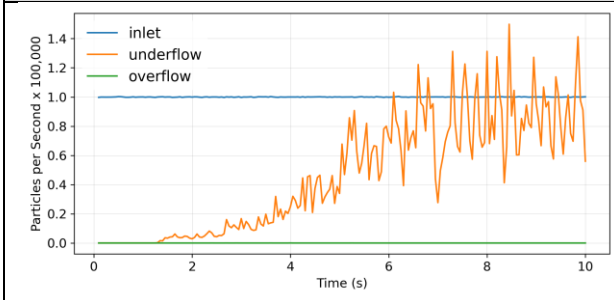
(A) Run 7: Volume Water Flow Rate



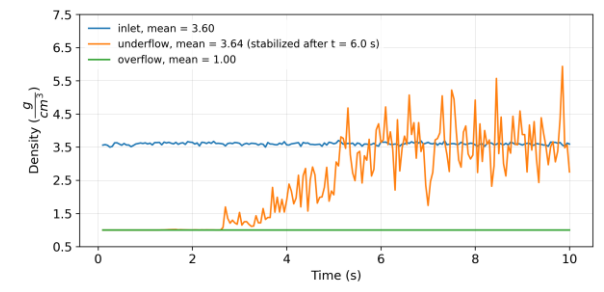
(B) Run 7: Cumulative Particle Flow



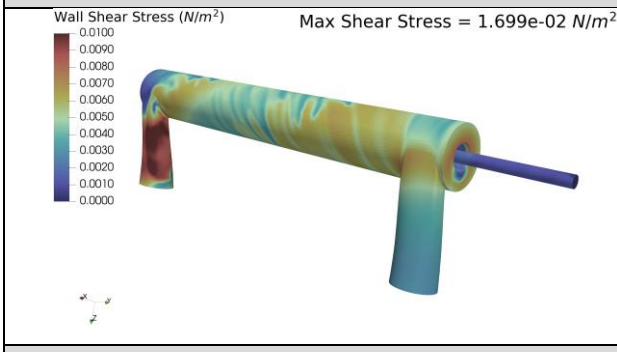
(C) Run 7: Particle Flow Rate



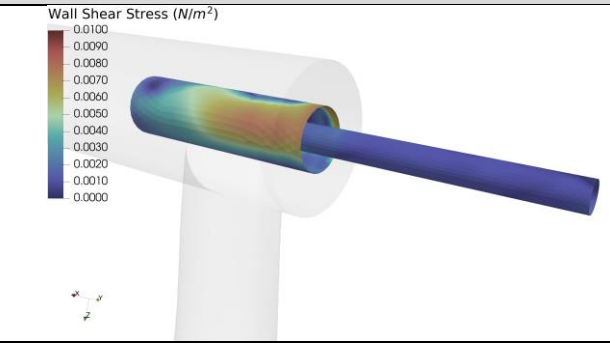
(D) Run 7: Effective Density



(E) Run 7: Shear Stress Full Domain



(F) Run 7: Shear Stress, Inside Geometry



(G) Run 7: Shear Stress Near Inlet

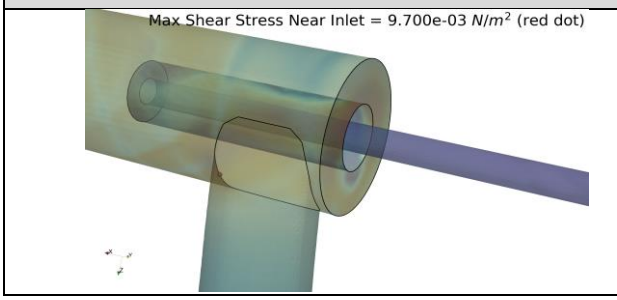
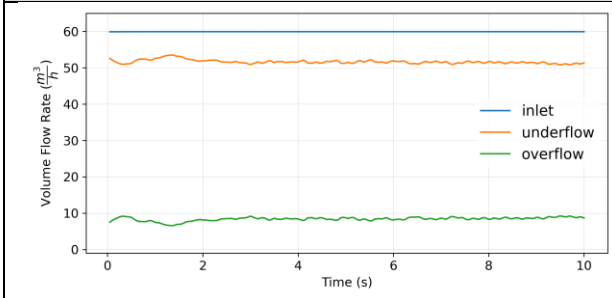


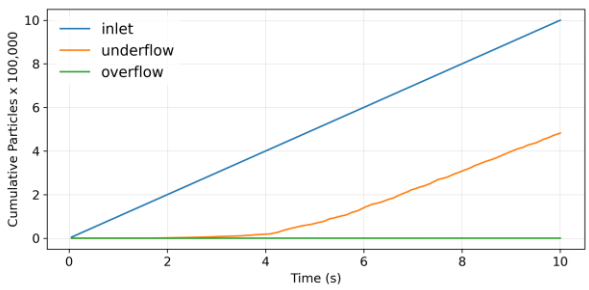
Figure B5: Volumetric flow, density and shear stress outputs of Run 7 in the DoE

Run 8: vortex finder diameter of 35 mm and feed SG of 3.6 t/m³

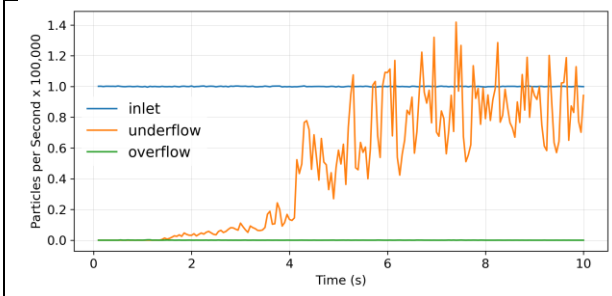
(A) Run 8: Volume Water Flow Rate



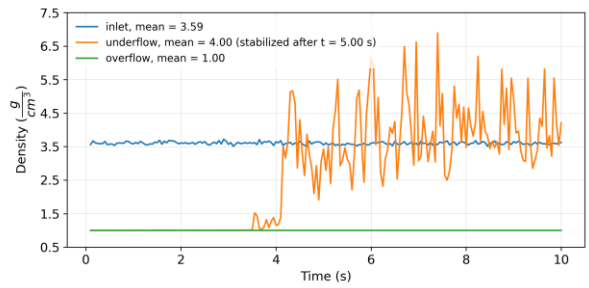
(B) Run 8: Cumulative Particle Flow



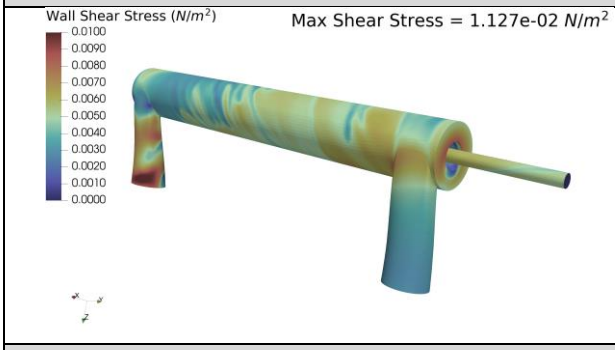
(C) Run 8: Particle Flow Rate



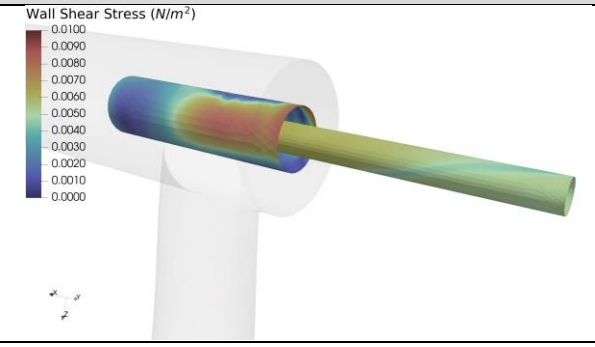
(D) Run 8: Effective Density



(E) Run 8: Shear Stress Full Domain



(F) Run 8: Shear Stress, Inside Geometry



(G) Run 8: Shear Stress Near Inlet

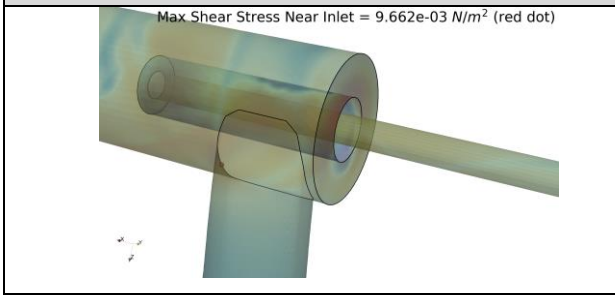


Figure B6: Volumetric flow, density and shear stress outputs of Run 8 in the DoE

APPENDIX C: SAFETY CONSIDERATIONS

Safety is a priority at Sishen mine. Therefore, a safety comparison and risk assessment procedure was evaluated for the two densifier types.

The Multotec PC200 densifier type is a safer option than the HMA 200NB since the parts are bolted together and are not clamped. Clamps often lose their tightness and shoot off under high-pressure conditions, as mentioned in the Problem Statement of this study. The Multotec PC200 also has weep holes to identify early part failures, which the HMA densifier unit does not have. Overall, no densifier inlet failures were recorded over a period of four years since installation of the Multotec PC200. This makes it a favourable option for Sishen mine.

It is important to keep in mind the risk assessments and standard operating procedure to be followed when inspecting and replacing densifier parts. The Job Risk Assessment (JRA) for inspection, replacing and unblocking of densifier parts was reviewed and updated to incorporate the Multotec PC200 unit and is found under SHEQ-SISHEN-FORM-213. Some of the top risks involved are:

- noise inducing hearing loss
- falling objects, debris and loads
- person falling from height
- slipping, tripping or falling down a staircase/ladder
- electrical shock
- failure of lifting equipment
- slipping, tripping or falling from a walkway
- being struck by fluid under pressure

It is important to note that both densifiers' upstream and downstream energy sources need be locked out for inspections and replacement of parts. Usually, a Level 1 isolation and lockout procedure will suffice for the inspection and replacement of parts. Level 1 isolation does not require an isolation permit; only a SLAM risk assessment.

The minimum requirements for Level 1 lockout and isolation are that the equipment should not involve more than three lock-out points and there should be fewer than eight people working on the inspection and replacement of densifier parts. All workers must ensure that their personal locks comply with the requirements of their personal locking devices. The workers must ensure that a lock-out box is available when required.

The procedure to be followed is outlined as follows:

i. Contact the control room (radio, telephone or visit) and request handover and stopping of equipment. Control room to note it on Level 1 isolations page.
ii. Isolate, lock-out and tag (electrical, pneumatic, hydraulic, mechanical, potential, or kinetic energy) as may be required and make safe. Ensure that the isolation mechanism is robust and in proper working order. The isolation officer must be authorized to lock out himself.
iii. Test for electrical isolation, e.g., voltage, pressure, elevated equipment, gasses, chemicals, temperature, tension, radiation and attempt to start from control room and local start. Mark test for dead confirmations off on the SLAM, the control room will also mark it on their Level 1 page. All the other teams should be cleared from the equipment before testing takes place. This is applicable where the test can result in a dangerous situation.

iv. Conduct a risk assessment of the work to be performed, ensure that all persons involved in the task have the correct PPE, ensure that the correct tools and equipment are available for the task, complete the risk assessment form (SLAM), make area safe by ensuring all deviations on the SLAM are addressed and work can continue safely.

v. Ensure that all personnel required to work sign the SLAM and start work.

vi. Start work to inspect and replace the densifier parts by removing the clamps or unbolting the unit.

vii. Level 1 isolation should not require handover; it must be completed by the team on shift. A permit needs to be completed if handover becomes necessary.

APPENDIX D: INDUSTRIAL CONSIDERATIONS

The comparison in terms of success factors for the two tested densifiers is summarized in Table 10.1. The success factor is commonly referred to at Sishen mine as a basic comparison between two applications to identify which would be more beneficial for the industry.

Table D1: Comparison between the two types of tested densifiers

Sishen success factor	HMA 200NB	Multotec PC200
Safety	Clamped design, unsafe	Bolted down, with weep holes
Wear rate	0.31 mm/day and MTTF for the inlet is 6–7 weeks at best.	0.04 mm/day and the inlet outlast the HMA densifier by 2.5 times.
Single stage efficiency	Allowably efficient but should be operated with the addition of control water to the dilute sump.	Allowably efficient but should be operated with the addition of control water to the dilute sump.
Ease of implementation	Unplanned total replacement time is 20 minutes to 1 hour but needs to be replaced frequently when it fails unexpectedly, which increases the D300 time.	Planned total replacement time 1 hour 30 minutes and can be done on planned maintenance. Operations need to have hand tool training and an impact tool to speed up the replacement.
Cost per unit	Unit price for parts is cheaper, but replacement occurs more frequently, making it the more expensive option.	It will be more cost effective in the long run. Break-even point calculated at seven months.

From these practical findings it can be concluded that:

1. **Safety:** The Multotec densifier is a safer design since it is a bolted down unit rather than a clamped unit, and it has weep holes that facilitate inspection of parts.
2. **Wear rate:** Mean-time-to-failure (MTTF) of the HMA densifier is four times greater than its current counterpart (Multotec) with a wear rate of 0.05 mm/day. It has lasted for a total of three months.
3. **Separation efficiency:** The Multotec densifier can provide a densifier overflow density of 1.6 g/cc with a 30 mm diameter vortex finder and a magnetic separator feed density of below 1.2 g/cc with the condition that the make-up water is open.
4. **Ease of implementation:** With the correct hand-tool training and appropriate impact tools, operators can replace the Multotec parts within an hour on planned maintenance. Also, mounting stand is proposed in the supporting documents that will satisfy and standardize the safety and process requirements.
5. **Cost-benefit:** FeSi consumption will also be positively impacted since FeSi will not be washed out to the dilute circuit or dropped to the floor. Weekly operational cost benefit outweighs the current HMA densifier unit by an average of R500/week.

It is recommended that the Multotec PC200 be used for densification at the Sishen drum plant under the following conditions:

- Make-up water feeding the dilute circuit should always be locked out, with the keys issued to each foreman and be kept safe in the key control box.

- Appropriate stand/mount to be manufactured for the unit to enable one standard for densification equipment in the drum plant.

- Operations receive hand-tool training and the appropriate impact tools to facilitate replacement when needed.

- Multotec should revise the overdesign on the unit to minimize the number of bolts on non-critical areas.

It is also recommended that test work and fine tuning be done to evaluate the effect of the inlet pressure on the Multotec densifier to optimize the separation efficiency of the unit.

APPENDIX E: INSPECTION AND MAINTENANCE SCHEDULE

Part of the condition monitoring for this test work was to install pressure gauges before the HMA 200NB and Multotec PC200 densifiers to inspect the correct operational pressures for the units on a 12-hourly basis. Consider the illustration below for clarification.

Pressure should remain constant between 430–500 kPa. The densifier sump overflows to the correct media sump, ensuring that the pressure to the densifier unit remains constant. This will be achieved if the media in the system is sufficient to maintain overflow conditions at the densifier feed sump. If the pressure falls out of operating limits, an investigation of the densifier parts should be triggered. The Table E1 below indicates the minimum, maximum lifetime and MTTF of each part.

Table E1: Densifier part lifetime and replacement schedule

Densifier part	**Lifetime of part (weeks)**		**Replacement schedule MTTF (weeks)**
	Min	Max	
Multotec inlet head liner	16	22	19
Multotec main body liner	52	52	52
Multotec discharge liner	52	52	52
Multotec 30 mm vortex finder	12	18	15
HMA inlet	4	7	5
HMA outlet	16	20	18
HMA 32 mm vortex finder	3	7	5
HMA main body	16	20	18

This strategy needs to specify how frequently parts need to be replaced and it needs to be incorporated into the maintenance planning schedule. The strategy should be to open and inspect the parts according to their minimum lifetime and replace if necessary and to schedule a replacement on the MTTF.